University of Alberta

Wireless Implantable Load Monitoring System for Scoliosis Surgery

by

Daniel Zbinden

A thesis submitted to the Faculty of Graduate Studies and Research
in partial fulfillment of the requirements for the degree of

Master of Science
in
Biomedical Engineering

Department of Electrical and Computer Engineering

©Daniel Zbinden
Spring 2011
Edmonton, Alberta

Examining Committee

Dr. Nelson Durdle, Electrical and Computer Engineering

Dr. Edmond Lou, Electrical and Computer Engineering

Dr. Vicky Zhao, Electrical and Computer Engineering

Dr. Kajsa Duke, Mechanical Engineering

Abstract

Surgical correction of scoliosis is a complicated mechanical process. Understanding the loads applied to the spine and providing immediate feedback to surgeons during scoliosis surgery will prevent overloading, improve surgical outcome and patient safety. Long-term development of residual forces in the spinal instrument after surgery with the continual curvature changes over time has been unknown. The goal of this research work was to develop a wireless implantable sensor platform to investigate the loads during and after surgery. This thesis describes research leading to the design of a sensor platform that uses both 403 MHz and 2.45 GHz for wireless communication, and reports the resolution and accuracy of the built-in temperature sensor, the A/D accuracy of the sensing platform, the power consumption at different operation modes, the range of the wireless communication and the discharge characteristics of a potential capacitive power module.

Acknowledgement

Table of Contents

List of Tables

List of Figures

List of Abbreviations

ADC	Analog to Digital Converter
AIS	Adolescent Idiopathic Scoliosis
AM	Amplitude Modulation
AP	Anteroposterior (front to back)
API	Application Programming Interface
ASIC	Application Specific Integrated Circuit
ASK	Amplitude Shift Keying
CD	Cotrel-Dubousset
CMOS	Complementary Metal Oxide Semiconductor
DAC	Digital to Analog Converter
DCLK	Digital Clock
DIO	Digital Input and Output
DLL	Dynamic-Link Library
DMA	Direct Memory Access
ECG	Electrocardiogram
EDLC	Electric Double Layer Capacitor (Supercapacitor, Ultracapacitor)
EEPROM	Electrically Erasable Programmable Read-Only Memory
EM	Electromagnetic
EMI	Electromagnetic Interference
EMR	Electromagnetic Radiation
EPR	Equivalent Parallel Resistance
ESR	Equivalent/Effective Series Resistance
ETSI	European Telecommunications Standards Institute
FCC	Federal Communications Commission
FM	Frequency Modulation
FPGA	Field-Programmable Gate Array
FSK	Frequency Shift Keying
GPIO	General Purpose Input and Output

IC	Integrated Circuit
I2C	Inter-Integrated Circuit
IDE	Integrated Development Environment
ISM	Industrial Scientific and Medical
ISP	Implantable Sensor Platform
LF	Low Frequency
MedIC	Medical Implant Controller (Windows software)
MEMS	Micro-Electro-Mechanical System
MICS	Medical Implant Communication Service
MOSFET	Metal Oxide Semiconductor Field Effect Transistor
OOK	On-Off Keying (modulation)
OpAmp	Operational Amplifier
PA	Posteroanterior (back to front)
PC	Personal Computer
PCB	Printed Circuit Board
RAM	Random Access Memory
RF	Radio Frequency
RFID	Radio-Frequency Identification
RX	Receive
SMA	SubMiniature version A
SPI	Serial Peripheral Interface
TET	Transcutaneous Energy Transfer/Transformer
TX	Transmit
USB	Universal Serial Bus
VAD	Ventricular Assist Device
WISP	Wireless Implantable Sensor Platform
WLAN	Wireless Local Area Network

Chapter 1

Introduction

Adolescent Idiopathic Scoliosis (AIS) is a three dimensional deformity of the spine affecting approximately 2% to 2.5% of the adolescent population [1]. Despite many years of research effort, its cause is still unknown. Figure 1-1 shows the back of a scoliosis patient. The physiological deformities associated with AIS can cause psychological discomfort in patients. Symptoms that commonly occur in association with scoliosis include pain and psychological stress. If AIS is left untreated and a large curve develops, it can injure both the lungs and heart causing significant health problems [2].
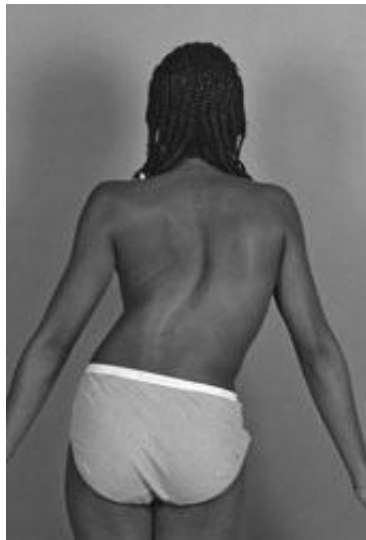
Figure 1-1: Scoliosis patient [3]

About 10% of AIS patients or 0.23% of the general adolescent population require treatment [1, 4]. Progression of scoliosis severity is difficult to predict, so treatment is usually based on serial observations and on an individual basis. Among those who require treatment, approximately 1% eventually require surgical intervention [1].

The goal of the surgery is to correct the curvature or at least to prevent it from progressing any further. This is usually done by fusing several vertebrae together. Harrington [5] developed the first widely used internal spinal instrumentation for the treatment of scoliosis. It consisted of a distraction rod and hooks that were used to stretch the lateral curve. Cotrel and Dubousset (CD) [6] improved upon this design by taking the three-dimensional nature of the deformity into account. The CD spinal instrumentation consists of pedicle hooks and screws which are placed at multiple levels along the spine. A pre-bent rod in the shape of the corrected spine is then loosely attached to the hooks and screws and turned to forcibly correct the lateral curve. This is called the derotation maneuver. Finally, the rod is locked in place and the vertebrae within the curve are fused together with bone graft in order to preserve the desired shape. Figure 1-2 shows pre- and post-surgical radiographs of a scoliotic spine.
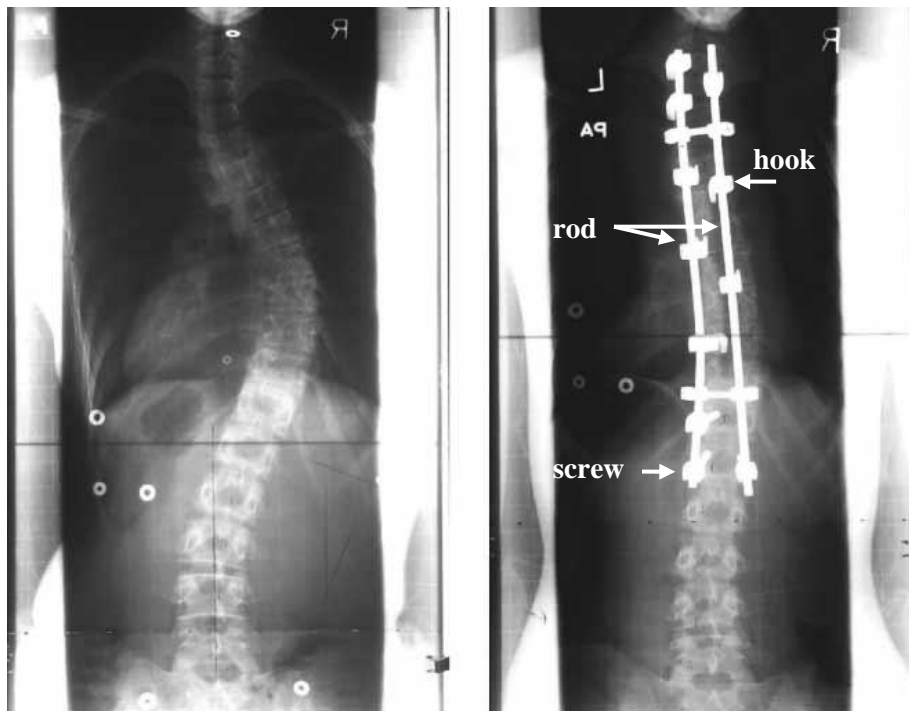
Figure 1-2: Radiographs of scoliotic spine before (left) and after surgery (right)

The success and outcomes of surgery depend heavily on the skill and experience of the surgeon. The amount of force applied is critical, since too much force can result in screws being pulled out of vertebrae or bone failing at the hook site, while too little force may result in sub-optimal correction [7, 8].

A good understanding of biomechanics during surgical correction of scoliosis is essential for optimizing procedure safety and outcome. Monitoring the load distribution after surgery allows detection of instrumentation failure such as screws being pulled out of the vertebra. Computer models are being developed to simulate forces during surgery and predict surgical outcomes [9-12]. To develop and verify these models, real surgical data gathered with telemetry systems are required. Loads have been measured on Harrington instrumentations [5, 13-16] and other spinal fixation devices [17-19].

More recently, telemetry systems for use during CD surgeries have been developed. Intraoperative optoelectronic analysis was employed to track three dimensional vertebral displacement after CD rod rotation [20]. Loads applied by the surgeon and distributed to the spine through the instrumentation were monitored using an instrumented rod rotator [21] and wireless telemetry attached to instrumented hooks and screws [22, 23], respectively. These designs were limited to use during the surgery and were sometimes obstructive to the surgeon due to size or cable connections. Furthermore, using the systems sometimes required additional work from the surgeon as he had to replace the instrumented hooks and screws with standard versions at the end of the surgery.

There is a need for a small, unobtrusive telemetry system that can monitor loads during surgery and can be left inside the body to continue operation after surgery and report residual forces. The system should work independently and transmit data wirelessly in order to avoid the inherent infection risk of wires penetrating the skin. Such a system would aid in better understanding the biomechanics during and after scoliosis surgery. This better understanding can then be used to optimize the procedure and make it safer by providing real-time feedback to the surgeon during surgery. Reporting the residual forces after surgery can provide information about the healing process and detect instrumentation problems.

1.1 Objectives

The objective of this research is to develop an implantable low-power load monitoring system to be used during and after scoliosis surgery. The ultimate goal of the developed system is to aid in the understanding of spine biomechanics and help improve efficacy and safety of surgical procedures.

1.2 Thesis Organization

This thesis consists of six chapters. It starts with an introduction to the work and the motivation behind it in Chapter 1. This includes information about scoliosis and treatment with a focus on surgery. The objectives are listed and the scope of this work is defined.

Chapter 2 provides anatomical background and a literature review about scoliosis, scoliosis surgery, surgical complications, mechanical forces during surgery and technical solutions for data transfer and power supply.

Chapter 3 describes the system requirements and design challenges. The approaches used to solve these challenges and test the results are described.

Chapter 4 describes the system design. First the rationale behind design choices and technical background grouped by individual design challenges is described. Then the technical specifications of the hardware built are listed.

Chapter 5 describes verification and testing of the designed system. Testing procedures are described and resulting data given. Test results are discussed and compared to the system requirements.

Chapter 6 summarizes the results of this thesis and concludes this research work.

Chapter 2

Background

This chapter provides background information by reviewing the literature. It begins with the definition of medical terms and a review of the spine and vertebra anatomy. Adolescent idiopathic scoliosis (AIS) and its treatment alternatives are then described. Surgical treatment and complications of scoliosis are discussed. Force measurement methods and experiments that have been conducted to find maximal acceptable forces at the implant-bone interface are reviewed. Research into the modeling of spine instrumentation biomechanics and surgical outcome prediction is described. An overview of techniques used to exchange data and power between implanted devices and an external system is given. Finally, internal energy generation and storage techniques are compared.

2.1 Anatomy

The following paragraphs provide a brief introduction to medical terms and describe the basic anatomy of the vertebral column and a typical vertebra.

2.1.1 Body Planes and Orientation

A specialized terminology is used in the literature and this thesis when discussing the spatial orientation of the spine and the mechanics of scoliosis treatment. Figure 2-1 illustrates anatomical planes and orientations.
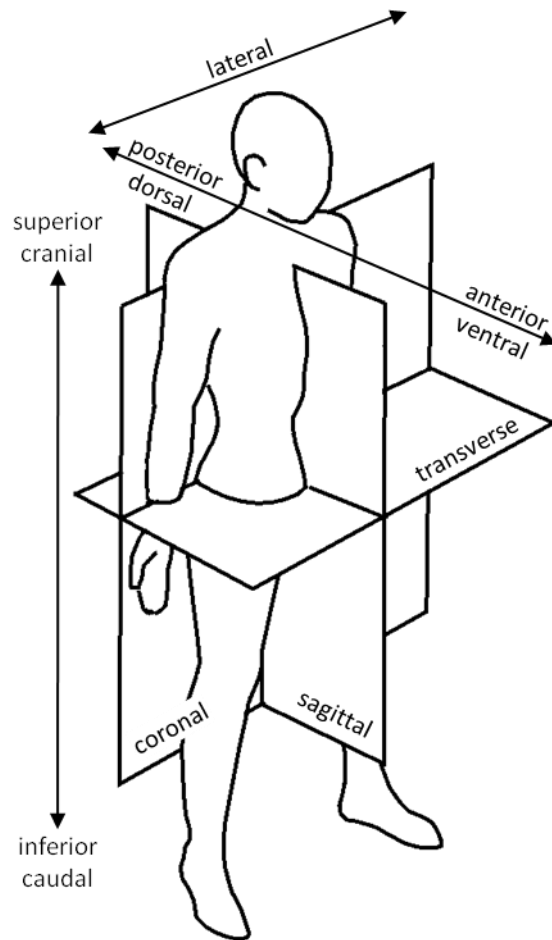
Figure 2-1: Body planes and orientation

The coronal plane divides the standing human body vertically into front (anterior, ventral) and back (posterior, dorsal). The sagittal plane divides the body vertically into left and right. A view of the body in the sagittal plane is called side view or lateral view. The transverse plane is known as an axial plane or cross-section and divides the body horizontally into top (superior, cranial) and bottom (inferior, caudal) portions.

2.1.2 Vertebral Column

The human spine consists of 33 bone segments called vertebra that are stacked on top of each other and separated by intervertebral discs. The vertebral column is divided into the four groups: cervical, thoracic, lumbar and pelvic as illustrated in Figure 2-2.
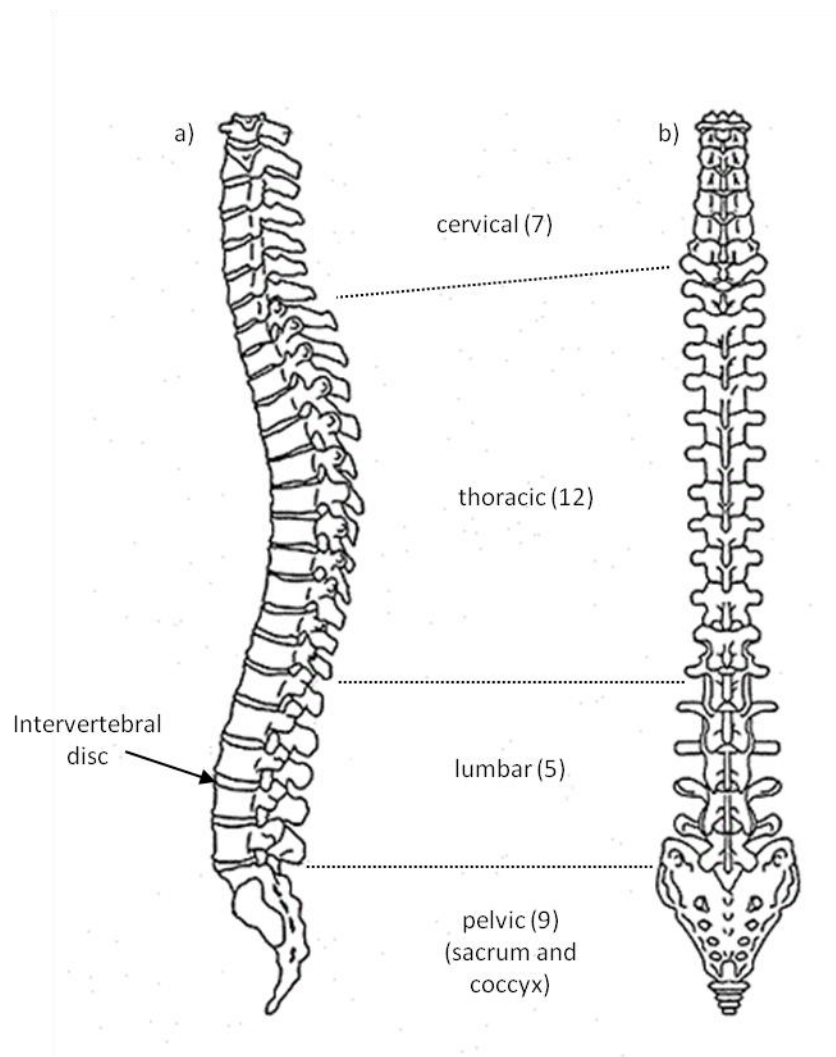
Figure 2-2: Vertebral column a) lateral view and b) posterior view

The individual vertebra are named and numbered from superior to inferior according to the region they are located in. Seven cervical vertebrae C1-C7 comprise the neck region with C1 also known as "atlas" supporting the head. The ribs attach to twelve thoracic vertebrae T1-T12. The largest five vertebrae L1-L5 are located in the lower back lumbar region. The five fused sacral vertebrae S1-S5 and the three to four fused coccygeal (tailbone) vertebrae connect to the pelvis.

A normal erect spine has multiple natural curvatures in the sagittal plane while keeping the head level and centered above the sacrum. The two most prominent curvatures bend dorsal in the thoracic region (kyphosis) and ventral in the lumbar region (lordosis).

When viewed on a posteroanterior (PA) radiograph, the vertebrae of a normal erect spine line up on a straight line, with no lateral curvature in the coronal plane.

2.1.3 Vertebra

Even though all vertebrae have a similar basic structure, their shape and size varies depending on their location on the spine. A lumbar vertebra is used here as an example since it is a good representation for the thoracic and lumbar vertebrae involved in scoliosis as described later. Figure 2-3 shows the individual features of a lumbar vertebra.
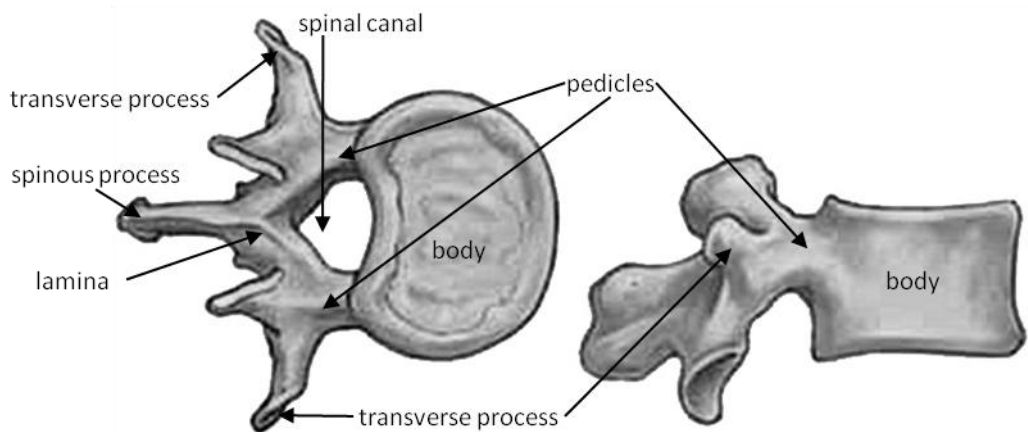
Figure 2-3: Lumbar vertebra superior view a) and lateral view b)

The vertebral bodies separated by intervertebral disks support most of the body weight. Two vertebrae with a disc between make up a motion segment. The transverse processes form muscle and ligament attachment sites and are connected to the vertebral body by the pedicles. The spinous process also forms muscle and ligament attachment sites and is connected to the pedicles through the lamina. The spinal cord is dorsally nested against the vertebral body and surrounded by the pedicles and lamina.

2.2 Adolescent Idiopathic Scoliosis

2.2.1 Definition and Natural History

Scoliosis is a three-dimensional deformity of the spine characterized by an abnormal lateral curvature and an axial rotation of the vertebrae. Figure 2-4 shows posterior views of a scoliotic spine and a normal spine. Structural deformities cause one or more abnormal primary curvatures which are compensated by functional curves in order to restore balance and center the head above the sacrum [24].

8
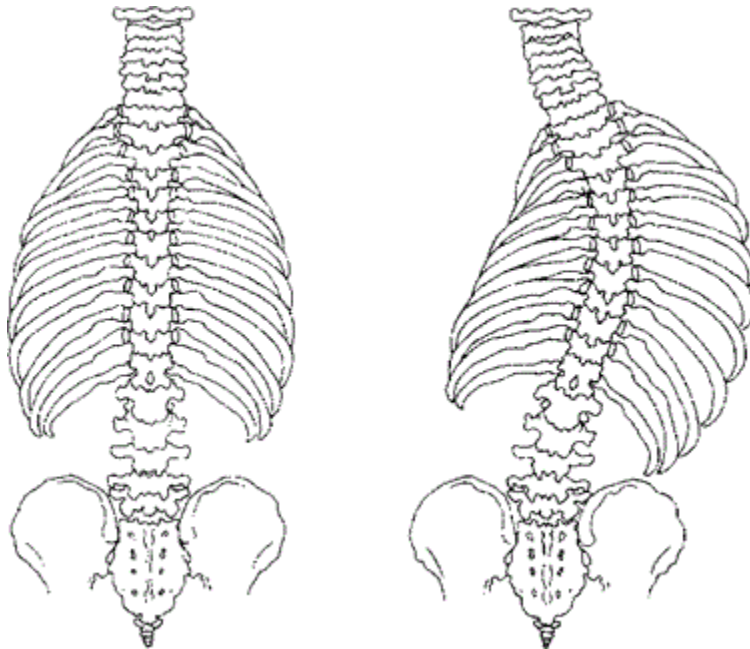
Figure 2-4: Posterior view of normal spine (right) and scoliotic spine (left)
[www.uihealthcare.com]

Scoliosis can have several causes, including congenital, neuromuscular [25] and genetic. In about 80% of the cases, however, no cause can be determined and such cases are termed idiopathic [3]. This type of scoliosis affects 2-3% of adolescent populations [1]. Scoliosis can be classified by age of onset as infantile (birth to age 3), juvenile (age 4 to 10) and adolescent (11 to maturity) [3]. The work described in this thesis focuses on adolescent idiopathic scoliosis (AIS).

Although it is a three dimensional deformity, scoliosis is clinically defined as a Cobb angle greater than 10º. The Cobb angle is measured on a posteroanterior (PA) radiograph by first drawing lines parallel to the endplates of the most tilted superior and inferior vertebra. The angle between two lines that are perpendicular to those parallel lines is the Cobb angle (Figure 2-5).
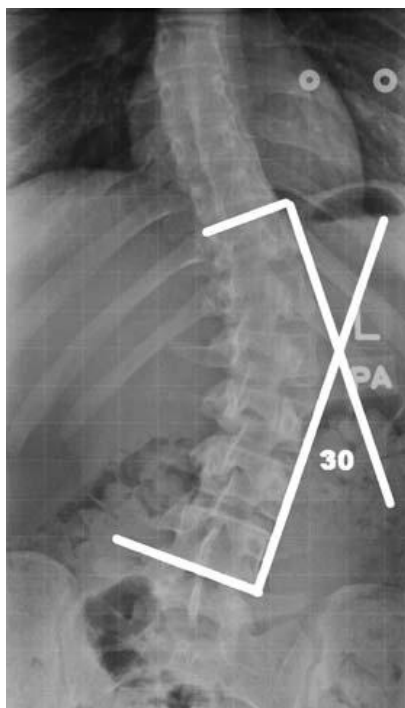
Figure 2-5: Cobb angle measurement on PA radiograph [26]

Curves of 50° at maturity or 80° during adulthood can increase risk of shortness of breath and curves of more than 100° can cause premature death although mortality rate is not significantly increased [1].

2.2.2 Treatment

About 10% of adolescent idiopathic scoliosis (AIS) patients require treatment [1, 27]. Despite many years of research, the progression of AIS cannot be predicted reliably [28]. The decision on treatment options take skeletal maturity and curve severity into consideration and also depend on the surgeon's preference. Patients with curves less than 25° are usually monitored regularly, curves between 25° and 40° are treated with bracing and more severe cases are corrected by surgery. Other methods that are sometimes used but have not yet been proven effective include exercise, biofeedback and electrical stimulation. The work described in this thesis focuses on surgical treatment which will be described in the following section 2.3.

2.3 Surgical Instrumentation and Procedure

The first widely used spinal instrumentation system was described by Harrington in 1962 [5]. The design had been developed over the previous years based on a device that was

first used in 1949. At that time, scoliosis was still considered a two dimensional lateral curvature. Therefore, the Harrington system only acted in the coronal plane, using a distraction rod on the concave side and a compression rod on the convex side of the curve. These rods stabilized the spine until fusion occurred.

Since then, various systems based on hocks, screws, wires and rods have emerged [29-34]. One widely used example of a posterior approach is the spinal instrumentation system developed by Cotrel and Dubousset (CD) [6] based on an understanding of scoliosis as a three-dimensional deformity. Key elements of the CD method are described in more detail in the following paragraphs.

2.3.1 Cotrel-Dubousset Surgical Instrumentation

CD instrumentation allows for three dimensional corrections of spinal deformities and is based on rods, hooks, screws and devices for transverse traction (Figure 2-6). The rods are made out of stainless steel or titanium and are pre-bent to a predetermined end curve. Hooks and screws have different sizes, depending on where on the spine they are used.
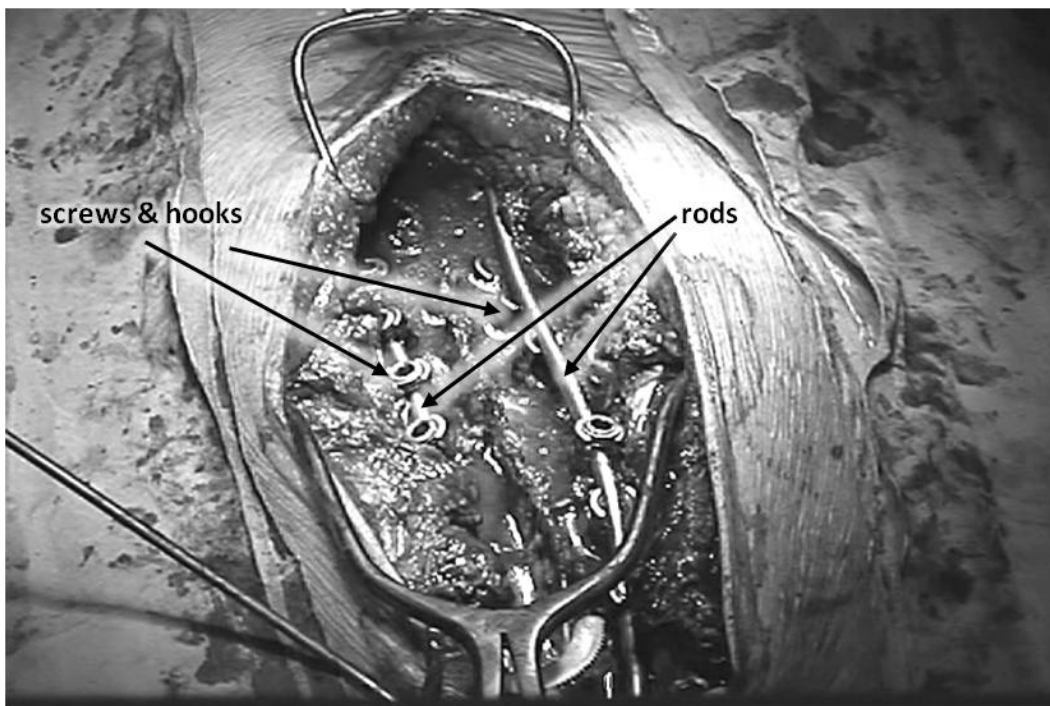
Figure 2-6: Cotrel-Dubousset instrumentation

2.3.2 Pre-op Planning

When planning the surgical correction of scoliosis, several factors such as patient size, weight and age, spine elasticity and bone quality need to be taken into account. These will have an influence on the number of attachment sites needed and the amount of correction that is achieved.

Traditionally, the hook and screw placement sites were selected and laid out on preoperative radiographs of the spine. However, the final correction has been difficult to predict and the best instrumentation configuration has remained controversial [35]. More recently, computer software has been developed to aid in surgical planning and predict the correction bases on patient characteristics and instrumentation variables [36]. Such software was also used to optimize instrumentation strategies by comparing the simulated outcome of several hundred strategies [12].

Once the surgeon has determined the strategy to use, the patient is placed on the table face down in prone position. An incision is made down the center of the back, spanning the length of the planned instrumentation.

2.3.3 Hook and Screw Placement

The location of screws and hooks are chosen so that they distribute corrective force over several vertebrae in order not to exceed maximum forces at any one location. A claw construct may be used at both ends (cranial and caudal) of the instrumentation since forces tend to be highest there [36]. The claw construct consists of two opposing hooks around one or sometimes two vertebrae. Laminar hooks are inserted into the spinal canal either on the superior edge of the lamina or below the inferior edge of the lamina. Pedicle hooks have a notched blade to hold the pedicle. A right-angled notch needs to be cut from the inferior facet of the cephalad vertebra in order to place pedicle hooks. Transverse hooks can be placed above or below a transverse process. They should, however, never be used alone but always in combination with a pedicular hook since the transverse process is a weak point. Pedicle screws are inserted into the vertebral body posteriorly through the pedicles.

2.3.4 Rod Insertion and Translation Maneuver

Before the rod is secured to the hook and screw heads, it is shaped to approximate the desired sagittal contour after correction. It is first inserted on the concave spine at either

end of the instrumentation and then progressively inserted into the remaining hooks and screws with the help of a translator-introducer device and loosely secured inside the screw and hook heads by set screws. This is the first part of the correction, since the spine is forced to adapt to the rod shape. The second rod is inserted on the convex side after the derotation maneuver in order to improve the derotation result.

2.3.5 Derotation Maneuver

Once the rod is loosely attached to all hooks and screws, it is rotated using rod rotators. In this maneuver, the lateral curvature is rotated towards the concave side of the curve into the sagittal plane. It is critical not to exceed maximum forces as this would result in bone failure and require a replacement of the hook or screw [7]. The instrumentation is fixed in this position by tightening the set screws.

2.3.6 Fusion

Bone graft is used to fuse the curve. This is to provide a more stable correction and relieve some of the pressure from the instrumentation. It takes about 6 weeks for the fusion to take effect during which time the patient should avoid strenuous activities.

2.4 Surgical Complications

Surgical complications related to the instrumentation occur in about 0.64% of AIS surgeries [37]. Intraoperative pedicle fractures were observed with an incidence of 0.50% per screw inserted [7]. Loosening of the pedicle screws was observed in 0.54% and pullout in up to 0.67% per screw inserted. Most of the pedicle screw pullout occurred at the apex of the curve during the correction maneuver [7]. It is, therefore, important to monitor the forces applied during surgery. Scoliosis surgery also carries the risks of a major surgery: 6% to 29% chance of requiring re-operation and a remote possibility of developing a pain management problem [1].

2.5 Mechanical Forces

Improving instrumentation safety by investigating its mechanics is not a novel idea. Biomechanical tests have been done to find maximum allowable forces at the bone-screw and bone-hook interface. In vivo force measurement systems and biomechanical models have been developed in order to get a better understanding of the quantitative forces and optimize surgical procedures.

2.5.1 Biomechanical Tests

The pullout strength and traction resistance of screws and hooks have been investigated in several studies [38-47]. The results of these studies were used to plan surgical procedures so that they would not exceed these maximum forces. Seller et al. found that pullout resistances varied with bone mineral density, screw type and screw length in cadaveric experiments. Pullout forces between 1863 N and 3159 N were observed [41].

2.5.2 In vivo Force Measurement

Several studies were dedicated to measuring loads for Harrington instrumentation [13-16] and other spinal instrumentation [48, 49]. Cotrel-Dubousset (CD) instrumentation, however, differs significantly from the Harrington instrumentation and existing results can thus not be easily adopted. The CD instrumentation applies major three-dimensional forces during the derotation maneuver while the Harrington instrumentation exercises mainly two-dimensional axial distraction and compression forces [5].

Lou et al. [22] used instrumented hooks and screws (Figure 2-7) to measure loads and moments on the CD instrument during surgery. The transducers were sensitive to push-in, pull-out and rotation about the rod axis, measuring a maximum force of 120 N and a maximum moment of 3.1 Nm during one surgery. Distraction forces acting along the rod axis and moments perpendicular to the rod axis could not be measured due to sensor design limitations. The instrumented hooks and screws were replaced by standard versions after the surgery was complete and before the wound was closed.
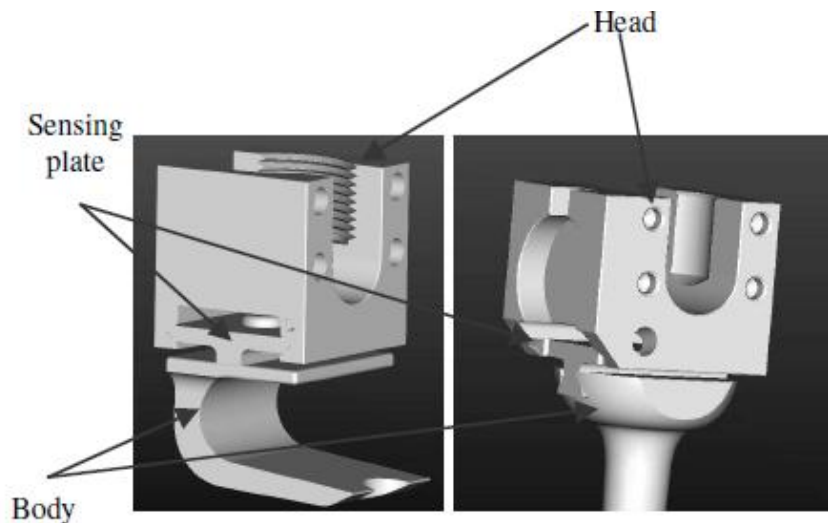
Figure 2-7: Instrumented hook and screw [23]

14

Lou et al. [21] employed an instrumented rod rotator (Figure 2-8) to measure loads and angular displacement applied by the surgeon during the CD derotation maneuver. Strain gauges in a half-bridge configuration were located inside a 'Gripper' box which was attached to a rod rotator. An inclinometer measured the orientation in the rod rotator plane. Measurements in seven patients showed maximum forces from 20-60 N with a torque of 4-12 Nm.
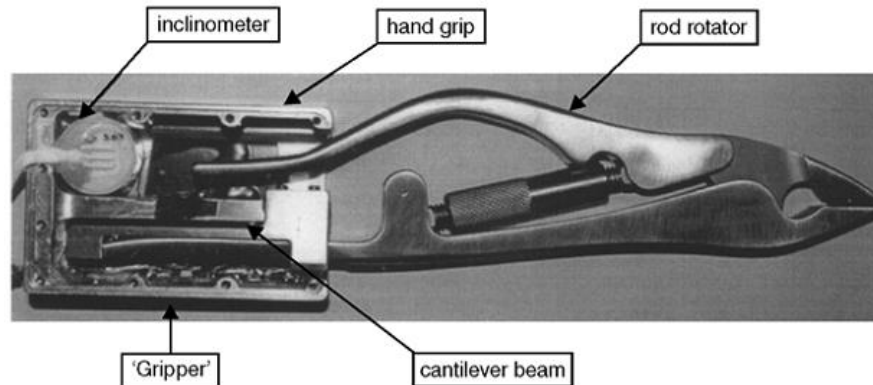
Figure 2-8: Instrumented rod rotator [21]

2.5.3 Biomechanical Models

Computer models to simulate scoliosis surgery have been developed with the goal of optimizing the procedure and make it safer [9, 10, 12, 35, 50-55]. A preoperative planning simulator [36] can be used to simulate hundreds of different configurations [12] to find the optimal procedure based on patient specific parameters. These models were developed with only pre- and postsurgical data available. Some of them predict intraoperative forces, but so far these have not been verified by measurements. Having real surgical intra-operative force values may improve the accuracy of these computer models.

2.5.4 Force Sensors

Benfield et al. [56] designed a piezoresistive micro-mechanical system (MEMS)-based sensor array to characterize in situ loads during scoliosis correction surgery. Piezoresistive sensors produced linear outputs and allowed for sensitivity adjustment. The sensor array was designed to fit into a standard hook or screw head which eliminated the need to redesign the entire hook/screw set (Figure 2-9). It was designed to measure three-dimensional forces of up to 1000 N and moments of up to 4000 N mm at each hook or screw.
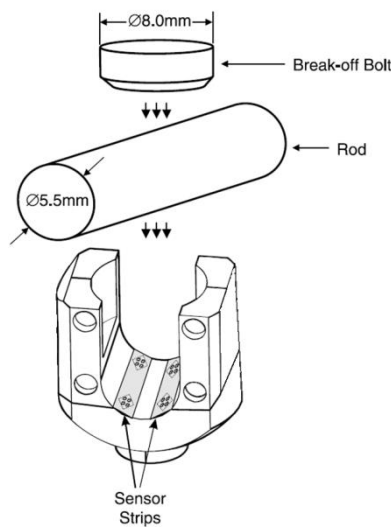
Figure 2-9: Instrumented hook or screw head [56]

The sensor array was based on a silicon diaphragm design and consisted of a total of 16 sensors on two strips per hook or screw head. Each of the sensors was connected to a supply voltage and delivered an output voltage proportional to the load applied. The direction and magnitude of the loads were determined by combining the output voltages of four sensors in a group. This means that a total of 16 differential voltages had to be measured for each hook or screw head.

2.6   Data Transfer and Power Supply

Two main challenges when designing an implantable telemetry system are the communication between the implanted and external systems, and the power supply of the implanted device. Setup commands need to be transmitted from an external controller to the implant and measured data needs to be transmitted from the implant to an external monitoring station. Power may be transmitted to the implant from an external source, generated from the body environment at the implant, or stored inside the implant at the time of implantation. The remainder of this chapter reviews techniques that have been used for *transcutaneous data and energy transfer* as well as *internal energy generation and storage*.

2.6.1   Transcutaneous Data and Energy Transfer

Providing external power to an implant via Transcutaneous Energy Transfer (TET) allows for a virtually unlimited operating time and relatively high power consumption when compared to internally powered devices. This comes at the cost of limited

mobility, since the external supply circuit needs to be in close proximity to the implanted device due to the limited range of most transmission methods.

Data transmission can be viewed as a form of energy exchange for the purpose of conveying information. Therefore, similar design principles apply to both, the data and energy link. Some methods described below allow for high data rates while others are better suited for high power transfer, and sometimes the same transmission method is used for both purposes at the same time.

A very simple and efficient method for a transcutaneous link is to run *wires* through the skin. This method, however, bears an inherent infection risk and should thus be avoided for long term use [57].

Omitting the wires and using the body fluids to conduct a current instead has also been investigated. This method called *galvanic coupling* allows transmission of data at a rate of several kilo bits per second (kbps) up to a range of several centimeters [58] via electrodes either implanted or attached to the skin. Transmission power needs to be limited and the transmission frequency needs to be carefully selected in order to avoid tissue damage, pain, muscle stimulation, electrode dissolution and development of potentially harmful gasses [59].

Another approach to transmitting energy to an implanted device is using *ultrasonic* pressure waves. This method is immune to electromagnetic interference, but direct skin contact is required and transmission power has to be limited below 100 mW in order to avoid tissue damage [60].

Optical data and power links consisting of a light source and a photovoltaic converter transmit power in the milliwatt range [61] and are immune to electromagnetic interference. They require an optical path and are thus limited to a range of a few millimeters when transmitting through the skin [61, 62].

The most common TET method used is based on electromagnetic (EM) fields. A transmitter coil or antenna generates EM fields which are received by a receiving coil or antenna either via *inductive coupling* or *radio frequency transmission*. Inductive coupling receivers tap into the energy stored in the magnetic near field of the transmitter at distances typically smaller than one wavelength. Radio frequency (RF) receivers

capture the electric field radiated by the transmitter over distances typically larger than two wavelengths. Both principles are described in more detail in the following paragraphs.

Inductive Coupling

Transcutaneous energy transfer via inductive coupling can be viewed as an electrical transformer with an external primary coil and an internal secondary coil (Figure 2-10). It is based on Faraday's law of induction which states that the induced electromotive force in any closed circuit is equal to the time rate of change of the magnetic flux through the circuit. Efficient energy transfer depends on high mutual induction between the two coils which requires good alignment and close proximity. Primary and secondary circuits are tuned to the same resonant frequency for maximum efficiency [63].
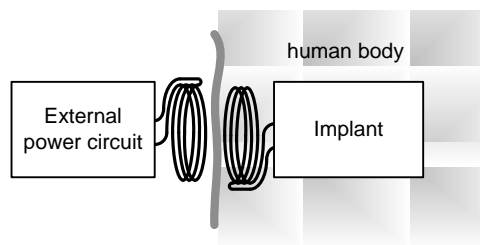
Figure 2-10: Inductive coupling

Mutual induction can be increased by using *ferrite cores*. Ferrite cores may reduce the interference on the implant circuitry by channeling the magnetic field [64]. The downside of this channeling effect is increased tissue heating due to the high magnetic field density between the cores. Self heating of the cores due to internal magnetic losses may further aggravate this problem. Furthermore, ferrite cores add weight to the implant and take up valuable space.

Other parameters that influence the system performance are the *operating frequency* and the physical dimensions of the coils. These two are directly related to each other, as a higher operating frequency allows for smaller coil dimensions. As the frequency increases, however, heating of the tissue becomes a problem. Therefore, the carrier frequencies for inductive energy transfer systems usually are below 10 MHz [64] and should not be higher than about 50 MHz [65].

One challenge when designing an inductive coupling system is to maintain a stable *output voltage*. Changes in coil separation and misalignment as well as load resistance

18

variations affect the output voltage. The load resistance increases when the implanted circuit switches to a low power mode. While a voltage regulator in the implant [66] can reduce some of the variations, some sort of frequency tuning of the circuit is usually employed as well.

The primary circuit can be detuned by deliberately *shifting the operating frequency* away from the resonant frequency of the coil [67], thereby reducing the amount of power transferred. The operating frequency can also be shifted to match the resonance frequency of the secondary coil [68] in order to increase the transferred power. The *resonant frequency of the primary coil* can be tuned by a switched variable capacitance [69] or a current-controlled variable inductance called transductor [66]. The *amplitude* of the power signal may be adjusted by pulse-skipping or varying the duty cycle of the inverter [62]. Data is either modulated on top of the energy link or via dedicated inductive link. Using the same coils for both energy and data transfer reduces the overall size but may reduce energy transfer efficiency.

Theogarajan [70] used separate concentric coils for data and energy transfer. Digital data was transmitted as a *pulse-width modulated* (PWM) signal with a carrier frequency of 13.56 MHz. This high frequency allowed for a data rate of up to 714 bps and provided good separation from the 125 kHz power signal.

Tang et al. [71] transmitted data to the implant by modulating two frequencies on top of the power signal. *Amplitude modulation* (AM) was chosen to keep the receiver inside the implant simple.

Djemouai and Sawan [63] used *amplitude shift keying* (ASK) of the power signal to transmit data to the implant.

Riistama et al. [72] used *load modulation* to transfer data from the implant to the external device. Off the shelve radio frequency identification (RFID) base station and RFID transponder IC's provided a data rate of up to 10 kbaud.

Sodagar et al. [64] transmitted data at 2 Mbps by *switching the frequency* (FSK) of the power signal between 4 and 8 MHz.

Inductive coupling has been widely used to provide energy to medical implanted devices. The basic principles and safety risks are well understood. Therefore, inductive coupling

19

is most suitable for transcutaneous power transmission. The limited transmission range of this method made rechargeable energy in the implantable device storage necessary.

Radio frequency transmission

Radio frequency (RF) receivers differ from inductive coupling in that they tap into the radiated electromagnetic energy rather than the local magnetic field. A radio link is mainly used for data transmission over distances greater than one wavelength. Even though several different wireless transmission principles exist as previously described (optical, ultrasonic, galvanic), the term "*wireless transmission*" is commonly used when referring to *RF transmission* and, therefore, these two terms will be used in this thesis interchangeably.

With the advances in low power wireless technology, new standards are emerging and small transceivers become commercially available. In 1999 the Federal Communications Commission (FCC) established the license free Medical Implant Communication Service (MICS) for communications over a distance of up to two meters. This new standard operates at a lower frequency than other common standards such as Zigbee, Bluetooth or WLAN, and thus offers better transmission in a body environment. In addition, the MICS band is reserved to be operated by medical personnel, which reduces the risk of interference.

The main challenge in designing an implantable radio system is the antenna. Implantable antennas need to be small enough to fit inside the body while maintaining reasonable radiation efficiency. In order for the radiation efficiency to remain constant, the size of an antenna has to grow with decreasing frequency. Commercially available antennas are usually optimized for operation in air. Since the electrical characteristics of a human body differ significantly from those of air, implantable antennas have to be specifically designed for this environment.

Karacolak et al. [73] developed a printed circuit board (PCB) dual-band antenna for use with a radio integrated circuit from Zarlink Inc. Finite-element boundary integral electromagnetic simulation code and a particle swarm optimization algorithm were used to optimize the antenna for the 402-405MHz MICS band and the 2.45GHz ISM band. The dimensions were 22.5x22.5x2.5mm^3. Houzen et al. [74] developed a planar inverted-F antenna optimized for the 402-405MHz MICS band and measuring

40x30x3.2mm^3. Sodagar et al. [64] used a LC tank with an optional loop antenna to transmit on-off-keyed (OOK) data at 70-200 MHz.

The design processes of these antennae involved the optimization of an original design. Finding a good original design required experience and the design process involved specialized software and test equipment. Finally, the antenna needed to be manufactured using specialized materials and techniques. Commercially available antennae may be a good alternative to a custom design, saving development time. Therefore, available antennae were evaluated.

Data Link Frequency Considerations

The optimal operating frequency of a wireless communication link depends on the desired *range*, the transmission *medium* and *interference* from other sources.

The wavelength is sometimes used instead of the frequency to characterize a sinusoidal waveform. The wavelength λ of an electromagnetic wave traveling through air is given by

(2-1) $$\lambda = \frac{c}{f}$$

where c is the speed of light and f is the frequency.

The *range* depends on the path loss which includes several factors. Among these factors, the frequency dependant path loss L is given by Friis transmission equation [75]

(2-2) $$L = \left(\frac{4\pi \cdot d}{\lambda}\right)^2$$

where d is the transmission distance and λ is the wavelength. This means that the transmission range with a given amount of power increases with increasing wavelength since the path loss decreases with the square of the wavelength.

The transmission *medium* for this system was air and body tissue. While transmission losses in air are minimal, the human body absorbs a significant amount of the radio signal. These losses are frequency dependant and tend to increase with increasing frequency due to the dielectric properties of the tissue [76]. This effect not only hinders wireless transmission but also has possible adverse effects on the body due to tissue heating.

Other wireless devices *interfere* with the radio link if they operate in the same frequency range. Institutions such as the Federal Communications Commission (FCC) or European Telecommunications Standards Institute (ETSI) regulate the frequencies used by wireless applications. Several frequency bands are available for Industrial, Scientific and Medical (ISM) use. These ISM bands have been defined for a while and are used by many applications. More recently, the Medical Implant Communication Service band (MICS) at frequencies of 402-405 MHz has been reserved for medical applications.

2.6.2 Internal Energy Generation and Storage

Several technologies have been developed to harvest electrical power from renewable body environment energy. Glucose fuel cells [77] generate power from the electrochemical reaction of oxygen and glucose that are present in body fluids. Human motion [78] or muscle movement [79] is converted into electrical energy by piezoelectric materials. While these technologies have the potential to allow life-time independent operation of low powered implants, their power production currently in the microwatt (µW) range is not enough for a radio-enabled real-time data acquisition system.

A more common alternative to a transcutaneous energy link is the use of implanted energy storage. Sometimes a rechargeable storage, periodically recharged via a transcutaneous link, allows for limited independent operation [61]. Energy can be stored in different forms and converted into electrical energy when needed. A rather unusual approach was investigated by Norman et al. A completely implantable system consisted of a nuclear fuel capsule that served as a heat source for a steam engine which in turn powered an artificial heart [80].

More common is the use of electrochemical batteries, either non-rechargeable primary cells or rechargeable secondary cells [81-83]. These range in capacity from several micro-ampere-hours (µAh) for specially designed microbatteries [82, 83] up to several milli-ampere-hours (mAh) for commercially available coin-cells.

Electric Double-Layer Capacitors (EDLC), also known as supercapacitors or ultracapacitors have a capacitance that is typically on the order of a thousand times greater than electrolytic capacitors. Small coin-size cells can have a capacitance of several hundreds of millifarads. Compared to rechargeable batteries, EDLCs have lower energy density, higher self-discharge rate and less stable output voltage. However, they

22

show little degradation even after thousands of charging cycles, have high cycle efficiency and low self-heating due to their low equivalent series resistance (ESR). The biggest advantage of EDLCs is their high charge- and discharge rates which makes EDLCs suitable for pulsed operation and easy to charge.

Therefore, EDLCs have significant potential as medium term power storage for either periodically (via transcutaneous energy link) or continuously (via energy harvesting) charged devices.

2.6.3 EDLC capacity considerations

The total amount of energy stored by electric double-layer capacitors depend on their characteristics like the capacitance in Farad and the voltage rating. However, in a scenario where an EDLC is powering a load (Figure 2-11), the amount of energy that can be utilized by the load depends on the minimum operating voltage of the load.
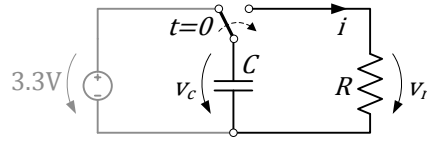
Figure 2-11: Capacitor discharging over load resistance

In general, when a capacitor is discharged over a load resistance R as shown in Figure 2-11, its output voltage $v_c(t)$ follows approximately the curve given as

(2-3)
$$v_C(t) = V_0 \cdot e^{-t/R \cdot C}$$

where V_0 is the initial voltage across the capacitor and C [F] is the capacitance. The power $p_r(t)$ dissipated by the load can be calculated by equ.(2-4) and is shown in Figure 2-12.

(2-4)
$$p_r(t) = \frac{v_c(t)^2}{R}$$

23
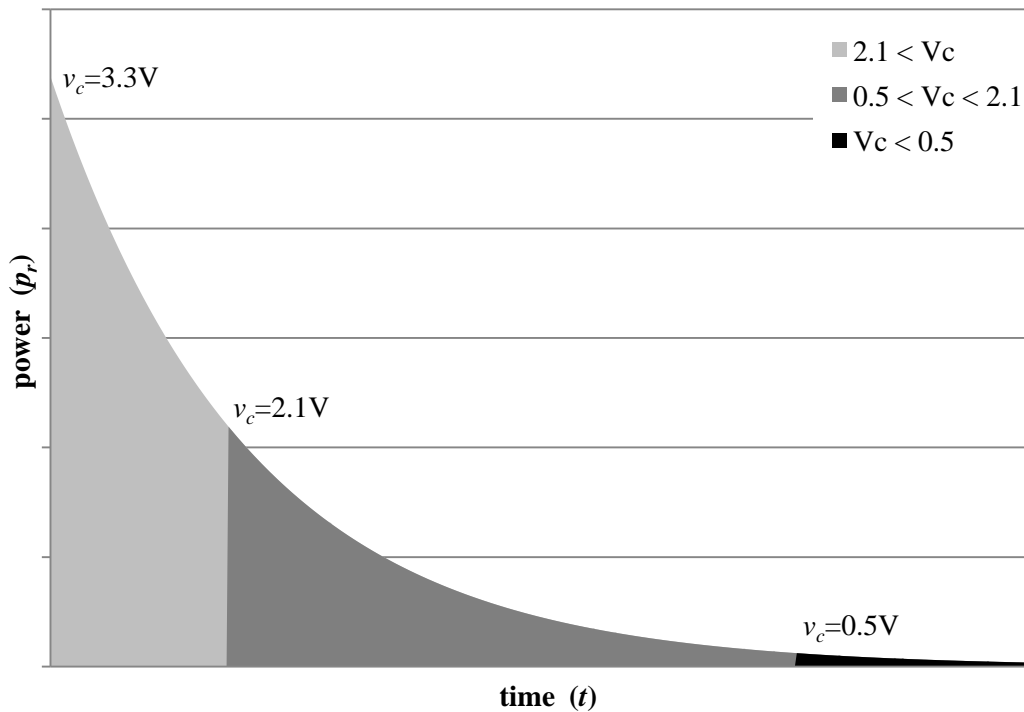
Figure 2-12: Capacitor discharge curve; power dissipation

The total energy J [Ws] stored in the capacitor when it is charged to $V_0 = 3.3$ V is represented by the entire area under the curve as given by

(2-5) $$J = \int_{t=0}^{\infty} p_r(t)dt$$

The light grey area in Figure 2-12 represents the energy that can be used with v_c above 2.1 V while the dark grey area represents the energy dissipated when v_c is between 0.5 V and 2.1 V. It can easily be seen from Figure 2-12 that the amount of usable energy stored in the capacitor can be significantly increased if the load can function with a lower supply voltage or the capacitor voltage can be boosted to provide a higher supply voltage.

Another way of computing the usable energy of a capacitor is based on equation (2-6) which gives the energy J [Ws] stored in a capacitor with capacitance C [F] as a function of the voltage v_c.

(2-6) $$J = \frac{1}{2}Cv_c^2$$

The difference between the energy J_1 stored when the capacitor is fully charged at its maximum rated voltage $v_c = V_1$ and the energy J_2 stored at the minimum operating voltage $v_c = V_2$ determines the usable energy ΔJ.

(2-7)
$$\Delta J = J_1 - J_2 = \frac{1}{2}C(V_1{}^2 - V_2{}^2)$$

Both, capacitance C and rated voltage defined by physical characteristics and cannot be changed for a given capacitor. This leaves minimizing V_2 to maximize the usable energy ΔJ. Therefore, the usability of a power module using a step-up converter to boost the EDLC voltage was investigated in this thesis.

Chapter 3

Methodology

This chapter reports the methodology required to develop an implantable system for force measurements during and after scoliosis surgery. The system consists of two main components, the implantable sensor platform (ISP) and the base station. This chapter identifies different environments in which the system is operated and elaborates on system requirements and on the procedures required to satisfy these requirements. The design challenges are addressed individually and methods to validate the system are described.

3.1 Operating Environments

The system will operate in two different environments (Figure 3-1). Forces and moments need to be measured and displayed in real-time *during surgery*. *After surgery*, the patient will return to the clinic periodically. During these clinic sessions, the therapist will ask the patient to perform several bending exercises. The forces and moments again need to be measured in real-time while these exercises are performed. In between these real time sessions the ISP will be inactive. The specific requirements for the two operating environments *surgery* and *therapy* are described in the following paragraphs.
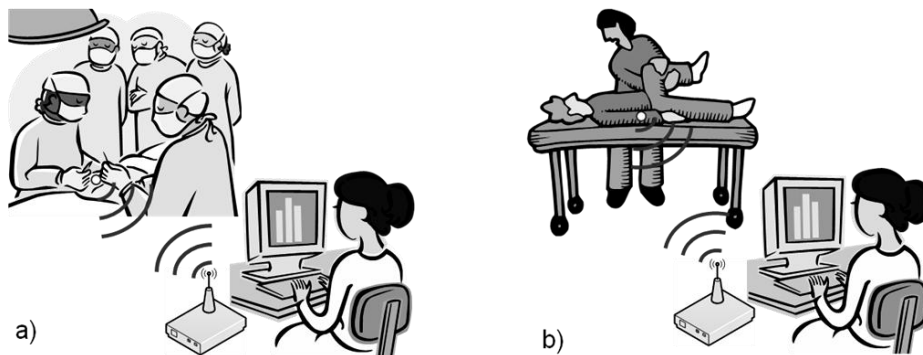
Figure 3-1: Operating environments a) surgery and b) therapy

3.1.1 Surgery

There is a sterile area which measures about 2 m x 2 m from the center of the patient during surgery. Non-sterilized equipment is kept away from this area. In this situation, data needs to be transmitted from the implanted part of the system to a base station outside the sterile area (Figure 3-2). Using wires to transmit data should be avoided since they would interfere with the surgeon. A wireless transmission path in this situation leads through air, but the line of sight will likely be blocked by tissue immediately around the implant and surgical staff around the patient.

Part of the total surgery time is spent on preparing the patient for insertion of the spinal instrumentation which is not very interesting from a biomechanical point of view. The surgeon can then turn on the system before he spends approximately 30 minutes correcting the curvature and adjusting the instrumentation. During that time, the implanted system needs to be able to operate independently without recharging. The implanted system is then still accessible for possible battery replacement or other modifications before the surgical incision is closed.

Figure 3-2: Operating room overview with 1) position of patient 2) position of base station

3.1.2 Therapy

After the scoliosis surgery, the implantable system is embedded inside the body approximately 20-35 mm below the skin surface. This is the minimum range required of wireless data and power links.

In order to avoid having to attach a bulky external supply circuit over the implant providing continuous power during therapy, implanted system should be recharged before each therapy session.

Data may be transmitted to a battery powered relay station strapped to the body or directly to a base station near the patient. Having a relay station close to the body eases the demands to on the wireless data link. The data can either be stored in the relay station and downloaded later or directly forwarded to the base station via a secondary wireless link.

3.2 Requirements of the Implantable System

The system must capture loads on the points where the instrumentation attaches to the spine (Figure 3-3a). The number of these locations varies with the number and size of curves to be corrected. The highest forces are expected at the extremities of the instrumented segment [36]. This means that at least 4 locations need to be monitored for two rods on a single curve. Installing wired connections between these locations would interfere with the surgical procedure and increase the risk of medical complications and technical failures. Therefore, separate implanted sensor platforms (ISP) will be used for each individual location and the communication between all ISP's and the external base station must be wireless.
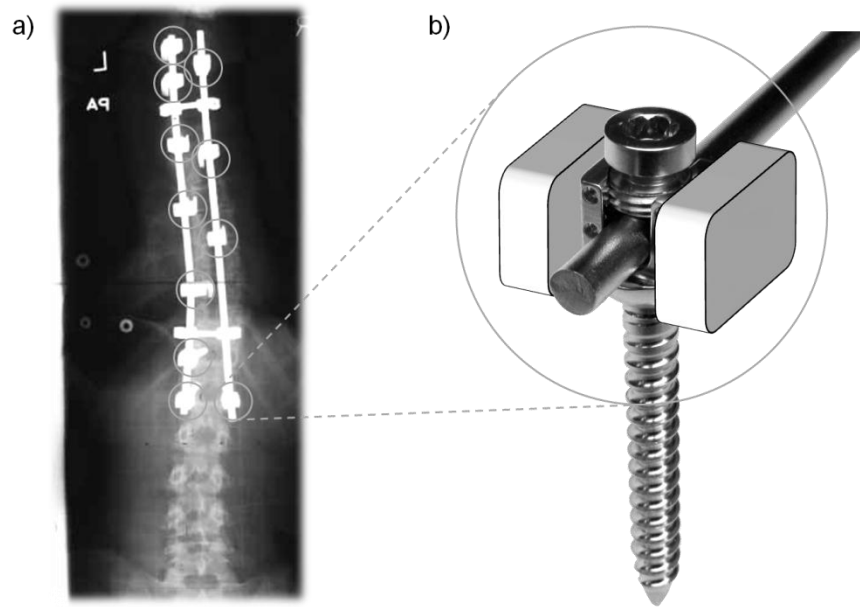
Figure 3-3: ISP locations: a) instrumentation spine attachment sites on AP radiograph, b) ISP location on screw head

The wireless protocol needs must handle communication between at least 4 ISP's and a base station. The minimum range is 2 m in free air during surgery and 20 mm through the skin during therapy sessions.

The majority of scoliosis patients are adolescent females. To embed the ISP's inside the body, they need to be small enough to fit near the spine without bulging the skin which would cause pressure points. Removing the spinous processes as a standard part of the surgical procedure will provide extra room, but the available space is still very limited. Figure 3-3b shows the arrangement of an ISP around an instrumented screw head.

MEMS-type transducers will be used to convert mechanical forces and moments into electric signals [56]. The ISP's must provide power to the transducers and measure the output voltages. 16 differential voltage signals per screw or hook head are required in order to capture three-dimensional forces and moments.

The power supply must last for at least 30 min without recharging to allow for independent operation during surgery.

3.3 Design Procedures

Operating the system after the surgery means that data has to be transmitted from inside the body to a computer. Since wires piercing the skin bear an infection risk, some sort of wireless data and power transfer is required. This thesis mainly focuses on the four design blocks: *transducer*, *wireless link*, *processing* and *power management* as shown in Figure 3-4. The body side refers to the implantable part of the system located near the spine inside the patient's body. The base station side contains the external part of the system including any wireless circuitry, power charging circuitry and a computer.

The transducer design was outside the scope of this thesis. A micro-electro-mechanical system (MEMS) type force transducer will be used to measure forces and moments [56, 84]. The wireless link was required to transmit commands between the base station and up to 4 implanted sensor platforms located on the body side. The processing block was needed to transport analog transducer signals to the computer and visualize them on the computer screen. The power management was required to store electrical energy in the sensor platforms and manage transcutaneous energy transfer (TET) from the base station to the sensor platform.
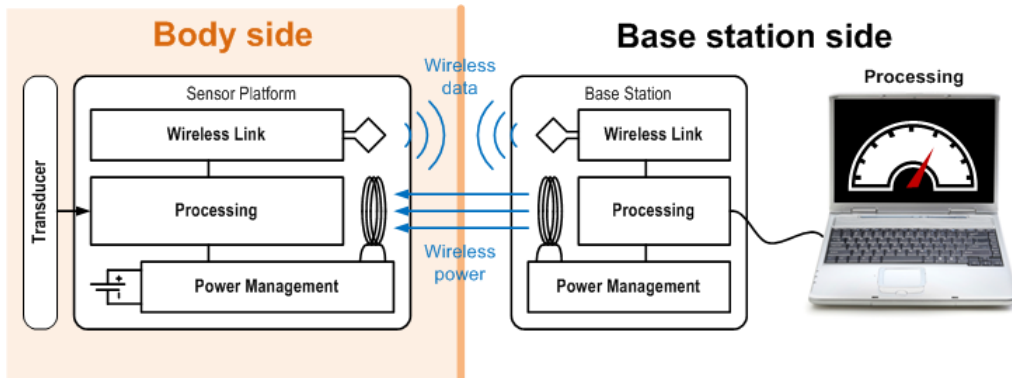
Figure 3-4: Design Blocks

For each individual design block, available technologies were investigated and the most suitable solution for this application was chosen. Five hardware modules were then built in order to verify the technology. Figure 3-5 shows the individual hardware modules *sensor platform*, *base station*, *power storage*, *energy transmitter* and *energy receiver* highlighted in grey. These hardware modules are described in the next chapter.
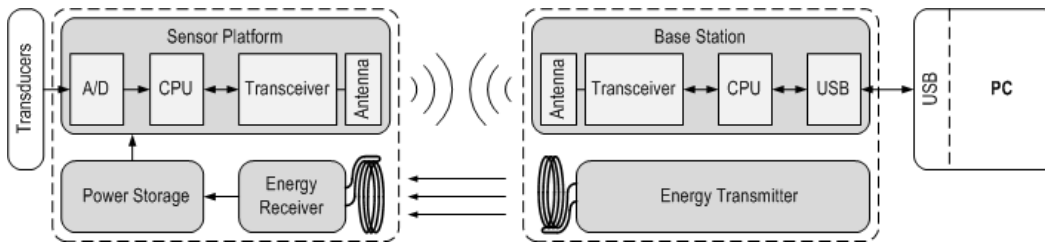
Figure 3-5: Hardware modules

3.4 Validation

Reliability of the system was verified by testing individual hardware modules or a combination of hardware modules. Table 3-1 gives an overview of the parameters tested and the hardware modules involved in testing a specific parameter.

The wireless communication is an important feature of the system. Both operating environments described in 3.1 create different demands on the wireless data link because of the different transmission paths. Both environments were thus simulated and tested individually. The wireless data link must have sufficient range to allow communication between the ISP's and the base station. In a packet based link, the packet loss rate is a measure of reliability. The wireless communication must be able to handle interference from other devices.

This system was designed to interface with MEMS typed transducers [56]. These transducers produce an output voltage that is proportional to the applied forces and influenced by the environment temperature [85]. The accuracy of a temperature sensor for temperature compensation of the measurements was determined. The accuracy and linearity of the analog to digital converter (ADC) used to digitize the transducer output voltages was tested and the correct transmission of the signal from the ADC to the PC user interface was verified.

The power storage must have a capacity high enough to provide power to the ISP's during the surgery. It must be rechargeable within minutes before each therapy session. The recharging time not only depends on the storage technology, but also on the amount of power the wireless power link can provide.

Individual tests are described in more detail in chapter 5.

Parameter Tested	Hardware Modules Involved
Wireless Data Link	
Range	Sensor Platform, Base Station
Reliability	Sensor Platform, Base Station
Interference	Sensor Platform, Base Station
Processing	
Temperature Sensor	Sensor Platform
Analog to digital converter	Sensor Platform
Signal transmission and visualization	Sensor Platform, Base Station, PC
Power Storage	
Capacity	Power Storage
Charging time	Power Storage

Table 3-1: Hardware testing

Chapter 4

System Design

This chapter describes the design of the wireless implantable sensor platform system. The block diagram in Figure 4-1 shows the main components of the system and gives an overview of how they interact. The system consists of one or several identical sensor platforms and a base station. Each sensor platform can connect up to 8 sensors without using multiplexing. Custom interface software written in Microsoft C# is used to manage the sensor network and visualize sensor values.
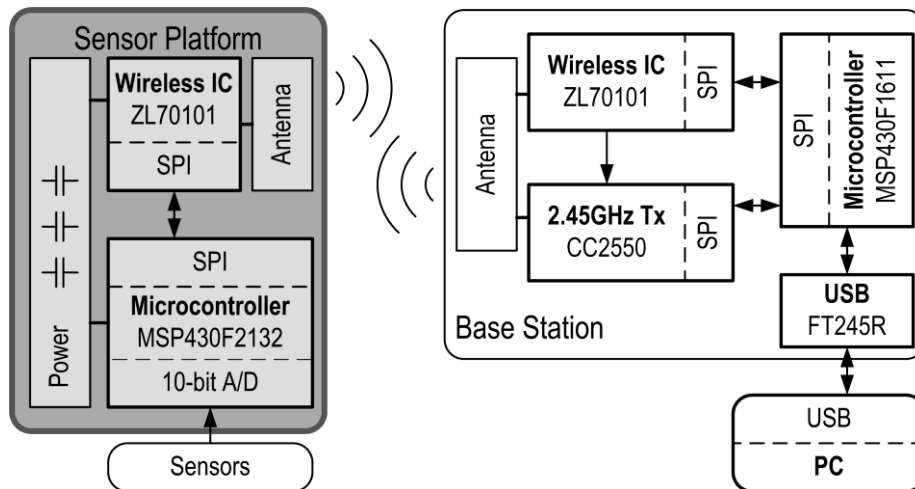
Figure 4-1: Block diagram of the wireless system

This chapter first describes the *wireless link* and then shows how the wireless transceivers were combined with other components to form the *sensor platforms* and *base station* modules. The design of a *capacitive power storage* module and a *transcutaneous energy transfer* link are described. Finally, the *software implementation* is described.

4.1 Wireless Link

A wireless link was used to transmit data between the base station and the implanted sensor platforms. This wireless link was an important part of the sensor platform and base station design because it would affect the power consumption and the selection of hardware components. Figure 4-2 shows the basic concept of a wireless link used to transmit a digital data stream through the transmission of electromagnetic energy. The following paragraphs describe the *transceiver selection* and *antenna design*.
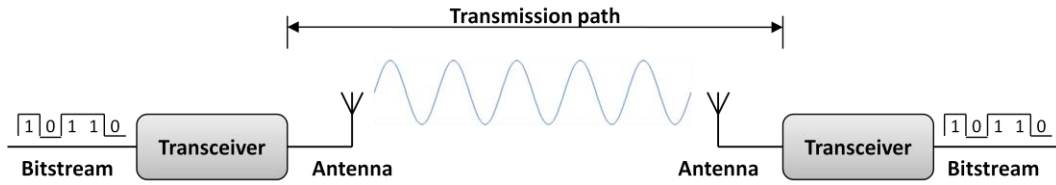
Figure 4-2: Wireless link diagram

4.1.1 Transceiver Selection

Commercially available wireless transceivers operating in the MICS band were evaluated based on parameters found in the manufacturers' data sheets (Table 4-1). The two most important criteria were the power consumption and the physical dimensions.

The ***power consumption*** not only depended on the supply voltage and current, but also on the data rate. A higher data rate requires less active time to transmit a certain number of bits. For example if the available data rate is twice what is required, the transceiver can be turned off half of the time. Data is stored locally while the transceiver is turned off and then transmitted in a burst at the full available data rate. This results in lower average power consumption.

Equation (4-1) gives the power consumption P [W] of a transceiver which is in transmit mode half of the time and in receive mode the other time.

$$(4\text{-}1) \qquad\qquad P = V_{sup} \cdot \frac{I_{Tx} + I_{Rx}}{2}$$

V_{sup} is the supply voltage and I_{Tx} and I_{Rx} are the supply currents in transmit and receive mode respectively. The energy J_b [Ws/bit] needed to transmit one bit is then given by

$$(4\text{-}2) \qquad\qquad J_b = \frac{P}{d_{raw}} = \frac{V_{sup} \cdot (I_{Tx} + I_{Rx})}{2 \cdot d_{raw}}$$

where d_{raw} [bit/s] is the raw data rate of the link. Note that J_b is an estimation which does not take into account any intermediate power modes and is based on theoretical data provided by the manufacturer. The *minimum supply voltage* was used as V_{sup} to compute J_b in Table 4-1.

The **total size** of the design was an estimation of the area required for the transceiver circuitry, including the package size and external components. The number of external components was counted on the manufacturer reference designs and included resistors, capacitors, inductors and switches, but not the antenna. For each external component an area of ($2x1mm = 2mm^2$) was added. An external microcontroller would be required to control the wireless transceiver if it did not have one built in. Therefore, an area of $25mm^2$ was added for transceivers without integrated microcontrollers. This is an estimation and does not take into account any oversized components nor room for trace routing.

Parameter / Product	Zarlink ZL70101	AMIS-52150	RFM TR3005	TI CC1010	TI CC1020	TI CC1100	TI CC1110
Frequency [MHz]	402-405 433-434 2450[1]	300-768	403.35-403.65	300-1000	402-470 804-940	300-348 400-464 800-928	300-348 391-464 782-928
Modulation	FSK	ASK OOK	ASK OOK	FSK OOK	FSK OOK	FSK OOK ASK	FSK OOK
Bit Rate [kbps]	800	16	115.2	76.8	153.6	500	500
Supply Voltage V_{SUP} [V]	2.1-3.5	2.3-3.6	2.2-3.7	2.7-3.6	2.3-3.6	1.8-3.6	2.0-3.6
Rx Current I_{RX} [mA]	5	7.5	3.8	9.1	19.9	15.2	18.1
Tx Current I_{TX} [mA] [2]	5	20[3]	7.5	10.4	16.2	15.5	20
J_b [µWs/bit] [4]	0.013	1.977	0.108	0.343	0.270	0.055	0.076
Interface	SPI	I2C + TxRx	Tx + Rx	register	SPI + DIO + DCLK	SPI	register
Package type	QFN-48	SSOP-20	SM-20H	TQFP-64	QFN-32	QLP-20	QLP-36
Package size [mm]	7x7	7x7.5	6.8x10	12x12	5x5	4x4	6x6
Ext. Components	6	20	14	10	18	15	15
Total size [mm^2]	85.4	115.5	119.6	163	84.2	69.5	64.5
Int. RF switch	✓	-	✓	✓	-	✓	✓
Int. Microcontroller	-	-	-	✓	-	-	✓

Table 4-1: Evaluation wireless transceiver

The ZL70101 from Zarlink is the most energy efficient transceiver, consuming about 13 nWs per bit. The smallest transceiver is the CC1110 from Texas Instruments, mainly because of its integrated microcontroller. Since the *ZL70101* is about six times more energy efficient than the CC1110, the Zarlink transceiver was chosen to build the system.

---

[1] Dedicated wakeup receiver
[2] Supply current when transmitting at 0 dBm (1 mW) output power
[3] Only maximum current consumption given (@ 12 dBm)
[4] See equation (4-2)

4.1.2 Antenna Design

One of the main challenges in designing an implantable wireless system is the antenna design. Antennae are interfaces between transceivers and the transfer medium. Different media require individually optimized antennae to achieve an efficient transmission. In other words, an antenna designed for use in air is less effective when it is embedded inside a body.

The dimensions of an antenna are related to the operating frequency. This means that antennae cannot be minimized arbitrarily and it is difficult to optimize them for several operating frequencies at the same time.

The Zarlink development kit included a helix antenna for the base station and a printed circuit loop antenna for the implant. Since the exact parameters for the helix antenna were not provided and the implant antenna dimensions (28 x 32 mm) were too large for this application, alternative solutions had to be investigated.

Commercially available antennae were used on both the base station and the sensor platform. A surface-mountable chip-antenna (ANT-403-SP, Antenna Factor) was used on the sensor platform. This antenna measured 30 x13.7x1.5 mm and had an impedance of 50 Ω at the center frequency of 403 MHz.

Experiments were performed to determine whether this antenna would be suited to receive the 2.45 GHz wakeup signal and how this antenna performs when implanted inside the body.

Antenna tuning and impedance transformation

Impedance matching is an important concept in high frequency design. It is based on the fact that the maximum amount of power is transferred from a source with impedance Z_S to a load with impedance Z_L if they are complex conjugates. In a wireless system, the source is either the transmitter or the antenna and the load is either the antenna or the receiver, depending on whether the device is in transmit or receive mode. Source and load impedance can be matched by means of an impedance transformation network (Figure 4-3).
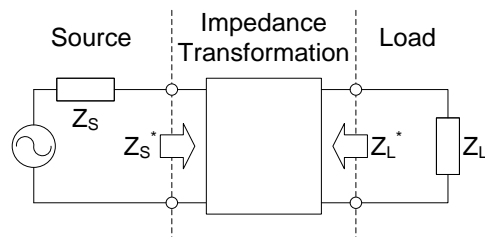
Figure 4-3: Impedance matching

The impedance transformation network presents a complex conjugate load Z_S^* to the source. Several methods can be used for impedance transformation, including transmission lines, discrete component networks or inductive transformers.

The Zarlink design manual[5] points out that the ZL70101 transceiver works best if the antenna is *not matched* to its internal impedance. The manual recommends the antenna impedance should be transformed to 500 Ω at the 400 MHz receiver input and transmitter output. In other words, when using this 400 MHz transceiver, the impedance of the antenna should be matched to 500 Ω. There is no information available about the impedance of the 2.45 GHz receiver inside the ZL70101.

4.2 Sensor Platform

The two main components of the sensor platform shown in Figure 4-4 were the wireless transceiver and the microcontroller. In this prototype, the antenna was connected through a coaxial SMA connector for better testability. The antenna can be stacked on top of the transceiver circuit in order reduce the overall size. Connection headers were provided to connect to external sensors. The following paragraphs discuss the microcontroller selection, describe the signal interface and list the sensor platform module specifications. Circuit schematics can be found in Appendix A-1.

---

[5] ZL70101 Design Manual rev.1.1, Dec. 2007, pp.57
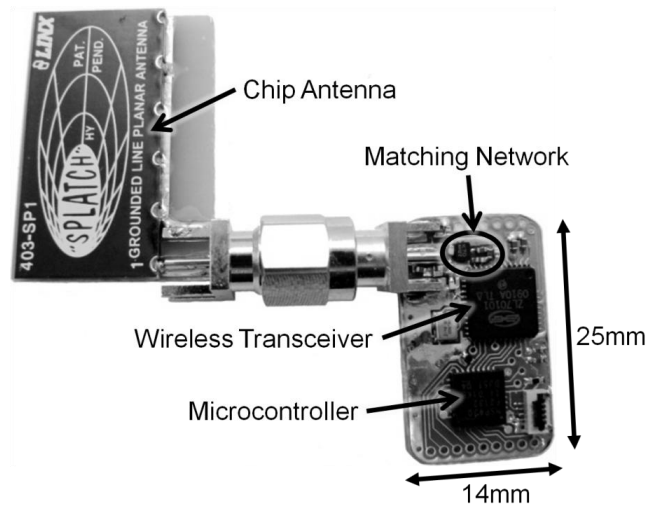
Figure 4-4: Sensor platform with antenna

4.2.1 Microcontroller Selection

The development kit for the Zarlink wireless transceiver included microcontrollers from Texas Instruments (MSP430F1611) on both, the implant and base station side. Using microcontrollers for the system rather than field programmable gate arrays (FPGA) allowed for reuse of source code and speed up the development. The purpose of the development kit was to demonstrate the capabilities of the ZL70101 transceiver but it was not designed to meet low power and small size requirements. Therefore, a different microcontroller had to be found for the implantable part of the system. This microcontroller had to have the following *characteristics*:

- Include Serial Peripheral Interface (SPI) for communication with the ZL70101 transceiver.

- Have 3 digital output pins to control the sensors (in addition to 8 ADC pins and 6 pins for the ZL70101 interface).

- Include 8 Analog to Digital Converters (ADC) with minimum 10 bit resolution to measure analog signals from the force sensors.

- Have a minimum of 8 kB of flash memory to store the embedded software[6].

---

[6] Link map generated by Code Composer Essentials v.3.1 showed 17.2 kB of flash memory and 300 Bytes of RAM used by Zarlink code. Removing trace library, error library and some other

39

- Have a minimum of 300 Bytes of RAM[6 above].

- Consume low power

- Be of small size

Table 4-2 lists the parameters of low power and small size microcontrollers from three of the most popular manufacturers. The suitability of these microcontrollers for use in the sensor platform was evaluated according to their features. Some were excluded due to their relatively large size, high supply current, small flash or RAM size or small number of GPIO pins (see crossed out parameters in Table 4-2).

Of the five remaining microcontrollers, the Atmega168PA from Atmel and the MSP430F2132 from Texas Instruments had the lowest power consumption. The Atmel microcontroller had more memory than the one from TI.

Using the MSP-type microcontroller from Texas Instruments would allow for adaption of the manufacturer source code which was written for an MSP430F1611. A single integrated development environment (IDE) could be used if one microcontroller type was used system wide.

The MSP430F2132 met the minimum memory requirements and the size could be minimized by wire bonding directly to the die instead of using the QFN-32 package. Therefore, the *MSP430F2132* was chosen, allowing faster software development.

---

code reduced flash size to just below 7 kB. Some additional space would be required for application functions.

Product	Texas Instruments					µChip		Atmel			
Parameter	MSP430F2012	MSP430F1232	MSP430F2132	MSP430F2274	MSP430F1611	PIC16F616	PIC16F690	ATmega168PA	ATtiny88	ATmega168V	ATmega165PV
Voltage[V]	1.8-3.6	1.8-3.6	1.8-3.6	1.8-3.6	1.8-3.6	2.0-5.5	2.0-5.5	1.8-5.5	1.8-5.5	1.8-5.5	1.8-5.5
Current[7] [µA]	300	300	350	390	~~500~~	185	220	350	390	417	~~610~~
Sleep Current[8] [µA]	0.1	0.1	0.1	0.1	0.2	0.15	0.15	0.1	0.15	0.3	0.2
Flash [kByte]	~~2~~	8	8	32	48	~~2~~	~~7~~	16	8	16	16
RAM [Byte]	~~128~~	~~256~~	512	1024	10240	~~128~~	~~256~~	1024	512	1024	1024
EEPROM [Byte]	-	-	-	-	-	-	256	512	64	512	512
Digital Output Pin[9]	~~0~~	8	8	15	34	~~0~~	4	14	14	11	40
ADC [bit]	8x10	8x10	8x10	12x10	8x12	8x10	12x10	8x10	8x10	8x10	8x10
Serial Interface	SPI I2C	SPI	SPI I2C	SPI I2C	SPI I2C	-	SPI I2C	SPI I2C	SPI I2C	SPI I2C	SPI
Package type	QFP-16	QFN-32	QFN-32	QFN-40	QFN-64	QFN-16	QFN-20	MLF-32	MLF-32	MLF-32	QFN-64
Dimensions [mm]	4x4	5x5	5x5	6x6	~~9x9~~	4x4	4x4	5x5	5x5	5x5	~~9x9~~
Remarks	ADC/SPI share pins	no internal LF Osc.		4x diff. OpAmp	2x12bit DAC, DMA	5V regulator	ADC/SPI share pins				

Table 4-2: Evaluation microcontroller, parameters not meeting minimum requirements are crossed out

---

[7] Supply current when CPU active with system clock = 1 MHz and supply voltage = 3 V

[8] All clocks off, respond to external wakeup interrupt from ZL70101

[9] General Purpose Input/Output pins, excluding 8 used for ADC and 6 used for ZL70701 interface (4 SPI + 1 interrupt + 1 wakeup control).

4.2.2 Power Considerations

Most of the power required by the sensor platform is to power the *wireless transceiver* (supply current in Table 4-3). The *sensors* also draw a significant amount of power, depending on their type. The strain gauge type sensors used by Lou et al. [22] required about 6.3 mW. The following paragraphs show how the sensor interface was designed to reduce the average power consumption of the sensors. Furthermore, the minimum power required by the wireless transceiver is calculated.

The *sensors* should only be powered when measurements are taken and turned off for the remaining time to save power. The sensor platform provides a digital output (EN on the schematic in Appendix A-1) to toggle power to the sensors. This EN output is controlled by the sensor interface according to Figure 4-5.
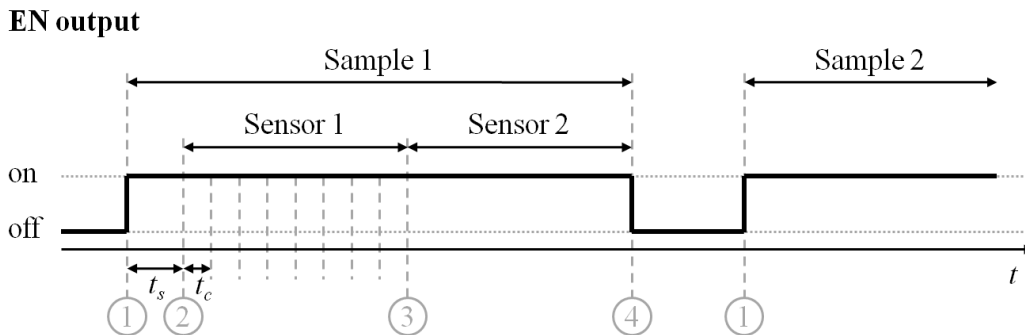
Figure 4-5: Sensor power enable output waveform when sampling 2 sensors. 1) turn on sensors, 2) perform 8 ADC conversions for first sensor, 3) perform 8 ADC conversions for second sensor, 4) turn off sensors

When the sensor platform receives the command to take a sample, the EN pin is turned on (#1 in Figure 4-5). The program then pauses for up to 1280 µs to allow for the sensor output to stabilize. Eight consecutive analog-to-digital conversions are then performed for the first sensor and the average is stored (#2 to #3 in Figure 4-5). These eight conversions are performed for each sensor. The EN pin is then turned off and the result of all conversions is sent to the base station (#4 in Figure 4-5). When the next sample command is received, the entire procedure is repeated.

If sample commands are received periodically every τ seconds, the duty cycle d_s of the sensors can be defined as

(4-3)
$$d_s = \frac{t_{on}}{\tau}$$

42

with t_{on} being the time it takes for a sample to complete. The sample time t_{on} is given by

$$(4\text{-}4) \qquad\qquad t_{on} = t_s + m \cdot t_c \cdot n$$

where t_s is the startup delay, m is the number of conversions that are averaged for each sensor and n is the number of sensors. The delay t_s can be programmed by the user to be $0 - 1280$ μs and $m = 8$ and $t_c = 6$ μs are constant system parameters. Inserting equation (4-4) into equation (4-3) and using the constant system parameters yields

$$(4\text{-}5) \qquad\qquad d_s = \frac{t_s + n \cdot 48 \mu s}{\tau}$$

The average power consumption $P_{s,ave}$ of the sensors connected to the sensor platform is given as

$$(4\text{-}6) \qquad\qquad P_{s,ave} = d_s \cdot P_S$$

where P_S is the power rating of the sensors.

If, for example, $t_s = 0$, $n = 8$ and $\tau = 0.1$ s (10 Hz), the average power consumption would be

$$(4\text{-}7) \qquad\qquad P_{s,ave} = \frac{0\mu s + 8 \cdot 48 \mu s}{100000 \mu s} \cdot 6.3 mW = \underline{0.024 mW}$$

The **wireless transceiver** should only be powered when data is transmitted. The average power consumption of the transceiver $P_{t,ave}$ can then be calculated similarly to the average power consumption of the sensors. The duty cycle d_t of the transceiver is given as

$$(4\text{-}8) \qquad\qquad d_t = \frac{b}{\tau \cdot r}$$

where b is the number of bits transmitted per sample and r [bit/s] is the data rate of the wireless link. The number of bits b is calculated based on the ADC resolution a [bit], the number of sensors n and the number of overhead bits h [bit]:

$$(4\text{-}9) \qquad\qquad b = h + n \cdot a$$

Substituting equ.(4-9) into equ.(4-8) and inserting the constant system parameters $h = 32$ bit, $a = 10$ bit and $r = 528000$ bit/s yields

(4-10)
$$d_t = \frac{(32bit + n \cdot 10bit)}{\tau \cdot 528000 \, bit/_s}$$

The average power consumption $P_{t,ave}$ of the wireless transceiver is then given as

(4-11)
$$P_{t,ave} = d_t \cdot P_t$$

where P_t is the power consumption of the transceiver. P_t is calculated from the supply current I_t at the supply voltage $V_{SUP} = 2.1$ V given in Table 4-3 as

(4-12)
$$P_t = V_{SUP} \cdot I_t = 2.1V \cdot 5mA = 10.5mW$$

When eight sensors $(n = 8)$ are sampled at 10 Hz $(\tau = 0.1 \text{ s})$, the average power consumption of the wireless transceiver $P_{t,ave}$ is

(4-13)
$$P_{t,ave} = \frac{(32bit + 8 \cdot 10bit)}{0.1s \cdot 528000 \, bit/_s} \cdot 10.5mW = \underline{0.022mW}$$

The total average power P_{ave} of the sensor platform is then at least

(4-14)
$$P_{ave} = P_{s,ave} + P_{t,ave} = \boxed{0.046mW}$$

4.2.3 Module Specifications

Table 4-3 lists specifications for the sensor platform module based on values given in the datasheet of individual components. Characteristics measured during experiments are listed in Chapter 5.

Physical dimensions			25 x 14 mm
Supply voltage V_{SUP}			2.1 – 3.5 V
Supply current	**Sleep Mode**	**Active Mode**	
		$V_{SUP} = 2.1$ V	$V_{SUP} = 3.0$ V
Microcontroller MSP430F2132	0.10 µA	250 µA	350 µA
RF transceiver ZL70101 (I_t)	0.65 µA	5 mA	5 mA
Total current consumption[10]	**0.75 µA**	**5.25 mA**	**5.35 mA**
Analog to digital converter	$V_{Ref} = 1.5$ V	$V_{Ref} = 2.5$ V	$V_{Ref} = V_{SUP}$
Input voltage	0 – 1.5 V	0 – 2.5 V	0 - V_{SUP}
Resolution	1.46 mV	2.44 mV	$V_{SUP}/1023$
Antenna impedance			50 Ω
Wireless frequency			402 – 405 MHz

Table 4-3: Sensor platform specifications

4.3 Base Station

The base station shown in Figure 4-6 contained a 2.45 GHz transmitter (CC2550, Texas Instruments), the same Zarlink wireless transceiver used on the sensor platform and a microcontroller (MSP430F1611, Texas Instruments) with 48 kB program memory. The transmitter CC2550 was used to wake up the sensor platform from the low power sleep mode by sending a wakeup command. The selected microcontroller on the base station provided more program memory and more input/output pins than the one on the sensor platform to accommodate the additional code and data lines necessary for the USB communication with a PC. The base station was powered entirely from the PC via the USB port. Circuit schematics can be found in Appendix A-3 to Appendix A-6.

---

[10] Total current consumption of the sensor platform does not include supply current to connected sensors.
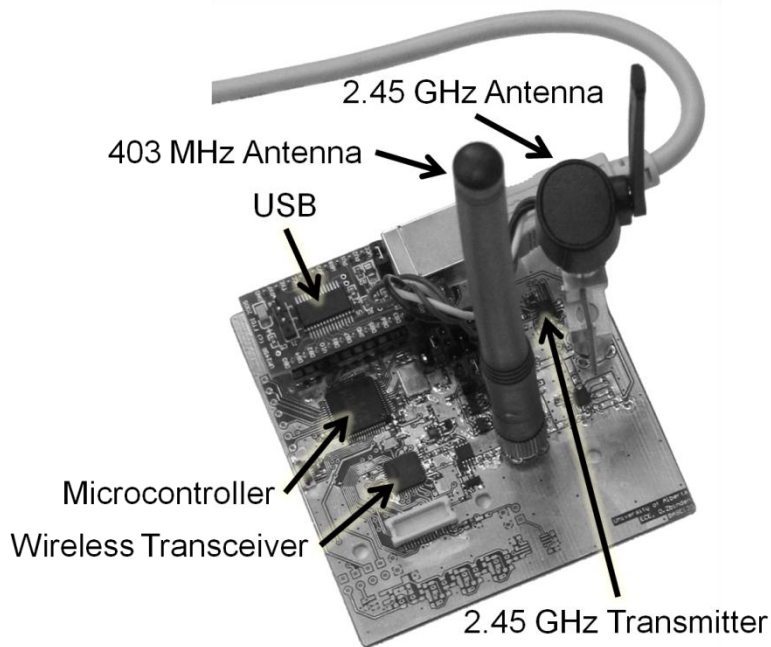
Figure 4-6: Base station

4.3.1 Module Specifications

Table 4-4 lists specifications for the base station module based on values given in the datasheet of individual components. Characteristics measured during experiments are listed in Chapter 5.

Physical dimensions	65 x 60 x 142 mm
Supply voltage (from USB)	5 V
Supply current @ V_{SUP} = 3.3 V	
Microcontroller MSP430F1611	0.6 mA
RF transceiver ZL70101	5.0 mA
RF transmitter CC2550	21.3 mA
RF amplifier MGA-412P8 (23 dBm)	200 mA
Total	**226.0 mA**
Wireless frequency data link	402 – 405 MHz
Wireless frequency wakeup	2450 MHz

Table 4-4: Base station specifications

4.4   Capacitive Power Storage

The capacitive power module shown in Figure 4-7 stored energy in three parallel electric double layer capacitors (EDLC). A step-up voltage converter was used to provide an output voltage at or above 2.1V. The following paragraphs discuss the supercapacitor and step-up converter selection, describe how connecting capacitors in parallel or in series affects their power storage capacity and list the capacitive power storage module specifications. Circuit schematics can be found in Appendix A-7.
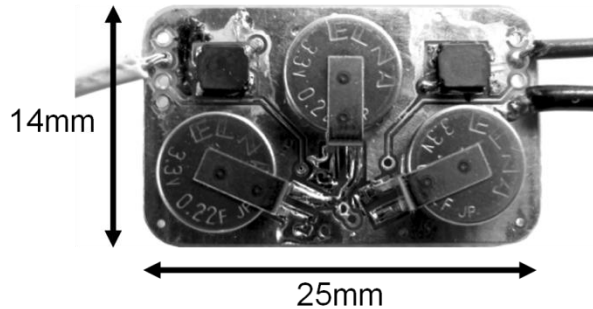
Figure 4-7: Capacitive power module with 3 EDLC's

4.4.1   Supercapacitor Selection

There was a wide variety of electric double layer capacitors (EDLCs) available. Elna, Inc.[11] and Cooper Bussmann[12] are two of the manufacurers that offered coin-sized cells for mounting on a printed circuit board. These EDLCs were available in different diameters and had a low profile which made them suitable for implantable devices. Table 4-5 lists EDLCs that had a diameter smaller than 10 mm.

The capacity was the amount of energy *J* stored in a fully charged capacitor, calculated with equation (2-6). The volume was calculated from the diameter and the height. The density was the capacity per volume.

The KS-2R8334 from Cooper Bussmann had the highest capacity, but it was not available at the time the prototype was designed. Therefore, the DCK-3R3E224 from Elna was used in the capacitive power storage module.

---

[11] Elna America, Inc., www.elna.co.jp/en/capacitor
[12] Cooper Industries, Inc., www.cooperbussmann.com/3/PowerStor.html

Product Parameter	Elna		Cooper Bussmann (PowerStor)	
	DCK-3R3E224	DC-2R5E224	KS-3R3224	KS-2R8334
Voltage [V]	3.3	2.5	3.3	2.8
Capacitance [mF]	220	220	220	330
Capacity [mWs][13]	1198	688	1198	1294
ESR [Ω] @ 1 kHz	200	100	200	100
Diameter [mm]	6.8	6.8	6.8	6.8
Height [mm]	2.1	2.1	2.1	2.1
Volume [mm^3]	76.3	76.3	76.3	76.3
Density [$^{mWs}/_{mm}{}^3$]	15.7	9	15.7	17

Table 4-5: Evaluation EDLC

4.4.2 Parallel vs. Series Connection

Several identical EDLCs can be connected either in parallel or in series in order to increase energy storage capacity. Figure 4-8 shows parallel and serially connected EDLCs, each represented by a capacitance C and an equivalent series resistance (ESR) R.
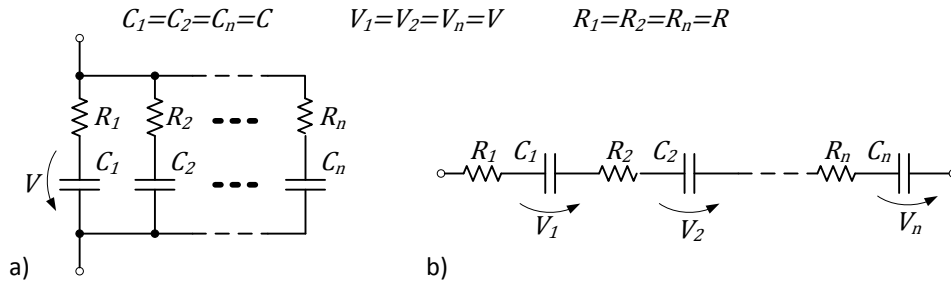
Figure 4-8: EDLC a) parallel connection, b) series connection

When connected in parallel, all capacitors share a common voltage V and the overall capacity C_P is the capacity of an individual capacitor C multiplied by the number of capacitors n.

(4-15)
$$C_P = nC$$

Inserting equation (4-15) into equation (2-6) gives the total energy J_p stored in the parallel connected capacitors.

---

[13] See equation (2-6)

(4-16)
$$J_P = \frac{1}{2} \cdot nC \cdot V^2 = \frac{n}{2} CV^2$$

When connected in series, the overall voltage is the sum of all individual voltages

(4-17)
$$V_S = nV$$

and the overall capacity is the capacity of an individual capacitor divided by n.

(4-18)
$$C_S = \frac{1}{n} C$$

Inserting equations (4-17) and (4-18) into equation (2-6) from Chapter 2 gives the total energy J_S stored in the serially connected capacitors.

(4-19)
$$J_S = \frac{1}{2} \cdot \frac{1}{n} C \cdot (nV)^2 = \frac{n}{2} CV^2$$

Equations (4-16) and (4-19) show the same amount of energy J can be stored in parallel and serial connected capacitors. However, there is a difference when it comes to the usable energy ΔJ.

Inserting equation (4-19) into equation (2-7) gives the usable work J_P stored in the parallel connected capacitors.

(4-20)
$$\Delta J_P = \frac{1}{2} \cdot nC \cdot \left[V^2 - V_2{}^2 \right]$$

Similarly, inserting equations (4-17) and (4-18) into equation (2-7) yields the usable work J_S stored in the serially connected capacitors.

(4-21)
$$\Delta J_S = \frac{1}{2} \cdot \frac{1}{n} C \cdot \left[(nV)^2 - V_2{}^2 \right]$$

Taking the difference ΔJ_{diff} of these two values will show whether they are equal or which one is higher.

(4-22)
$$\Delta J_{\text{diff}} = \Delta J_S - \Delta J_P$$

Substituting ΔJ_S with (4-21) and ΔJ_P with (4-20) gives

(4-23)
$$\Delta J_{\text{diff}} = \frac{1}{2n} C \left[(nV)^2 - V_2{}^2 \right] - \frac{n}{2} C \left[V^2 - V_2{}^2 \right]$$

and simplifying yields

(4-24)
$$\Delta J_{\text{diff}} = \frac{1}{2n} \left(n^2 CV^2 - CV_2{}^2 - n^2 CV^2 + n^2 CV_2{}^2 \right) = \frac{n^2 - 1}{2n} CV_2{}^2$$

The fact that the difference ΔJ_{diff} is positive means that serially connected capacitors provide more usable energy than parallel connected capacitors for equal capacitance C, rated votage V and number n.

However, one of the reasons for using EDLCs instead of batteries is their high current rating due to their low ESR. When EDLCs are connected in parallel, the overall ESR R_P is reduced even further to

(4-25)
$$R_P = \frac{1}{n} R$$

where n is the number of parallel EDLCs and R is the ESR of an individual EDLC. The overall ESR R_S of serially connected EDLCs is given by

(4-26)
$$R_S = nR$$

The lower overall ESR of EDLCs connected in parallel reduces thermal losses and voltage drops and thus allows for sourcing higher currents as well as higher charging currents. The charging current i_c of a capacitor is given by

(4-27)
$$i_c(t) = \frac{V}{R} e^{-t/RC}$$

with the maximum current i_0 at $t = 0$ given as

(4-28)
$$i_0 = \frac{V}{R}$$

Minor differences of internal resistance between individual capacitors would result in an unequal distribution of the applied charging voltage over these individual capacitors, if they are connected in series. Since the EDLC's have to be charged up to their rated voltage for maximal energy storage, this imbalance would result in an overvoltage over some individual capacitors which in turn may result in permanent damage to this capacitor.

Also, the voltage rating of the charging and discharging circuit for parallel connected EDLC's remains constant if the number of individual EDLC's changes. This means that the overall capacity could be changed easily by varying the number of EDLC's without having to redesign the rest of the circuit.

Therefore, the EDLC's in the capacitive power storage module were connected in parallel.

4.4.3 Step-up Converter Selection

The step-up converter had to boost the EDLC voltage to provide a minimum supply voltage $V_{SUP} \geq 2.1$ V to the sensor platform circuit. An important parameter was the minimum input voltage to the step-up converter to provide the output voltage. The lower the minimum input voltage V_{IN}, the more of the energy stored in the EDLC could be used. This can be shown substituting V_2 with V_{IN} in equation (2-7).

(4-29)
$$\Delta J = \frac{1}{2} C \left(V_1{}^2 - V_{IN}{}^2 \right)$$

The TPS61220 from Texas Instruments was chosen because of its low minimum input voltage $V_{IN} = 0.7$ V, high conversion efficiency (up to 74% when $V_{IN} = 0.7$V), low quiescent current and small physical size of 2 x 2 mm (excl. external components).

4.4.4 Module Specifications

Table 4-6 lists specifications for the capacitive power module based on values given in the datasheet of individual components. Computed values such as the energy storage capacity are based on ideal models and do not include any losses. Characteristics measured during experiments are listed in Chapter 5.

Physical dimensions		14 x 25 x 5 mm
Capacitance		990 mF
Charging voltage		3.3 V
Energy storage capacity (J)		5.39 Ws
Energy storage capacity usable (ΔJ)[14]		5.15 Ws
Output voltage		2.1 – 2.8 V
	$V_{CAP} > 0.7$ V	$V_{CAP} > 1.6$ V
Output current	40 mA	100 mA

Table 4-6: Capacitive power storage specification

---

[14] EDLCs discharged to 0.7 V, disregards resistive losses, voltage converter efficiency, voltage converter quiescent current

4.5 Transcutaneous Energy Transfer

Power is a major concern in wireless implantable devices because the wireless communication circuitry requires a lot of power. Miniaturizing the physical size of implantable devices does not leave much room for power storage in batteries or capacitors. The proposed system employs power saving data transmission protocols and low power standby modes in order to extend operation time. An inductive power transfer circuit is suggested. The design of this transcutaneous energy transfer system is outside of the scope of this thesis. Wired connections were used for testing purposes instead.

4.6 Software Implementation

Software was developed to test the wireless link functionality and verify the data acquisition procedure. It can be extended to support the analysis and administration of data in a relational database. The software consisted of three main parts depicted in Figure 4-9. The user interface running on a Windows 7, Vista or XP operating system allowed a user to configure the system and display and store collected data. The embedded software running on the base station configured the wireless link and relayed commands between the user interface and the sensor platforms. The embedded software running on a sensor platform responded to user commands received via the wireless link.

Figure 4-9: Software overview

The software was modified based on the source code provided by Zarlink (ADK 1.2.0) under a non disclosure agreement. The modified source code was developed to work with our specific hardware design and functionality. The following paragraphs describe the contribution made to build on the Zarlink source code.

The *windows software* has a new user interface and added data storage capability. Most of the hardware specific back-end functionality including the DLL and the API classes remain almost unchanged. API classes were extended to support data binding.

The *base station embedded software* originally running on two microcontrollers was modified so it could run on a single MSP430F1611 microcontroller. Support for the wireless link to be used as a command interface was added.

The *sensor platform embedded software* was adapted to run on a microcontroller with significantly less program memory. Support for the wireless link to be used as a command interface and sensor configuration functionality was added

The software structure is shown in greater detail in Figure 4-10. Each rectangle represents a software module. Software modules can be a collection of functions in C or a class in C#. Modules contain sub-modules where the sub-module is only accessed through the parent module by any other part of the software. Modules interact with each other through function calls represented by solid arrows or interrupts represent by dashed arrows.
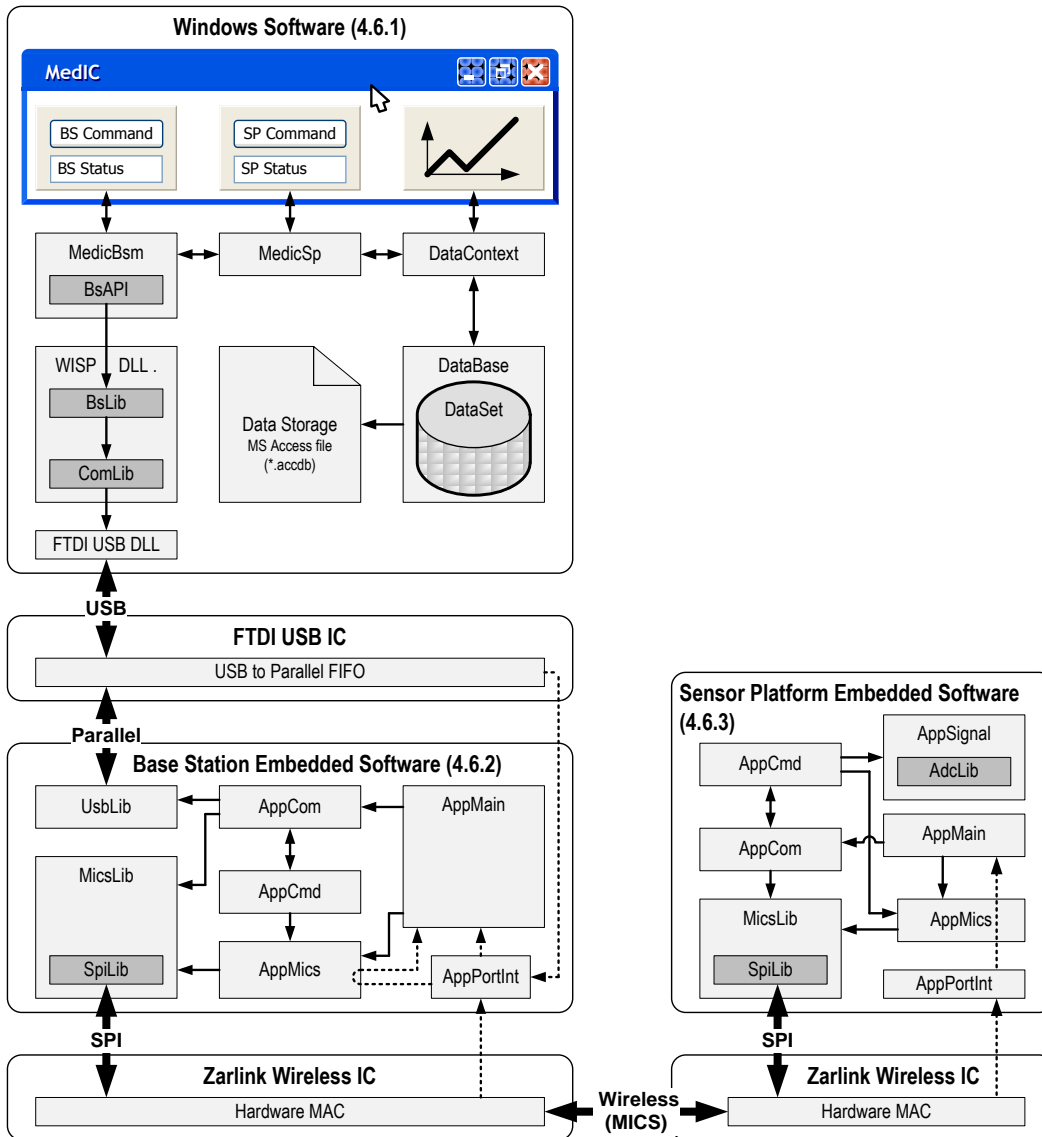
Figure 4-10: Software structure

4.6.1 Windows Software

The windows software at the top left in Figure 4-10 was developed using the Microsoft Visual Studio 2008[15] environment. The structure was built with modules to allow for expansion by adding modules and modifications of existing modules without having to change the entire program.

---

[15] Microsoft Visual Studio 2008, version 9.0.21022.8 RTM with Microsoft .NET framework version 3.5 SP1

The user interface is labeled *MedIC*, short for **Med**ical **I**mplant **C**ontrol, in Figure 4-10. It consisted of a main program window and six user control elements labeled 1 through 6 in Figure 4-11.
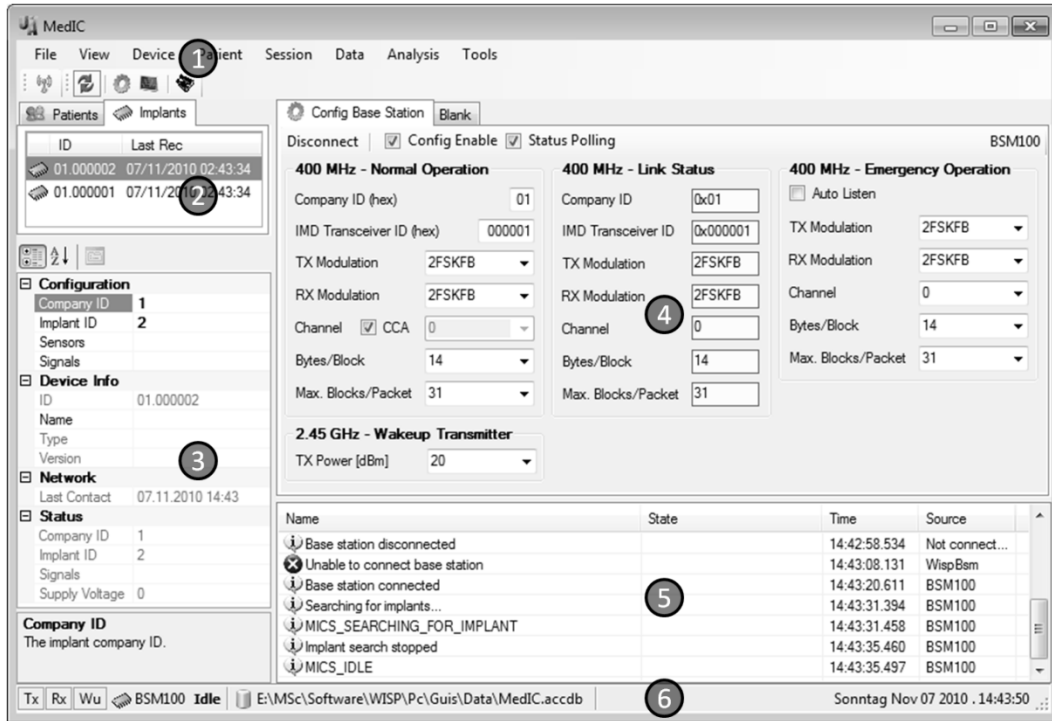
Figure 4-11: User interface with configuration form with 1) menu bar, 2) implant/patient list, 3) list item properties, 4) control area, 5) program log, 6) status bar

1) The menu bar provided access to the main program functions, and open user control forms at location 4 in Figure 4-11.

2) The implant/patient list could be switched between a list of patient files and a list of implant devices within the communication range of the base station. The patient file list allowed navigating through data stored in the database. The implant list was updated automatically when the base station searched for implants and showed any ZL70101 transceiver within the communication range.

3) The list item properties provided more details of the currently selected patient or implant in the list view (2).

4) The control area displayed multiple .Net user controls (forms, tables, graphs, etc.) organized in tabs. The user interface functionality could be easily expanded by adding a new .Net user control. Some implemented controls included a

55

configuration form for the base station (shown in Figure 4-11), a communication terminal for wireless data exchange and a data table to view raw data in the database.

5) The program log listed important events for example when a base station was connected and error messages for example when no base station was found.

6) The status bar showed the current operating status of the base station such as "Idle" or "Searching for implants" and the connection status of the data base.

The user interface interacted with the back-end modules through function calls and data binding. These back-end modules are shown below the user interface in Figure 4-10 and described in more detail below.

The *MedicBsm* module was a representation of the base station state in PC RAM. The module kept track of the actual state by frequently polling and storing parameters such as wireless channel or data rate from the hardware. It provided a command interface to the rest of the software by importing the *WISP DLL* functions into managed code. This module contained a list of associated sensor platforms which were represented by an individual *MedicSp* module. Similar to the *MedicBsm* module, the *MedicSp* module was a representation of the state of a sensor platform in PC RAM.

The communication with the base station passed through several abstraction layers on the left side in Figure 4-10. The *WISP DLL* module contained the *BsLib* and *ComLib* modules. The BsLib module implemented base station specific maintenance functions for connecting to or disconnecting from the hardware. It also assembled command packets to be sent through USB when the corresponding command functions were called. The *ComLib* module implemented the communication protocol available from Zarlink Inc. under a Non-Disclosure Agreement.

Basic USB functionality was handled by the *FTDI USB DLL* provided by FTDI Ltd.[16]. This DLL implemented low level functions to recognize plugged in base stations and transmit and receive bytes.

---

[16] Future Technology Devices International Ltd. (FTDI), www.ftdichip.com

Data storage was managed on the right side in the windows software section in Figure 4-10. The *DataContext* module kept track of related data samples and configuration values. It contained all the necessary information to relate a data value to the patient, session, sample, device and sensor information (see data base description below).

The *DataBase* module held a local copy of the relational data base in a *DataSet*. It provided all the functionality necessary ensure data integrity and synchronize the DataSet with a Microsoft Access file that served as persistent data storage. The database was designed to allow for future statistical analysis such as finding maximum force values. Figure 4-12 shows the database structure with individual data tables and relationships.
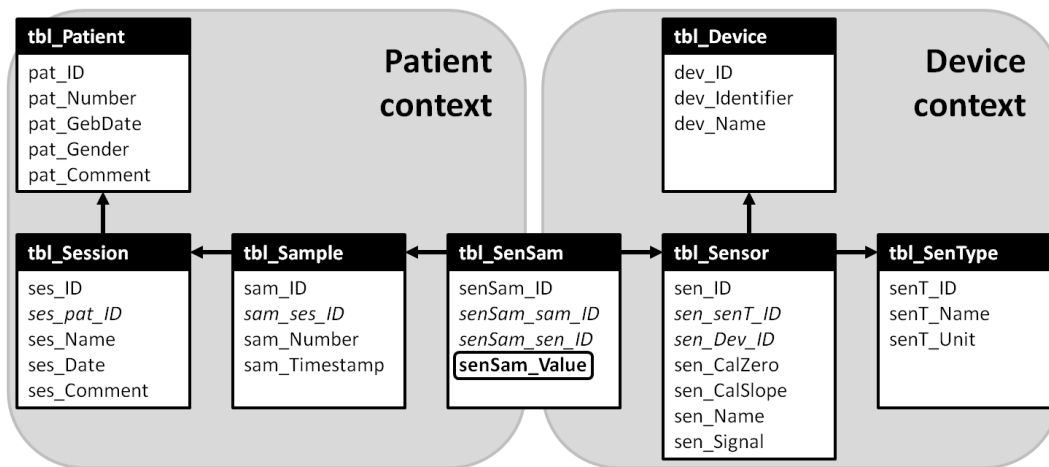
Figure 4-12: Relational database table structure

Before describing the database structure in more detail, some terms need to be defined. A *device* was a sensor platform uniquely identified by its identifier and name. A *sensor* was a single sensor or transducer connected to the sensor platform. A *sample* was a collection of all sensor values from a device at a particular point in time. A *session* was a series of related samples. Related samples were all samples that were taken between a start sample and a stop sample command.

The data base can be divided into two parts, the patient context and the device context. The device context is used when communicating with sensor platforms and processing received force data while the patient context is used to manage patient records and analyze force data. Collected data values were stored in the highlighted *senSam_Value* attribute of the *tbl_SenSam* table in the center of Figure 4-12.

The patient context associated the data value with a sample, a sample with a session and a session with a patient. This formed a tree structure with each patient having multiple sessions, each session containing multiple samples and each sample containing multiple sensor values. In order to ensure patient privacy, no patient names were stored in the database. Instead, a patient number attribute was provided which could be used to link to an external, secure patient database.

The device context associated each data value with a sensor and a sensor with a sensor platform device. This formed a tree structure with each sensor platform device having multiple sensors connected to it and each sensor having a history of multiple sample values taken over time. Storing the uncalibrated raw data in *tbl_SenSam* (*senSam_Value* attribute) and the calibration data for each sensor in *tbl_Sensor* provided more flexibility than if the calibration had been stored on the sensor platform and only the end result had been transmitted to the PC. This way, changes in the calibration could be post-applied to older data if necessary. The two calibration parameters *sen_CalZero* and *sen_CalSlope*s allowed for a two-point calibration of the sensors. More calibration parameters could be added for nonlinear sensor.

4.6.2 Base Station Embedded Software

The base station embedded software at the bottom left in Figure 4-10 was developed with Code Composer Essentials[17] and written in C. It was running on a MSP430F1611 microcontroller from Texas Instruments Inc. The two main tasks of the embedded software were to configure the wireless link and forward command packets from the USB to the wireless link and vice versa.

The *UsbLib* module shown in Figure 4-10 provided low level access to the USB interface for communication with the Windows software. The *MicsLib* module used the *SpiLib* module to control the Zarlink transceiver. It implemented low-level functions to configure the transceiver and transmit data.

The *AppCom* module implemented the communication protocol described in section 4.6.4. It handled incoming command packets by either passing them on to the *AppCmd* module if they were addressed to the base station or else forwarding them. Command packets were forwarded to the wireless interface if they arrived through USB and vice

---

[17] Texas Instruments Code Composer Essentials for MSP430, version 3.2.4.3.8

versa. The *AppCmd* module executed commands that were addressed to the base station, mainly to configure the wireless link. The *AppMics* module implemented high-level functions used to configure the wireless link and kept track of the wireless link state.

The *AppMain* module initialized the hardware at start-up and scheduled sub-processes during run-time. The *AppPortInt* module captured hardware interrupts and notified the *AppMain* module.

4.6.3 Sensor Platform Embedded Software

The sensor platform embedded software at the bottom right in Figure 4-10 was developed with Code Composer Essentials[17] and written in C. It was running on a MSP430F2132 microcontroller from Texas Instruments Inc. The main task of the sensor platform embedded software was to respond to user commands received via the wireless link.

The modules interfacing with the Zarlink transceiver (*SpiLib* and *MicsLib*) were identical to those used in the base station embedded software. The *AppCom* module still implemented the communication protocol, but only for the wireless link. The *AppCmd* module implemented the sensor platform specific commands listed in Table 4-8.

The *AppPortInt* module captured hardware interrupts and notified the *AppMain* module. The *AppMics* module implemented high-level functions used to configure the wireless link and kept track of the wireless link state. The *AppMain* module initialized the hardware at start-up and scheduled sub-processes during run-time. It was optimized for low-power operation. The *AppSignal* module allowed for flexible software configuration of the sensor interface. It used the AdcLib module to configure the analog-to digital converters (ADC). Details of the signal interface are described below.

Signal Interface

The signal interface shown in Figure 4-13 supported 8 individual external sensor inputs and internal temperature and supply voltage measurements. The number of signals to be measured, reference voltages and measurement delays could be reconfigured during operation. Two address lines permit the use of external multiplexers to support the 32 signals generated by the MEMS-transducers on one instrumented hook or screw head. Three different reference voltages including the supply voltage Vcc and 1.5 V / 2.5 V from the internal reference voltage generator could be selected to sample individual

sensor voltages. Choosing a lower reference voltage for sensors with a lower output range would increase the sensitivity of the measurement (see ADC specifications in Table 4-3). All voltages were measured relative to a common ground potential.
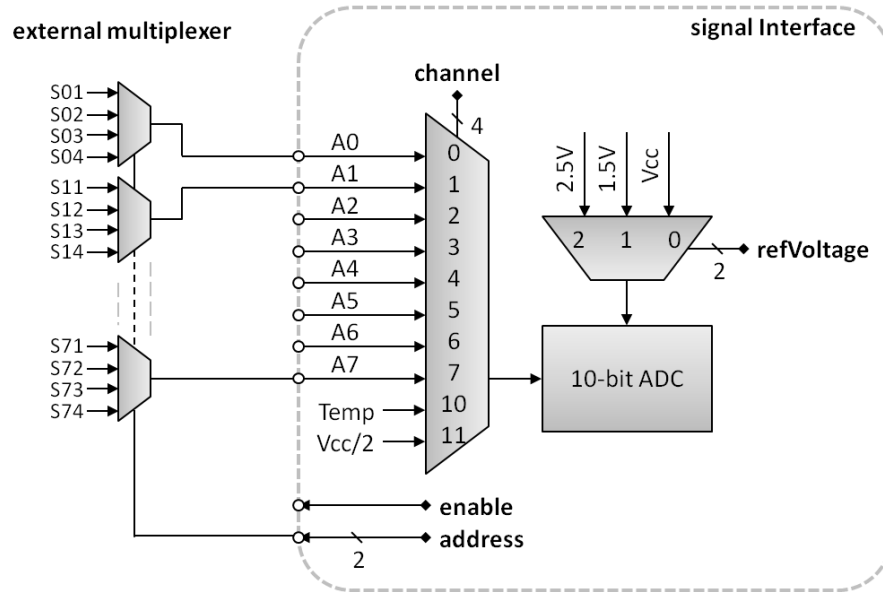
Figure 4-13: Signal interface

The signal interface was configured by sending the command *SetSignalsConfig* to the sensor platform. The command contained a two-byte structure for each of up to 34 signals that could be measured. The structures contained the fields listed in Table 4-7.

field name	bits	description	values
delay	7	Delay in microseconds/10 after the address pins were set and before the ADC conversion was started. This delay allowed the sensor output voltage to stabilize.	$0 - 2^7 \rightarrow$ $0 - 1280$ µs
enable	1	Enable pin to control power to the external sensors.	$0, 1 \rightarrow$ low, high
channel	4	Channel number to select signal source. Source could be external pins, internal temperature sensor or supply voltage.	$0 - 7, 10, 11 \rightarrow$ Pin A0 – A7, Temp, Vcc
address	2	Address pins to control external multiplexer.	$0 - 3$
refVoltage	2	Positive reference voltage used for the ADC conversion. Note: negative reference was always the common ground potential.	$0, 1, 2 \rightarrow$ Vcc, 1.5 V, 2.5 V

Table 4-7: Signal configuration structure

4.6.4 *Communication Protocol*

The *Windows software*, *base station embedded software* and *sensor platform embedded software* communicated with each other through USB and a wireless link. Commands were exchanged through a packet based protocol. Protocol details are available from Zarlink Inc. but cannot be published due to a Non-Disclosure Agreement.

Commands were identified by a unique 8 bit command type number in the command header. This allowed for the implementation of $2^8 = 256$ unique commands. Table 4-8 lists commands implemented by the *sensor platform embedded software*. These commands were generated by the windows software and forwarded to the sensor platform via the base station. Some command packets included data in the command body.

Command Type		Description
4	GetMicsConfig	Get wireless link configuration. Report wireless parameters such as channel or data rate.
5	SetMicsConfig	Configure wireless link. Set wireless parameters such as channel or data rate.
32	GetSignalsConfig	Get signal configuration from sensor platform. Report signal interface configuration. See Figure 4-13 and Table 4-7 for more details.
33	SetSignalsConfig	Configure signals on sensor platform. Set signal interface configuration. See Figure 4-13 and Table 4-7 for more details.
34	GetSample	Measure all signals. Report the current values of all signals.
35	GetSignal	Measure signal value. Report the current value of the signal specified by a signal number.
36	GetSupplyVoltage	Measure supply voltage. Report the current value of the supply voltage.
121	GetDevType	Get device type string. This string identified the hardware type and version. This information was used by the Windows software to determine compatibility and match the sensor platform to an appropriate device object in memory.
122	GetDevName	Get device name string. This string was used to match a sensor platform to information stored in the Windows software database.
123	GetDevVer	Get device version string. This string identified the embedded software type and version. This information was used by the Windows software to determine compatibility and match the sensor platform to an appropriate device object in memory.

Table 4-8: Sensor platform command list

The sensor platform processed commands and replied with one of the command types listed in Table 4-9.

Command Type		Description
0	OkReply	Command successful. This reply was sent if a command was processed successfully. If data was requested in the original command from the windows software, the reply packet would contain result data.
127	ErrReply	Command failed. This reply was sent if an unknown command was received or an error occurred while processing a command.

Table 4-9: Sensor platform response list

Chapter 5

Prototype Verification and Test Results

To validate the functionality and the hardware design of the prototype, experiments were performed to determine: the accuracy of the internal temperature sensor, the accuracy of the ADC, the power consumption, the wireless communication range and the charge and discharge characteristics of the power module.

5.1 Sensor Platform

5.1.1 Temperature Sensor Accuracy

Normally, there is a sensitivity effect on the MEMS sensors when the temperature changes from room temperature (22 °C) to body temperature (37 °C) [85, 86]. Therefore, the capability of measuring temperature on the system can provide sensitivity compensation, which means more accurate measurements from MEMS sensors can be obtained. This experiment was to investigate the accuracy of the built-in temperature sensor inside the microcontroller MSP430F2132. Using the internal temperature sensor has the advantage of reducing the size and weight of the system. The accuracy of the internal temperature sensor was evaluated by comparing it with a low power temperature sensor (LM94022, National Semiconductor) which was soldered close to the microcontroller on the prototype sensor platform. A thermo couple from a multimeter (Fluke 179 True RMS Multimeter with Fluke 80BK-A) was also used as a reference for temperature measurements. The thermocouple was attached to the ground plane of the sensor platform and close to both the external and internal temperature sensor.

To determine the stability and differences of the temperature measurements from both internal and external sensors relative to the reference (from the multimeter), a series of temperature measurements were taken at room temperature at an interval of 15 seconds for 30 minutes. Then, the accuracy of the sensors over a range of temperature from room

temperature (23ºC) to 50ºC was tested. The sensor platform was placed inside an oven and heated gradually. Measurements were taken at an interval of 1 second over a period of 3 hours 30 minutes.

Table 5-1 reports the resolution and summarizes 121 measurements at room temperature from all 3 sensors. Although the internal sensor had a lower resolution than the external sensor, the accuracy of the internal sensor was higher than the external sensor by comparing with the reference value (from the thermal couple), -0.2ºC vs 1.65ºC.

n=121	Resolution[a]	Average ± SD	Offset[b]
reference	0.10 °C	22.30 ± 0.10 °C	-
External	0.18 °C	23.95 ± 0.12 °C	1.65 °C
Internal	0.42 °C	22.10 ± 0.15 °C	-0.2 °C

a. from device datasheets

b. Offset = (external | internal) – reference

Table 5-1: Temperature resolution, average, standard deviation and offset

Figure 5-1 shows the temperature variations when the platform was heated inside the oven. The measurements shown are compensated results where the offset value found in Table 5-1 has been subtracted on both sensors' measurements. Both sensors showed a similar temperature profile, except when the temperature changed rapidly. This discrepancy might be due to the fact that the external sensor was more sensitive to sudden temperature changes.
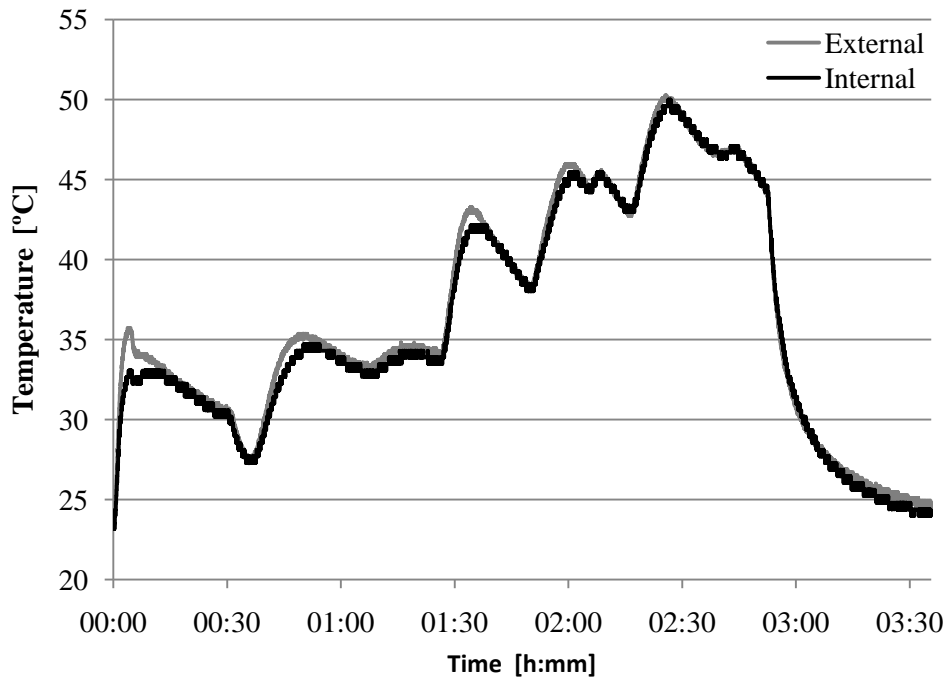
Figure 5-1: Temperature variations when heated inside oven

Even though the resolution of the internal temperature sensor was not as high as the external sensor, the accuracy of the internal sensor was better and sufficient to calculate the temperature compensation of any piezoresistive sensors due to temperature change. Therefore, an external temperature sensor was not necessary.

5.1.2 ADC Accuracy

The analog to digital converter (ADC) of a microcontroller plays an important role on the sensor platform as it converts the analog sensor output voltages into a digital number. It is, therefore, important that the ADC produces accurate and repeatable results independent of external influences such as temperature or supply voltage variations. A laboratory power supply was used to power the sensor platform as well as generating input voltages. The internal 1.5 V reference voltage was used for all ADC conversions. First, the ADC linearity was tested by applying an input voltage varying from 0 V to 1.5 V in steps of 0.1 V. Second, the ADC stability was tested over a supply voltage range from 2.1 V to 3.5 V in steps of 0.1 V with a constant input voltage at approximately 1 V. Finally, the ADC stability was tested over the temperature from room temperature to about 45 °C using a heat gun.

66

Figure 5-2 shows a good linearity ($R^2 = 1$) of the microcontroller ADC when the internal 1.5 V reference was used. The sampling resolution was 10 bit which resulted in a resolution of 1.5 V / (2^{10}-1) = 0.0015 V.
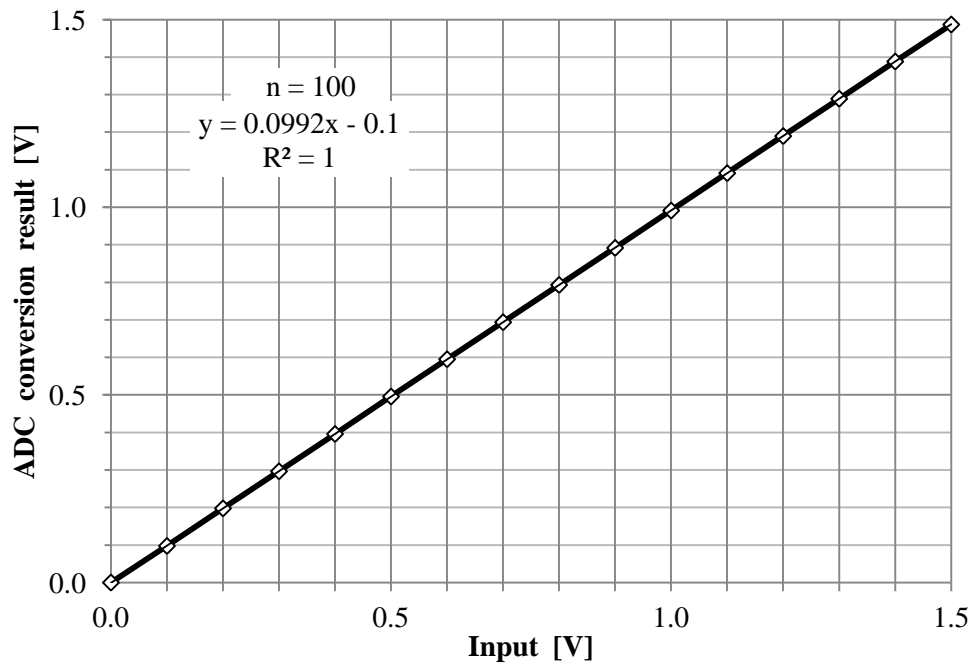
Figure 5-2: ADC Linearity

Figure 5-3 shows the variation of the ADC result (1.053 V ± 0.0012 V) when a constant input voltage of approximately 1 V was measured. The standard deviation of 0.0012 V over the entire supply voltage range (2.1-3.5 V) was smaller than the ADC resolution (0.0015 V).
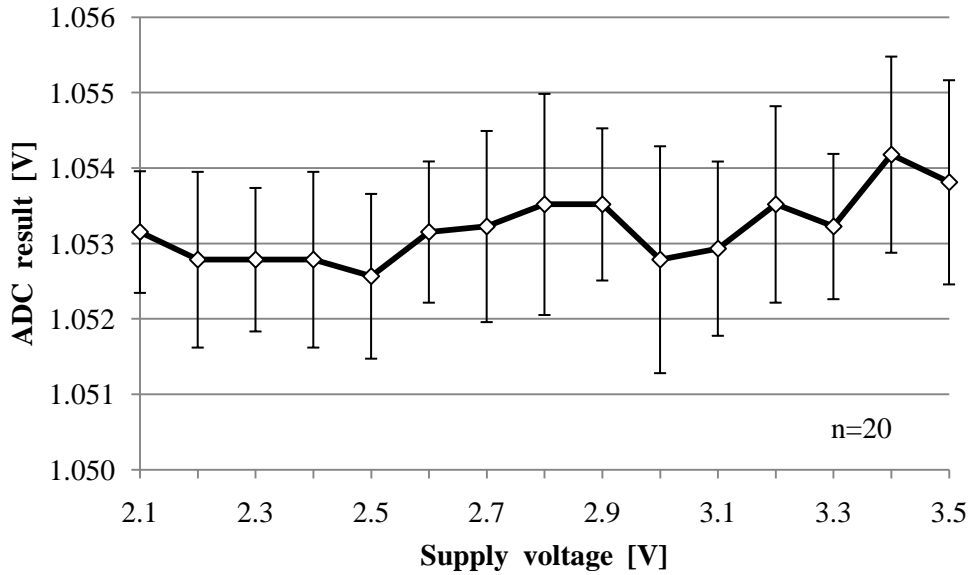
Figure 5-3: ADC stability with changing supply voltage, error bars show standard deviation of the 20 measurements taken at each supply voltage step.

The ADC result was also independent of the temperature when a constant input voltage of 1 V was measured (Figure 5-4). The standard deviation of 0.0007 V over the entire temperature range (20-45 °C) was smaller than the ADC resolution (0.0015 V).
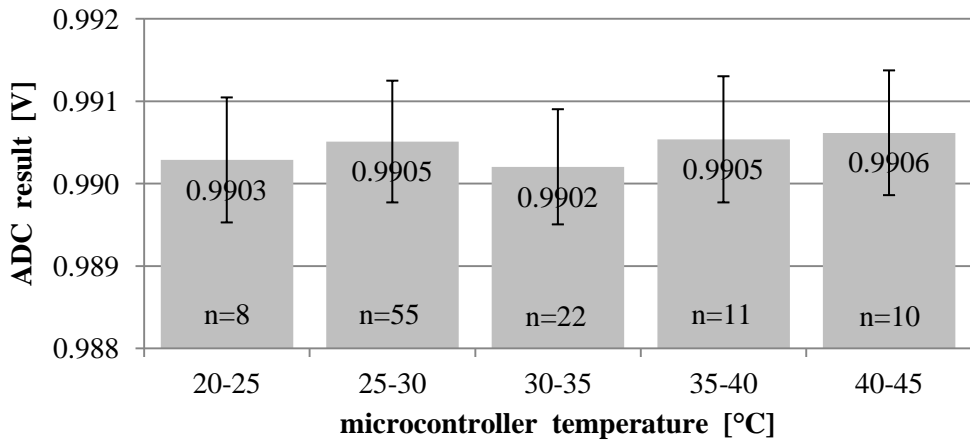
Figure 5-4: ADC stability with changing temperature, error bars show standard deviation of the measurements taken in each temperature range.

5.1.3 Power Consumption

The average power consumption of the sensor platform, with no sensors connected, was measured in the two main modes of operation, during active communication with the base station and while in sleep mode. A laboratory power supply applied a 1 V test

voltage to the ADC inputs of the sensor platform to simulate the sensors. In active mode, the wireless transceiver was turned on and the base station was requesting samples from the sensor platform at a frequency of 10 Hz. In sleep mode, the sensor platform powered down the 403 MHz radio but kept listening for wakeup commands in the 2.45 GHz band. The microcontroller was also powered down, but the internal timer kept running for debug purposes. A Fluke 867B Graphical Multimeter measured the supply current at 2.1 V and averaged it over a period of 10 minutes in both modes.

In sleep mode, the sensor platform drew an average current of 0.17 mA at 2.1 V, resulting in 0.36 mW power consumption. The sleep current is considerably higher than minimum possible value calculated in Table 4-3 because the microcontroller woke up periodically to handle tasks for test purposes. These tasks will not be included in the final program and the microcontroller will only be woken up when the base station initiates a communication link. In active mode, while sampling at 10 Hz, the average current draw was 5.26 mA, resulting in 11.05 mW power consumption. The active current corresponds well with the number calculated in Table 4-3.

5.2 Wireless Link

5.2.1 Sensor Platform Antenna Performance

The surface-mountable chip antenna used on the sensor platform was originally designed for 403 MHz. Since it would also be required to receive the 2.45 GHz wakeup signal, an experiment was performed to determine the antenna performance at that frequency. Figure 5-5 shows the experiment setup with a spectrum analyzer (BK Precision 2650, B&K Precision Cop.) on the left and the base station (BSM100, Zarlink Inc.) on the right.
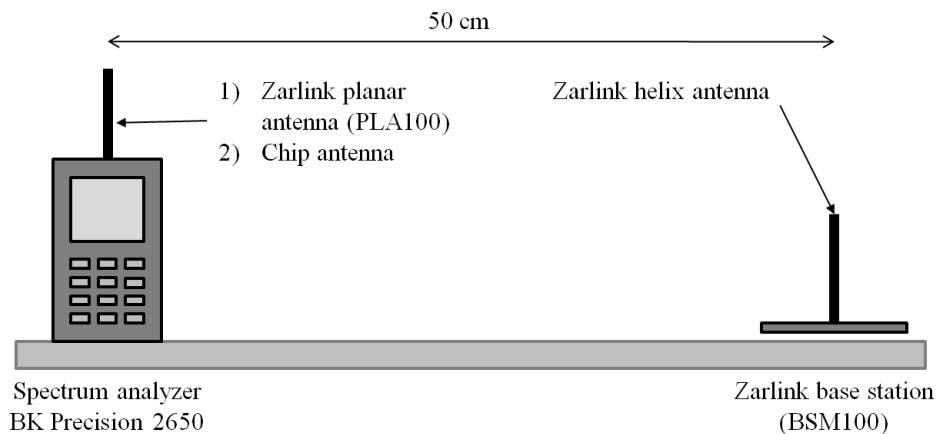
Figure 5-5: Sensor platform antenna performance test setup

The base station transmitted a carrier signal at 2.45 GHz which was received by the spectrum analyzer. The signal strength received by the spectrum analyzer through the chip antenna was compared to the signal strength with the planar antenna, which served as a reference, and no antenna connected. Both antennae were oriented with their largest area facing the base station antenna 50 cm away. The spectrum analyzer averaged 20 measurements for each frequency point.

Figure 5-6 shows the received power as a function of the frequency in decibel (dB) relative to the peak power received by the planar antenna. The peak power for the chip antenna was 2 dB below that of the planar antenna and 25.6 dB higher than when no antenna was used. This indicates that the selected chip antenna can be used to receive the 2.45 GHz wakeup signal.
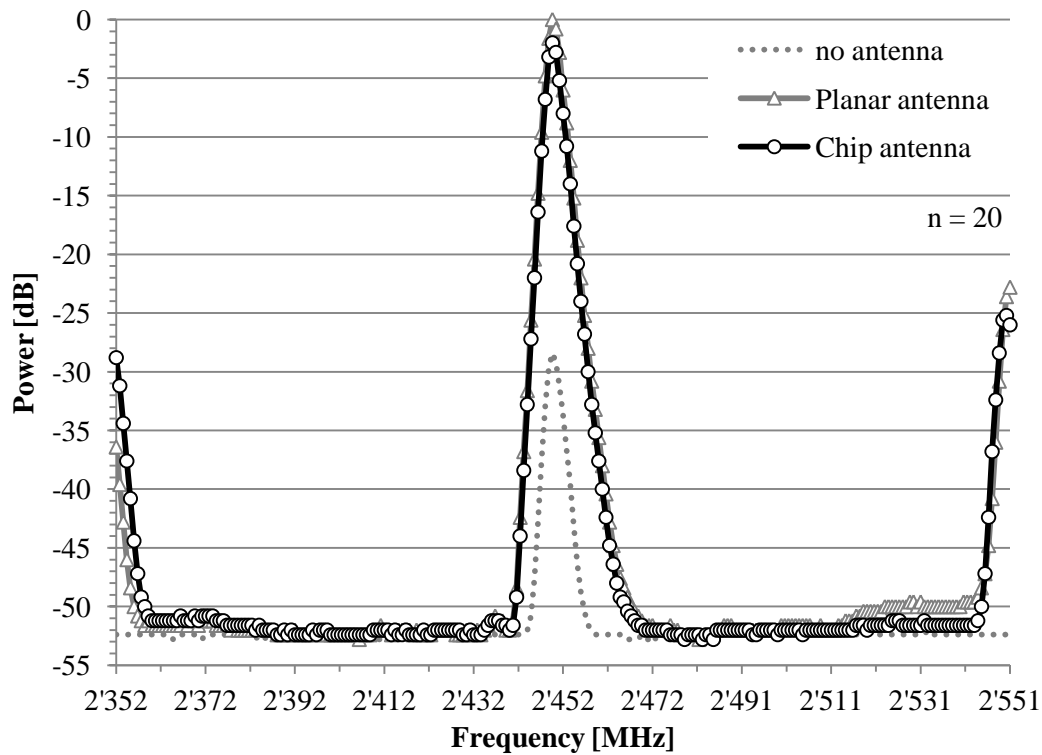
Figure 5-6: Sensor platform antenna performance @ 2.45 GHz

5.2.2 Free-Air Communication Range

When used in the operating room, the sensor platform will have to transmit data from the operating table to the base station about 2 m away. The communication range was tested in an office environment with a direct line of sight between sensor platform and base station. The sensor platform was placed at increasing distances from the base station in steps of 1 m. At each step, the base station tried to initiate a wireless link 10 times and the number of successful connections was noted. A successful attempt included waking up the sensor platform within 4 seconds using the 2.45 GHz wakeup signal and receiving a response on 403 MHz. The entire procedure was repeated 14 times.

The wireless communication was found to be 99% reliable in the targeted range of 2 m and still 74% reliable up to a range of 4 m with a direct line of sight between base station and sensor platform (Figure 5-7).
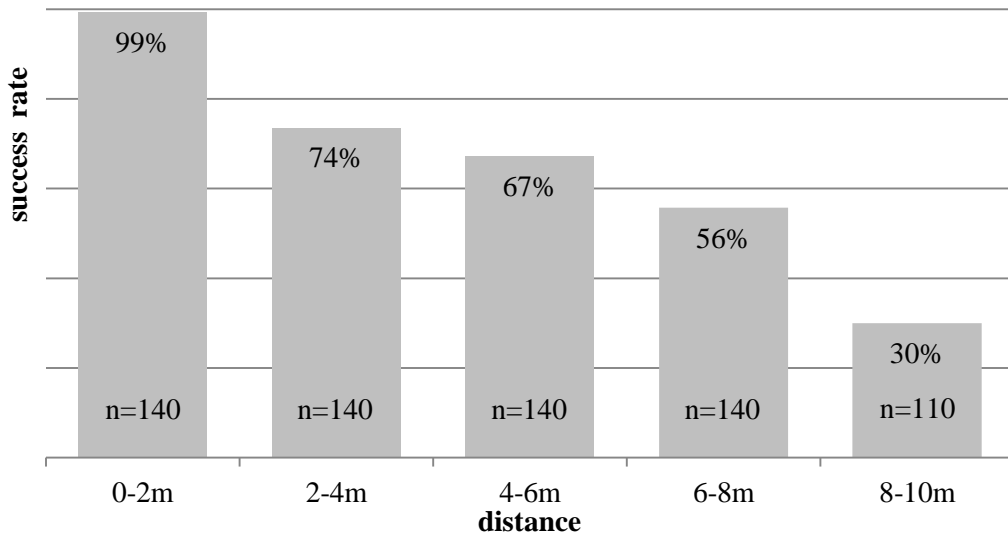
Figure 5-7: Wireless communication range in air

5.2.3 Implanted Communication Range

When used after the surgery, the sensor platform will have to transmit data from inside the body to the outside. The test setup shown in Figure 5-9 was used to determine whether the wireless link can operate through tissue mimicking solution. The solution was mixed according to a recipe that was used by Karacolak et al. [73] to simulate the electrical properties of body tissue. The two different recipes used for 2.45 GHz and 403 MHz are shown in Table 5-2. The solution temperature was 18.6 ℃ when the tests were performed.

Ingredient	MICS (403 MHz)	ISM (2.45 GHz)
Sugar (sucrose)	56.18%	53%
Salt (NaCl)	2.33%	-
Water (deionized)	41.49%	47%

Table 5-2: Recipe for tissue-mimicking solution [73]

The sensor platform antenna was placed embedded in medical grade silicon rubber (Dow Corning® 3140, Dow Corning Corp.) as shown in Figure 5-8.
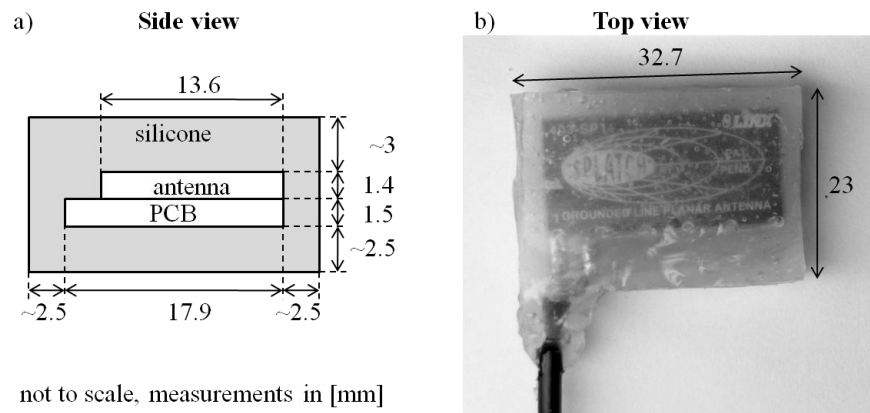
Figure 5-8: Sensor platform antenna mounted on printed circuit board (FR4) and embedded in silicone. a) side view, b) top view

The antenna was placed on a pedestal in a plastic bucket as shown in Figure 5-9 and connected to the sensor platform by a coaxial cable. The base station, mounted above the antenna, then attempted to establish a wireless communication link with the sensor platform 20 times. A successful attempt included waking up the sensor platform within 2 seconds using the 2.45 GHz wakeup signal and receiving a response on 403 MHz.
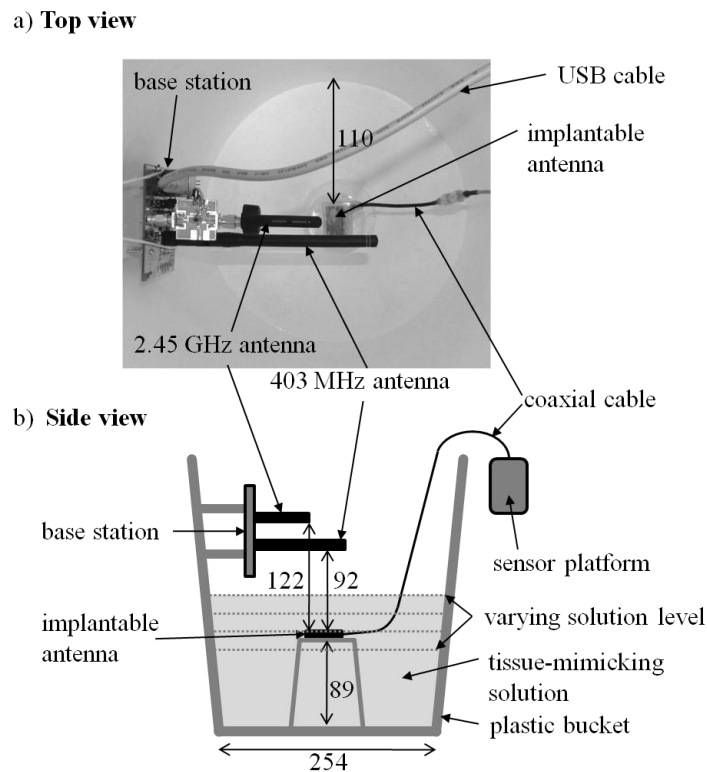
Figure 5-9: Wireless communication range in tissue-mimicking solution test setup. a) top view, b) side view. Measurements are in millimeters.

Connection attempts were made with varying 2.45 GHz transmission power levels and for different height levels of the tissue-mimicking solution. The transmission power level was in decibel (dB) relative to the maximum power. Tests were performed with transmission powers down to 56 dB below maximum. The solution heights were in millimeters (mm) above the top edge of the antenna. Tests were performed with the solution 28 mm below the antenna and up to 37 mm above the antenna. These tests were repeated for both types of tissue-mimicking solution.

Figure 5-10 shows measurements taken in the solution for 2.45 GHz at different transmission power levels. Data points right of the antenna in Figure 5-10 simulate the case where the antenna is embedded inside the human body. There, the antenna was covered by 2 to 27 mm of tissue-mimicking solution. A wireless communication link was established within 2 seconds for at least 70% of the time, even when the transmission power was reduced 15 dB below the maximum.
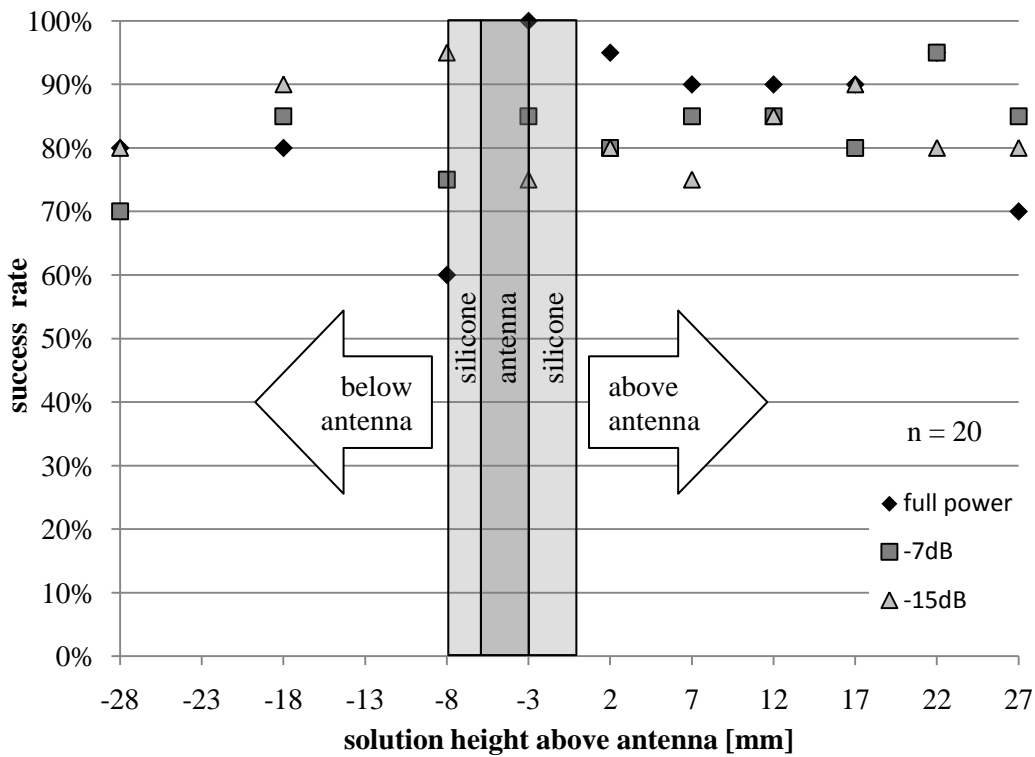
Figure 5-10: Wireless communication range at different depths in tissue-mimicking solution for 2.45 GHz. Wakeup signal transmit power set to full power, 7 dB below full power and 15 dB below full power

Figure 5-11 shows measurements taken in the solution for 403 MHz. A wireless communication link was established within 2 seconds for at least 85% of the time when the antenna was covered by 22 mm of solution. Communication was still established 40% of the time at a depth of 37 mm.
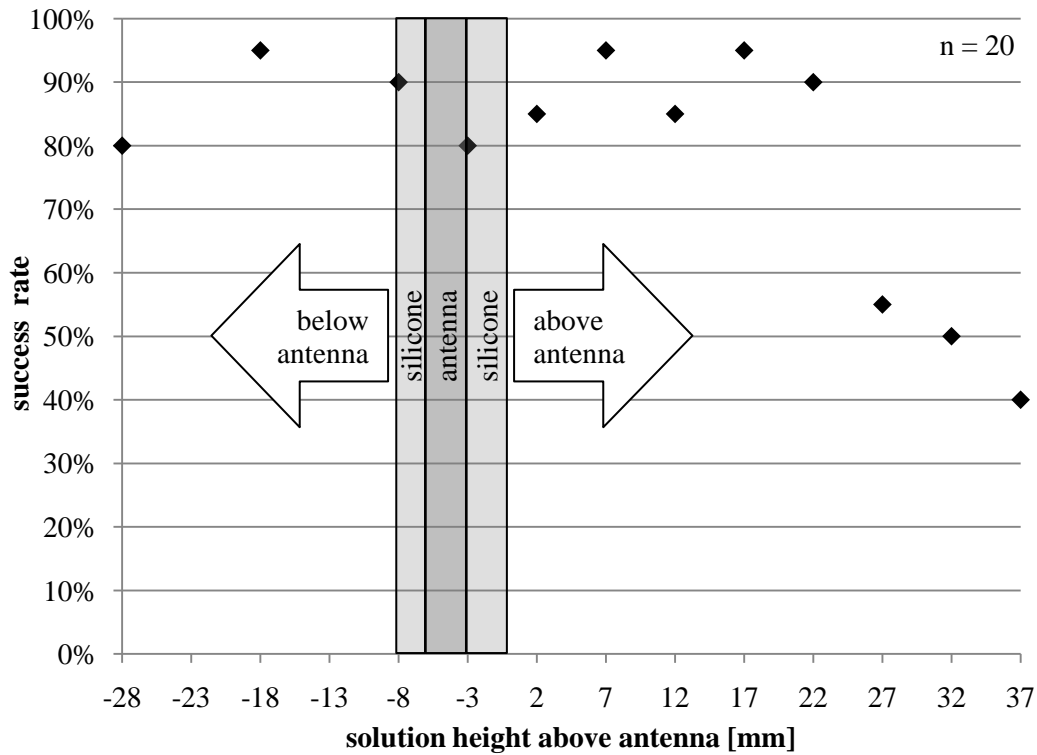
Figure 5-11: Wireless communication range at different depths in tissue-mimicking solution for 403 MHz.

The results show that wireless communication is possible with the chosen antenna when implanted inside the human body.

5.2.4 Communication Interference

The electromagnetic radiation (EMR) generated by surgical instruments and monitoring devices during the operation may interfere with the wireless communication of the sensor platform or vice versa. Figure 5-12 shows how the sensor platform was placed in the operating room and tested with several other devices running at the same time. The base station was located 2 m from the operating table.

Figure 5-12: OP setup with 1) sensor platform, 2) electrosurgical generator, 3) patient simulator, 4) navigation system, 5) anesthesia machine

The devices listed below and shown in Figure 5-12 were run simultaneously and monitored for any effects that may be caused by interference.

1) Sensor platform

2) Electrosurgical Generator, Force FX™, Valleylab, Tyco Healthcare Group LP

3) Patient simulator, MPS450, Fluke Electronics Corp.

4) Navigation System, Stealthstation® Treon™ plus, Medtronic Surgical Navigation Technologies

5) Anesthesia machine, GE Aestiva/5, Soma Technology, Inc.

The base station was able to connect to and communicate with the sensor platform at all times except when the electrosurgical generator was in use. The electrosurgical generator only prevented the base station from connecting to the sensor platform, but did not interrupt an active communication link on 403 MHz that had already been established.

Since the sensor platform system will not be used at the same time as the electrosurgical generator, this will not be a problem. No effect of the sensor platform on the functionality of other devices was observed.

5.3   Capacitive Power Module

Several charging and discharging experiments were performed to show the effect of the voltage converter on the operating time and determine the operating time under four load conditions and different charging times. The basic test setup is shown in Figure 5-13.
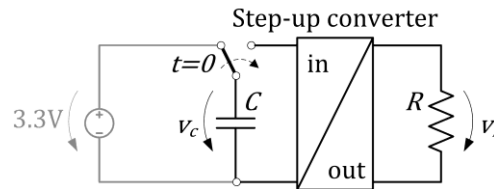
Figure 5-13: Power module test setup

The electric double-layer capacitors (EDLC) in the power module were charged by a laboratory power supply shown on the left in Figure 5-13. After a defined charging time, the power supply was disconnected from the circuit and the EDLCs were discharged by a voltage converter with a resistive load.

5.3.1   Discharge Characteristics

The EDLCs were pre-charged to their maximum rated voltage of 3.3 V using a laboratory power supply. The power supply was then disconnected and a voltage converter drained the EDLCs to provide at least 2.1 V to a load resistor. The four different load conditions simulated included 4.4 mW, 0.44 mW, 0.044 mW and 0 mW (no load). The voltages v_c across the EDLCs and v_r across the load were recorded.

Figure 5-14 compares the power module discharge voltage v_c to a standard discharge curve v_s for a capacitor with a resistive load. The power module configuration is shown in Figure 5-13 and the standard configuration in Figure 5-15a.
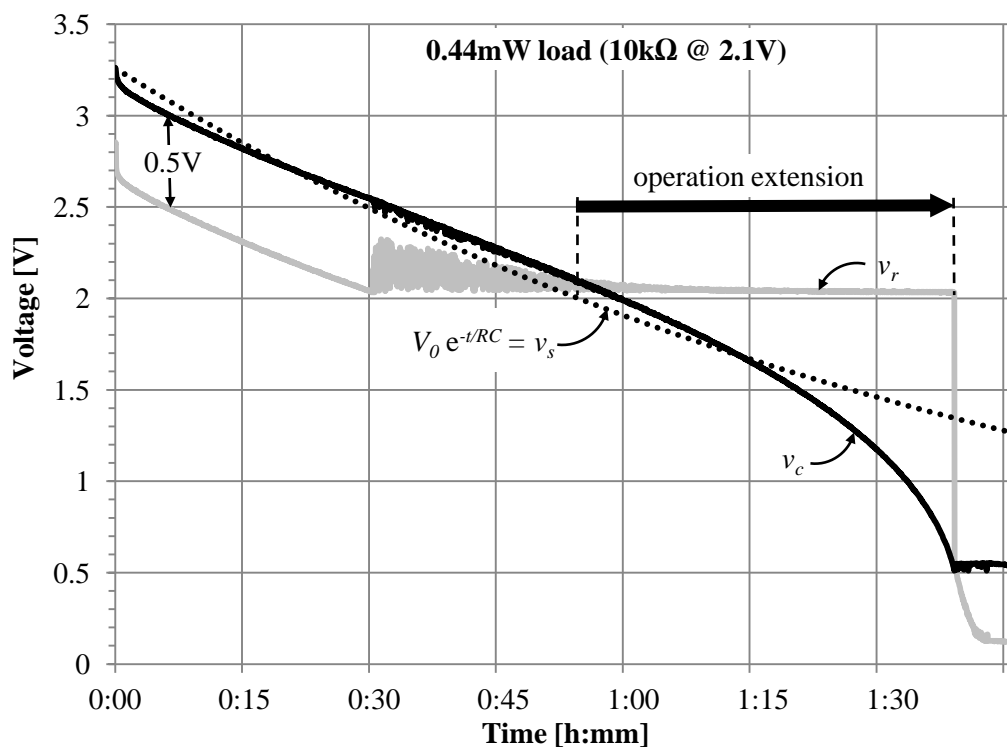
Figure 5-14: EDLC voltage v_c, converter output voltage v_r and standard discharge curve $v_s = V_0 e^{-t/RC}$.

For a 0.44 mW load with a minimum operating voltage of 2 V the usable time was extended from 55 minutes without, to 100 minutes with voltage converter. A combined step-up and step-down regulator could be used to make better use of the energy during the first 55 minutes when v_c is higher than the required output voltage and to provide a stable output voltage from the start.

In order to understand the behavior of output voltage v_r, one must first know how the selected voltage converter operated. As long as the input voltage v_c was higher than the pre-set output voltage (2.1 V), the input was internally connected to the output through a diode (Figure 5-15b). This resulted in an output voltage v_r that was about $v_d \approx 0.5V$ lower than the input voltage v_c during the first 30 minutes (Figure 5-14). When the input voltage was less than 2.6 V, the voltage converter switched to a boost mode to maintain the pre-set output voltage. When the input voltage decreased to 0.5V, the converter could no longer maintain the proper output voltage.
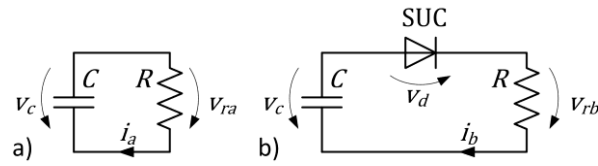
Figure 5-15: a) Standard configuration with load on capacitor, b) Load connected to capacitor through voltage converter in diode mode.

Figure 5-16 compares the EDLC discharge times for different loads. Each curve shows the EDLC voltage v_c for a particular load labeled in milliwatts (mW). The voltages decrease as the EDLCs are discharged down to 0.5 V at which the voltage converter shut down. It is noticeable that the EDLCs were being discharged even when there was no load connected. This was due to the self-discharge rate of EDLCs and the quiescent current of the voltage converter.
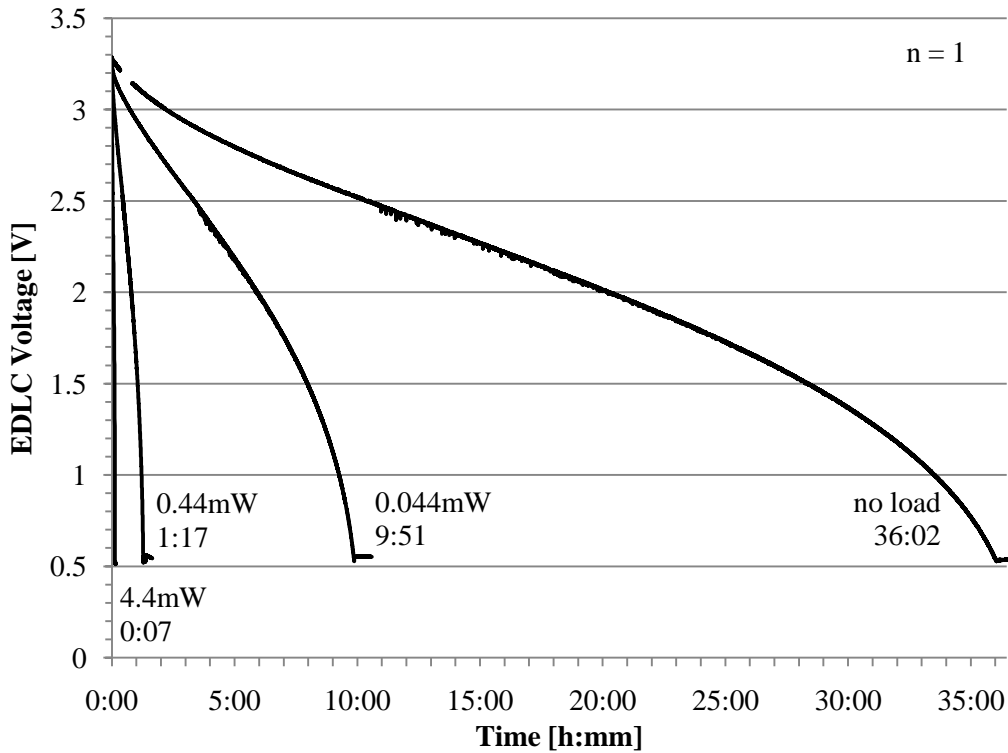
Figure 5-16: EDLC discharge voltage curves for 4.4mW, 0.44mW, 0.044mW and no load (open) with operating times noted. Charging time was 10 minutes.

The operating times from Figure 5-16 are plotted on a logarithmic scale in Figure 5-17 to show the relationship between the load and the operating time.

79
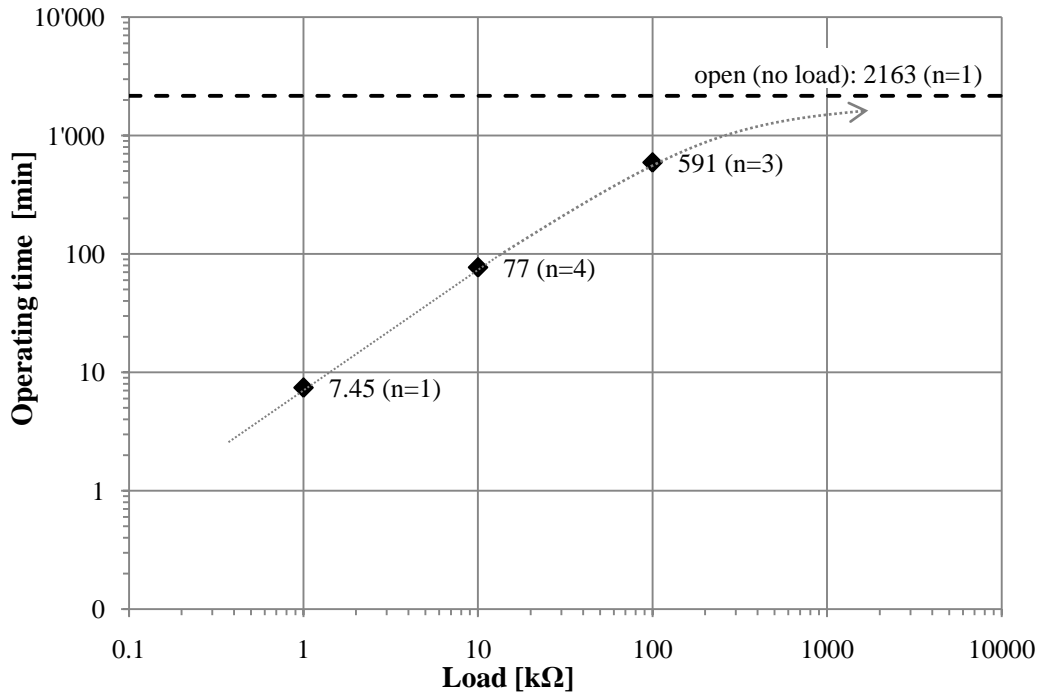
Figure 5-17: Power module operating time vs. load. Charging time was 10 minutes.

The resistance R seen by the EDLC can be modeled as the load resistance R_L in parallel with an internal resistance R_i

$$(5\text{-}1) \qquad\qquad R = \frac{1}{\frac{1}{R_i}+\frac{1}{R_L}}$$

where the load resistance R_L is shown on the horizontal axis in Figure 5-17 and R_i is a virtual internal resistance representing the self-discharge current of the EDLCs and the quiescent current of the voltage regulator. R_i will typically be in the range of several 100 kΩ. The total resistance R in equ.(5-1) is dominated by the $1/R_L$ term as long as $R_L<<R_i$, and R will go towards R_i as R_L approaches infinity (no load). Therefore, the operating time cannot exceed the dashed line in Figure 5-17 that marks the operating time with no load connected ($1/R_L = 0$).

5.3.2 Charging Characteristics

The amount of electrical charge stored in an EDLC depends on the charging voltage, the charging current, the charging time and the ESR. The charging voltage was limited to the 3.3 V rating of the EDLCs. The maximum charging current i_0 for three EDLCs

connected in parallel was given by equation (4-28) and computed for an ESR of 200 Ω and a rated voltage of 3.3 V in equation (5-2) as

(5-2)
$$i_0 = \frac{3.3V}{200\Omega/3} = \underline{49.5mA}$$

The three EDLCs in the charging module were charged by a laboratory power supply at their rated voltage of 3.3 V (Figure 5-13). The current limit of the power supply was set at 1.3 A, well above the maximum charging current given by equation (5-2). The charging time was varied in order to determine the relationship between charging time and operating time.

Figure 5-18 shows the EDLC voltage discharge curves for different charging times. There is only a small initial drop in the voltage at $t = 0$ for a charging time of 90 minutes, indicating that the EDLCs are fully charged. The initial voltage drop is about 1.2 V after a charging time of 1 minute.
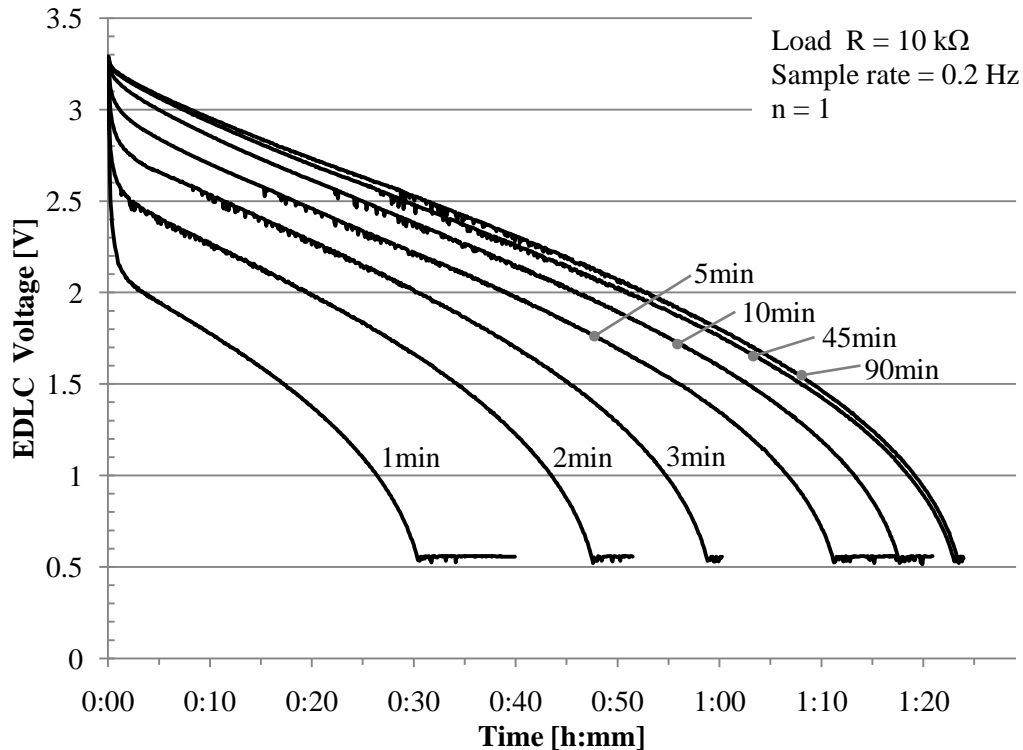
Figure 5-18: EDLC voltage discharge curves for 1 min, 2 min, 3 min, 5 min, 10 min, 45 min and 90 min charging times

The operating time is shown as a function of the charging time in Figure 5-19 and listed in Table 5-3. The operating time increases rapidly at the beginning, but there is little gain

for long charging time as the EDLC's are saturated. Table 5-3 lists the operating time relative to when it is approximately fully charged at 90 minutes charging time.
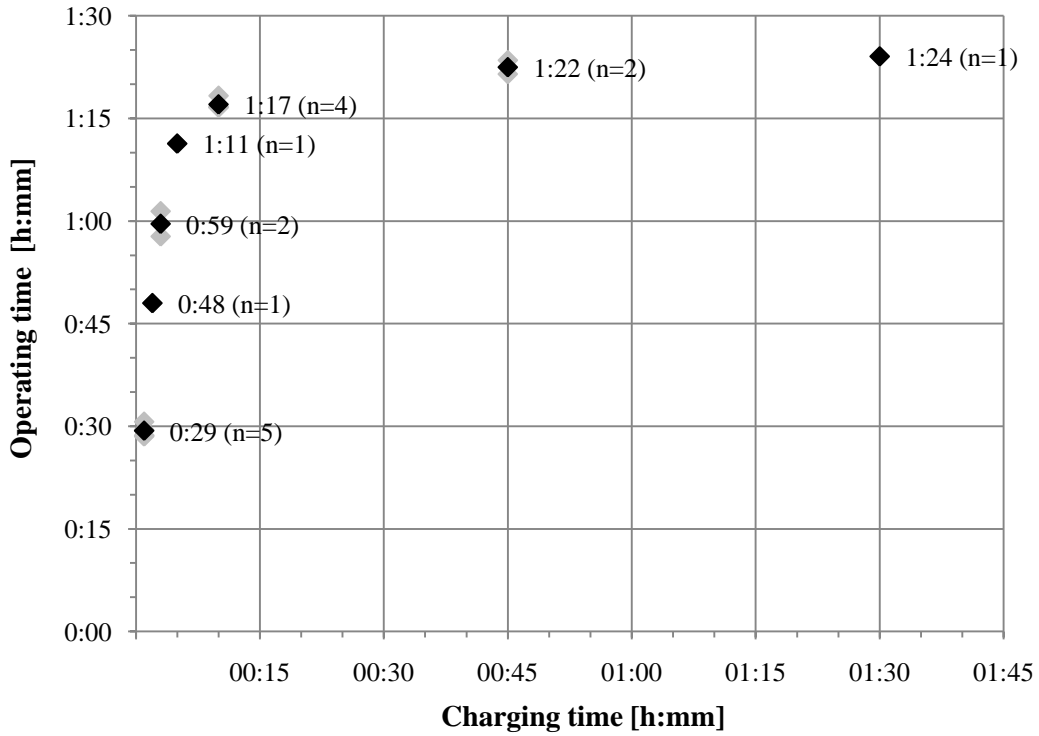
Figure 5-19: Operating time vs. charging time (1 min, 2 min, 3 min, 5 min, 10 min, 45 min, 90 min) for 10 kΩ load

Charging time	Operating time	
[minutes]	[minutes]	
90	84	100.0%
45	82	97.6%
10	77	91.7%
5	71	84.5%
3	59	70.2%
2	48	57.1%
1	29	34.5%

Table 5-3: Operating time vs. charging time for 10 kΩ load

Chapter 6

Conclusion and Recommendations

6.1 Conclusions

There is no system available to measure both the forces during scoliosis surgery and monitor residual forces after the surgery. This thesis describes a wireless implantable load monitoring system consisting of an implantable sensor platform and a base station. Wireless data transfer and magnetic power transfer were found to be suited for this application. Capacitive power storage was investigated for medium term implantable power storage. A prototype system was designed to validate the sensor interface, the wireless communication link and the capacitive power storage. The sensor platform was able to measure 32 signals produced by the MEMS-transducers on one hook or screw head with a resolution of 1.46 mV. The internal temperature sensor allowed for temperature compensation of measurements. The power consumption of the implanted sensor platform was 11.05 mW when sampling at 10 Hz and 0.36 mW when in sleep mode. The wireless communication range was 99% reliable up to 2 m in free air which is sufficient for use in the operating room. The reliability of the wireless communication link needs to be improved for implanted operation. The designed capacitive power module has the potential to become a medium term power storage for implantable devices. The capacitive power module with a total capacitance of 660 mF was able to provide a minimum of 2.1 V to a 0.44 mW load for 77 minutes when previously charged for 10 minutes. This prototype system will be further developed and miniaturized. The basic concepts can be used for any implantable wireless telemetry system and are not limited to applications for the treatment of scoliosis.

6.2 Recommendations and Future Work

Some work is still required before the system can be used in a patient. *Biocompatible packaging* needs to be developed for the implantable sensor platform. This is an

important aspect of an implantable device as the packaging must protect the sensitive circuitry from the hostile body environment as well as prevent adverse effects on the surrounding tissue. Body fluids are corrosive and electrically conductive and thus have the potential of destroying sensitive electric components or short circuit them. Feed-throughs for sensors are usually the weak point of the packaging and require special attention. Electromagnetic properties of the material have to be considered if inductive power supply and wireless data transmission are used. A magnetically conductive material will divert energy around an enclosed receiving coil and get heated in the process while an implant encased in an electrically conductive material will create a Faraday cage and thus require an external antenna.

The wireless transmission power needs to be measured to ensure it meets the FCC specifications. The reliability of the wireless communication link should be verified in cadaveric tests.

An inductive *transcutaneous power transfer* circuit has to be built and optimized for this application in order to allow use of the system after surgery.

The hardware and software of the systems can be enhanced to reduce the size, improve the operating time, increase the wireless communication range and increase the reliability and flexibility of the system.

The size of the sensor platform can be reduced by

- using multilayer printed circuit boards and/or flexible printed circuit boards.

- use wire bonding to die of microcontroller and wireless transceiver instead of surface mount packages.

- integrate microcontroller and transceiver circuit into a custom ASIC.

- minimize antenna matching network by utilizing tuning capacitors integrated into the transceiver IC.

The operating time can be increased by optimizing the sensor platform embedded software to reduce the power consumption. The wireless transceiver should be turned off most of the time and only turned on for a short time to transmit data bursts to the base

station. This will require a sophisticated communication protocol that is able to function in a half-duplex wireless link.

The wireless communication link needs to be optimized to increase the range when the sensor platform is implanted inside the body. The chip-antenna currently used is optimized for operation in free air and is not efficient when embedded in tissue. An antenna optimized for implantable devices can be developed using methods described by Karacolak et al. [73].

The software can be modified in order to increase the reliability and flexibility of the system.

- The sensor platform configuration is currently stored in volatile RAM. This configuration could be stored in the info section of the flash memory inside the MSP430F2132 microcontroller.

- The windows software periodically sends status request commands to the base station in order to keep track of the hardware status. This status polling takes up valuable bandwidth in the USB connection and introduces delays in status updates to the windows software. An update command should be implemented that allows the base station to notify the windows software of status changes.

The ZL70101 wireless transceiver on the sensor platform can be remotely controlled without intervention of the microcontroller. If the reset input of the microcontroller is connected to a digital output pin of the ZL70101, the implanted system can be restarted by means of a soft-reset in case of a software failure. It should also be possible to remotely program the sensor platform microcontroller through the wireless link while it is implanted inside the body.

Bibliography

[1] M. A. Asher and D. C. Burton, "Adolescent idiopathic scoliosis: natural history and long term treatment effects," *Scoliosis,* vol. 1, pp. 2-10, MAR, 2006.

[2] K. Pehrsson, S. Larsson, A. Oden and A. Nachemson, "Long-Term Follow-Up of Patients with Untreated Scoliosis - a Study of Mortality, Causes of Death, and Symptoms," *Spine,* vol. 17, pp. 1091-1096, SEP, 1992.

[3] www.srs.org. Types of scoliosis. *2009(04/26), .*

[4] N. H. Miller, "Cause and natural history of adolescent idiopathic scoliosis," *Orthop. Clin. North Am.,* vol. 30, pp. 343-352, JUL, 1999.

[5] P. R. Harrington, "Treatment of Scoliosis - Correction and Internal Fixation by Spine Instrumentation," *Journal of Bone and Joint Surgery-American Volume,* vol. 44, pp. 591-634, 1962.

[6] Y. Cotrel, J. Dubousset and M. Guillaumat, "New Universal Instrumentation in Spinal Surgery," *Clin. Orthop.,* vol. 227, pp. 10-23, FEB, 1988.

[7] J. M. Hicks, A. Singla, F. H. Shen and V. Arlet, "Complications of Pedicle Screw Fixation in Scoliosis Surgery A Systematic Review," *Spine,* vol. 35, pp. E465-E470, MAY 15, 2010.

[8] J. M. Flynn, R. R. Betz, M. F. O'Brien, P. O. Newton and Harms Study Grp, "Radiographic Classification of Complications of Instrumentation in Adolescent Idiopathic Scoliosis," *Clin. Orthop.,* vol. 468, pp. 665-669, MAR, 2010.

[9] A. B. Schultz and C. Hirsch, "Mechanical Analysis of Harrington Rod Correction of Idiopathic Scoliosis," *Journal of Bone and Joint Surgery-American Volume,* vol. A 55, pp. 983-992, 1973.

[10] V. K. Goel and L. G. Gilbertson, "Spine Update: Applications of the Finite Element Method to Thoracolumbar Spinal Research-Past, Present, and Future," *Spine,* vol. 20, pp. 1719-1727, August, 1995.

[11] C. E. Aubin, Y. Petit, I. A. F. Stokes, F. Poulin, M. Gardner-Morse and H. Labelle, "Biomechanical modeling of posterior instrumentation of the scoliotic spine," *Comput Methods Biomech Biomed Engin,* vol. 6, pp. 27-32, 2003.

[12] Y. Majdouline, C. Aubin, A. Sangole and H. Labelle, "Computer simulation for the optimization of instrumentation strategies in adolescent idiopathic scoliosis," *Med. Biol. Eng. Comput.,* vol. 47, pp. 1143-1154, NOV, 2009.

[13] C. Hirsch and T. Waugh, "The Introduction of Force Measurements Guiding Instrumental Correction of Scoliosis," *Acta Orthopaedica,* vol. 39, pp. 136-144, 1968.

[14] A. Nachemson and G. Elfstrom, "Intravital Wireless Telemetry of Axial Forces in Harrington Distraction Rods in Patients with Idiopathic Scoliosis," *Journal of Bone and Joint Surgery-American Volume,* vol. A 53, pp. 445-465, 1971.

[15] G. Elfstrom and A. Nachemson, "Telemetry Recordings of Forces in Harrington Distraction Rod - Method for Increasing Safety in Operative Treatment of Scoliosis Patients," *Clin. Orthop.,* pp. 158-172, 1973.

[16] H. K. Dunn, A. U. Daniels and G. G. McBride, "Intraoperative Force Measurements During Correction of Scoliosis," *Spine,* vol. 7, pp. 448-455, SEP/OCT, 1982.

[17] A. Rohlmann, G. Bergmann and F. Graichen, "A Spinal Fixation Device for In-Vivo Load Measurement," *J. Biomech.,* vol. 27, pp. 961-963, JUL, 1994.

[18] F. Graichen, G. Bergmann and A. Rohlmann, "Telemetry System for In-Vivo Measurement of the Loading of an Internal Spinal Fixation Device," *Biomed. Tech.,* vol. 39, pp. 251-258, OCT, 1994.

[19] A. Rohlmann, L. H. Riley, G. Bergmann and F. Graichen, "In vitro load measurement using an instrumented spinal fixation device," *Med. Eng. Phys.,* vol. 18, pp. 485-488, SEP, 1996.

[20] I. B. Ghanem, F. Hagnere, J. F. Dubousset, B. Watier, W. Skalli and F. Lavaste, "Intraoperative optoelectronic analysis of three-dimensional vertebral displacement after Cotrel-Dubousset rod rotation - A preliminary report," *Spine,* vol. 22, pp. 1913-1921, AUG 15, 1997.

[21] E. Lou, D. L. Hill, J. V. Raso, M. J. Moreau and J. K. Mahood, "Instrumented rod rotator system for spinal surgery," *Med. Biol. Eng. Comput.,* vol. 40, pp. 376-379, JUL, 2002.

[22] E. Lou, V. J. Raso, B. Martin, E. Epper and D. L. Hill, "A wireless load measurement tool for spine surgery," in Ottawa, Ont., 2005, pp. 1813-1817.

[23] E. Lou, V. J. Raso, B. Martin, D. Schile, M. Epper, J. K. Mahood, M. Moreau and D. Hill, "Wireless Surgical Tools for Mechanical Measurements during Scoliosis Surgery," *Conf. Proc. IEEE Eng. Med. Biol. Soc.,* vol. 7, pp. 7131-7134, 2005.

[24] J. R. Cobb, "The problem of the primary curve," *J. Bone Joint Surg. Am.,* vol. 42-A, pp. 1413-1425, Dec, 1960.

[25] S. Berven and D. S. Bradford, "Neuromuscular scoliosis: Causes of deformity and principles for evaluation and management," *Semin. Neurol.,* vol. 22, pp. 167-178, JUN, 2002.

[26] S. Allen, E. Parent, M. Khorasani, D. L. Hill, E. Lou and J. V. Raso, "Validity and reliability of active shape models for the estimation of Cobb angle in patients with adolescent idiopathic scoliosis," *J. Digital Imaging,* vol. 21, pp. 208-218, JUN, 2008.

[27] J. E. Lonstein, "Adolescent Idiopathic Scoliosis," *Lancet,* vol. 344, pp. 1407-1412, NOV 19, 1994.

[28] K. M. C. Cheung, T. Wang, G. X. Qiu and K. D. K. Luk, "Recent advances in the aetiology of adolescent idiopathic scoliosis," *Int. Orthop.,* vol. 32, pp. 729-734, DEC, 2008.

[29] H. Halm, A. Richter, B. Thomsen, M. Koeszegvary, M. Ahrens and M. Quante, "Anterior scoliosis surgery. State of the art and a comparison with posterior techniques," *Orthopade,* vol. 38, pp. 131-145, FEB, 2009.

[30] S. Kadoury, F. Cheriet, M. Beausejour, I. A. Stokes, S. Parent and H. Labelle, "A three-dimensional retrospective analysis of the evolution of spinal instrumentation for the correction of adolescent idiopathic scoliosis," *European Spine Journal,* vol. 18, pp. 23-37, JAN, 2009.

[31] V. Reddi, D. V. Clarke and V. Arlet, "Anterior thoracoscopic instrumentation in adolescent idiopathic scoliosis - A systematic review," *Spine,* vol. 33, pp. 1986-1994, AUG 15, 2008.

[32] P. O. Newton, V. V. Upasani, J. Lhamby, V. L. Ugrinow, J. B. Pawelek and T. P. Bastrom, "Surgical Treatment of Main Thoracic Scoliosis with Thoracoscopic Anterior Instrumentation Surgical Technique," *Journal of Bone and Joint Surgery-American Volume,* vol. 91A, pp. 233-248, OCT, 2009.

[33] J. Beastall, E. Karadimas, M. Siddiqui, M. Nicol, J. Hughes, F. Smith and D. Wardlaw, "The Dynesys lumbar spinal stabilization system - A preliminary report on positional magnetic resonance imaging findings," *Spine,* vol. 32, pp. 685-690, MAR 15, 2007.

[34] S. M. Lee, S. I. Suk and E. R. Chung, "Direct vertebral rotation: A new technique of three-dimensional deformity correction with segmental pedicle screw fixation in adolescent idiopathic scoliosis," *Spine,* vol. 29, pp. 343-349, FEB 1, 2004.

[35] C. E. Aubin, V. Goussev and Y. Petit, "Biomechanical modelling of segmental instrumentation for surgical correction of 3D spinal deformities using Euler-Bernoulli thin-beam elastic deformation equations," *Med. Biol. Eng. Comput.,* vol. 42, pp. 216-221, MAR, 2004.

[36] C. E. Aubin, H. Labelle, C. Chevrefils, G. Desroches, J. Clin and A. Boivin, "Preoperative planning simulator for spinal deformity surgeries," *Spine,* vol. 33, pp. 2143-2152, SEP 15, 2008.

[37] J. D. Coe, V. Arlet, W. Donaldson, S. Berven, D. S. Hanson, R. Mudiyam, J. H. Perra and C. I. Shaffrey, "Complications in spinal fusion for adolescent idiopathic scoliosis in the new millennium. A report of the Scoliosis Research Society Morbidity and Mortality Committee," *Spine,* vol. 31, pp. 345-349, FEB 1, 2006.

[38] A. S. Little, L. B. C. Brasiliense, B. C. R. Lazaro, P. M. Reyes, C. A. Dickman and N. R. Crawford, "Biomechanical Comparison of Costotransverse Process Screw Fixation and Pedicle Screw Fixation of the Upper Thoracic Spine," *Neurosurgery,* vol. 66, pp. 178-182, MAR, 2010.

[39] M. J. McGirt, E. G. Sutter, R. Xu, D. M. Sciubba, J. Wolinsky, T. F. Witham, Z. L. Gokaslan and A. Bydon, "Biomechanical Comparison of Translaminar Versus Pedicle Screws at T1 and T2 in Long Subaxial Cervical Constructs," *Neurosurgery,* vol. 65, pp. 167-172, DEC, 2009.

[40] A. T. Mahar, R. Bagheri, R. Oka, P. Kostial and B. A. Akbarnia, "Biomechanical comparison of different anchors (foundations) for the pediatric dual growing rod technique," *Spine Journal,* vol. 8, pp. 933-939, NOV-DEC, 2008.

[41] K. Seller, D. Wahl, A. Wild, R. Krauspe, E. Schneider and B. Linke, "Pullout strength of anterior spinal instrumentation: a product comparison of seven screws in calf vertebral bodies," *European Spine Journal,* vol. 16, pp. 1047-1054, JUL, 2007.

[42] K. Z. Yuksel, M. S. Adams, R. H. Chamberlain, M. Potocnjak, S. C. Park, V. K. H. Sonntag and N. R. Crawford, "Pullout resistance of thoracic extrapedicular screws used as a salvage procedure," *Spine Journal,* vol. 7, pp. 286-291, MAY-JUN, 2007.

[43] A. Alobaid, V. Arlet, A. Busato and T. Steffen, "Pull-out strength of the suprapedicle claw construct: a biomechanical study," *European Spine Journal,* vol. 14, pp. 759-764, OCT, 2005.

[44] L. Balabaud, E. Gallard, W. Skalli, B. Dupas, R. Roger, F. Lavaste and J. P. Steib, "Biomechanical evaluation of a bipedicular spinal fixation device: three different strength tests," *European Spine Journal,* vol. 12, pp. 480-486, OCT, 2003.

[45] L. E. Gayet, P. Pries, H. Hamcha, J. P. Clarac and J. Texereau, "Biomechanical study and digital modeling of traction resistance in posterior thoracic implants," *Spine,* vol. 27, pp. 707-714, APR 1, 2002.

[46] J. G. Heller, J. K. Shuster and W. C. Hutton, "Pedicle and transverse process screws of the upper thoracic spine - Biomechanical comparison of loads to failure," *Spine,* vol. 24, pp. 654-658, APR 1, 1999.

[47] L. S. Freedman, G. R. Houghton and M. Evans, "Cadaveric Study Comparing the Stability of Upper Distraction Hooks used in Harrington Instrumentation," *Spine,* vol. 11, pp. 579-582, 1986.

[48] A. Rohlmann, F. Graichen, R. Kayser, A. Bender and G. Bergmann, "Loads on a telemeterized vertebral body replacement measured in two patients," *Spine,* vol. 33, pp. 1170-1179, MAY 15, 2008.

[49] A. Rohlmann, F. Graichen, U. Weber and G. Bergmann, "2000 Volvo Award Winner in Biomechanical Studies - Monitoring in vivo implant loads with a telemeterized internal spinal fixation device," *Spine,* vol. 25, pp. 2981-2986, DEC 1, 2000.

[50] X. Wang, C. Aubin, H. Labelle and D. Crandall, "Biomechanical Modelling of a Direct Vertebral Translation Instrumentation System: Preliminary Results," *Research into Spinal Deformities 6,* vol. 140, pp. 128-132, 2008.

[51] R. Dumas, V. Lafage, Y. Lafon, J. Steib, D. Mitton and W. Skalli, "Finite element simulation of spinal deformities correction by *in situ* contouring technique," *Computer Methods in Biomechanics and Biomedical Engineering,* vol. 8, pp. 331-337, 2005.

[52] F. Cheriet, S. Delorme, J. Dansereau, C. E. Aubin, J. A. De Guise and H. Labelle, "Intraoperative 3D reconstruction of the scoliotic spine from radiographs," *Ann. Chir.,* vol. 53, pp. 808-+, 1999.

[53] J. M. Mac-Thiong, C. E. Aubin, J. Dansereau, J. A. de Guise, P. Brodeur and H. Labelle, "Registration and geometric modelling of the spine during scoliosis surgery: a comparison study of different preoperative reconstruction techniques and intra-operative tracking systems," *Med. Biol. Eng. Comput.,* vol. 37, pp. 445-450, JUL, 1999.

[54] I. A. F. Stokes, M. Gardner-Morse, C. E. Aubin, F. Poulin and H. Labelle, "Biomechanical simulations for planning of scoliosis surgery," *Research into Spinal Deformities 2,* vol. 59, pp. 343-346, 1999.

[55] I. A. F. Stokes and M. Gardnermorse, "3-Dimensional Simulation of Harrington Distraction Instrumentation for Surgical-Correction of Scoliosis," *Spine,* vol. 18, pp. 2457-2464, DEC, 1993.

[56] D. Benfield, E. Lou and W. Moussa, "Development of a MEMS-based sensor array to characterise in situ loads during scoliosis correction surgery," *Comput. Methods Biomech. Biomed. Engin.,* vol. 11, pp. 335-350, AUG, 2008.

[57] T. J. Koh and T. R. Leonard, "An implantable electrical interface for in vivo studies of the neuromuscular system," *J. Neurosci. Methods,* vol. 70, pp. 27-32, DEC, 1996.

[58] M. S. Wegmueller, S. Huclova, J. Froehlich, M. Oberle, N. Felber, N. Kuster and W. Fichtner, "Galvanic Coupling Enabling Wireless Implant Communications," *Instrumentation and Measurement, IEEE Transactions on,* vol. 58, pp. 2618-2625, 2009.

[59] D. P. Lindsey, E. L. McKee, M. L. Hull and S. M. Howell, "A new technique for transmission of signals from implantable transducers," *Biomedical Engineering, IEEE Transactions on,* vol. 45, pp. 614-619, 1998.

[60] S. Ozeri and D. Shmilovitz, "Ultrasonic transcutaneous energy transfer for powering implanted devices," *Ultrasonics,* vol. 50, pp. 556-566, MAY, 2010.

[61] C. Algora and R. Pena, "Recharging the Battery of Implantable Biomedical Devices by Light," *Artif. Organs,* vol. 33, pp. 855-860, OCT, 2009.

[62] T. Mussivand, K. S. Holmes, A. Hum and W. J. Keon, "Transcutaneous Energy Transfer with Voltage Regulation for Rotary Blood Pumps," *Artif. Organs,* vol. 20, pp. 621-624, 1996.

[63] A. Djemouai and M. Sawan, "Circuit techniques for effective wireless transfer of power and data to electronic implants," *J. Circuits Syst. Comput.,* vol. 16, pp. 801-818, OCT, 2007.

[64] A. M. Sodagar, K. D. Wise and K. Najafi, "A Wireless Implantable Microsystem for Multichannel Neural Recording," *IEEE Trans. Microwave Theory Tech.,* vol. 57, pp. 2565-2573, OCT, 2009.

[65] M. Sawan, S. Hashemi, M. Sehil, F. Awwad, M. Hajj-Hassan and A. Khouas, "Multicoils-based inductive links dedicated to power up implantable medical devices: modeling, design and experimental results," *Biomed. Microdevices,* vol. 11, pp. 1059-1070, OCT, 2009.

[66] K. VanSchuylenbergh and R. Puers, "Self-tuning inductive powering for implantable telemetric monitoring systems," *Sensors and Actuators A-Physical,* vol. 52, pp. 1-7, MAR-APR, 1996.

[67] S. Choi and M. Lee, "Coil-Capacitor Circuit Design of a Transcutaneous Energy Transmission System to Deliver Stable Electric Power," *ETRI J.,* vol. 30, pp. 844-849, DEC, 2008.

[68] J. A. Miller, G. Belanger and T. Mussivand, "Development of an Autotuned Transcutaneous Energy Transfer System," *ASAIO Journal,* vol. 39, pp. M706-M710, July/September, 1993.

[69] T. D. Dissanayake, D. M. Budgett, P. Hu, L. Bennet, S. Pyner, L. Booth, S. Amirapu, Y. Wu and S. C. Malpas, "A Novel Low Temperature Transcutaneous Energy Transfer System Suitable for High Power Implantable Medical Devices: Performance and Validation in Sheep," *Artif. Organs,* vol. 34, pp. E160-E167, 2010.

[70] L. S. Theogarajan, "A Low-Power Fully Implantable 15-Channel Retinal Stimulator Chip," *IEEE J Solid State Circuits,* vol. 43, pp. 2322-2337, OCT, 2008.

[71] T. B. Tang, S. Smith, B. W. Flynn, J. T. M. Stevenson, A. M. Gundlach, H. M. Reekie, A. F. Murray, D. Renshaw, B. Dhillon, A. Ohtori, Y. Inoue, J. G. Terry and A. J. Walton, "Implementation of wireless power transfer and communications for an implantable ocular drug delivery system," *IET Nanobiotechnol.,* vol. 2, pp. 72-79, SEP, 2008.

[72] J. Riistama, J. Vaeisaenen, S. Heinisuo, H. Harjunpaeae, S. Arra, K. Kokko, M. Maentylae, J. Kaihilahti, P. Heino, M. Kellomaeki, O. Vainio, J. Vanhala, J. Lekkala and J. Hyttinen, "Wireless and inductively powered implant for measuring electrocardiogram," *Med. Biol. Eng. Comput.,* vol. 45, pp. 1163-1174, DEC, 2007.

[73] T. Karacolak, A. Z. Hood and E. Topsakal, "Design of a Dual-Band Implantable Antenna and Development of Skin Mimicking Gels for Continuous Glucose Monitoring," *Microwave Theories & Techniques,* vol. 56, pp. 1001-1008, 2008.

[74] T. Houzen, M. Takahashi, K. Saito and K. Ito, "Implanted planar inverted F-antenna for cardiac pacemaker system," in *IWAT2008,* Chiba, Japan, 2008, pp. 346-349.

[75] H. T. Friis, "A Note on a Simple Transmission Formula," *Proceedings of the IRE,* vol. 34, pp. 254-256, 1946.

[76] S. Gabriel, R. W. Lau and C. Gabriel, "The dielectric properties of biological tissues .2. Measurements in the frequency range 10 Hz to 20 GHz," *Phys. Med. Biol.,* vol. 41, pp. 2251-2269, NOV, 1996.

[77] S. Kerzenmacher, J. Ducree, R. Zengerle and F. von Stetten, "Energy harvesting by implantable abiotically catalyzed glucose fuel cells," *J. Power Sources,* vol. 182, pp. 1-17, JUL 15, 2008.

[78] H. Chen, M. Liu, C. Jia and Z. Wang, "Power Harvesting Using PZT Ceramics Embedded in Orthopedic Implants," *IEEE Trans. Ultrason. Ferroelectr. Freq. Control,* vol. 56, pp. 2010-2014, SEP, 2009.

[79] B. E. Lewandowski, K. L. Kilgore and K. J. Gustafson, "In Vivo Demonstration of a Self-Sustaining, Implantable, Stimulated-Muscle-Powered Piezoelectric Generator Prototype," *Ann. Biomed. Eng.,* vol. 37, pp. 2390-2401, NOV, 2009.

[80] J. C. Norman, V. H. Covelli, W. F. Bernhard and J. Spira, "An Implantable Nuclear Fuel Capsule for an Artificial Heart," *Transactions American Society for Artificial Internal Organs,* vol. 14, pp. 204-&, 1968.

[81] E. Okamoto, K. Watanabe, K. Hashiba, T. Inoue, E. Iwazawa, M. Momoi, T. Hashimoto and Y. Mitamura, "Optimum selection of an implantable secondary battery for an artificial heart by examination of the cycle life test," *ASAIO J.,* vol. 48, pp. 495-502, SEP-OCT, 2002.

[82] E. Okamoto, T. Inoue, K. Watanabe, T. Hashimoto, E. Iwazawa, Y. Abe, T. Chinzei, T. Isoyama, S. Kobayashi, I. Saito, F. Sato, H. Matsuki, K. Imachi and Y. Mitamura, "Development of an implantable high-energy and compact battery system for artificial heart," *Artif. Organs,* vol. 27, pp. 184-188, FEB, 2003.

[83] F. Albano, Y. S. Lin, D. Blaauw, D. M. Sylvester, K. D. Wise and A. M. Sastry, "A fully integrated microbattery for an implantable microelectromechanical system," *J. Power Sources,* vol. 185, pp. 1524-1532, DEC 1, 2008.

[84] D. Benfield, W. Moussa and E. Lou, "A high-load stress sensor for scoliosis surgery application," in 2004, .

[85] R. E. Beaty, R. C. Jaeger, J. C. Suhling, R. W. Johnson and R. D. Butler, "Evaluation of Piezoresistive Coefficient Variation in Silicon Stress Sensors using a 4-

Point Bending Test Fixture," *Ieee Transactions on Components Hybrids and Manufacturing Technology,* vol. 15, pp. 904-914, OCT, 1992.

[86] O. Slattery, D. O'Mahoney, E. Sheehan and F. Waldron, "Sources of variation in piezoresistive stress sensor measurements," in *Ieee Transactions on Components and Packaging Technologies,* 2004, pp. 81-86.

Appendix A
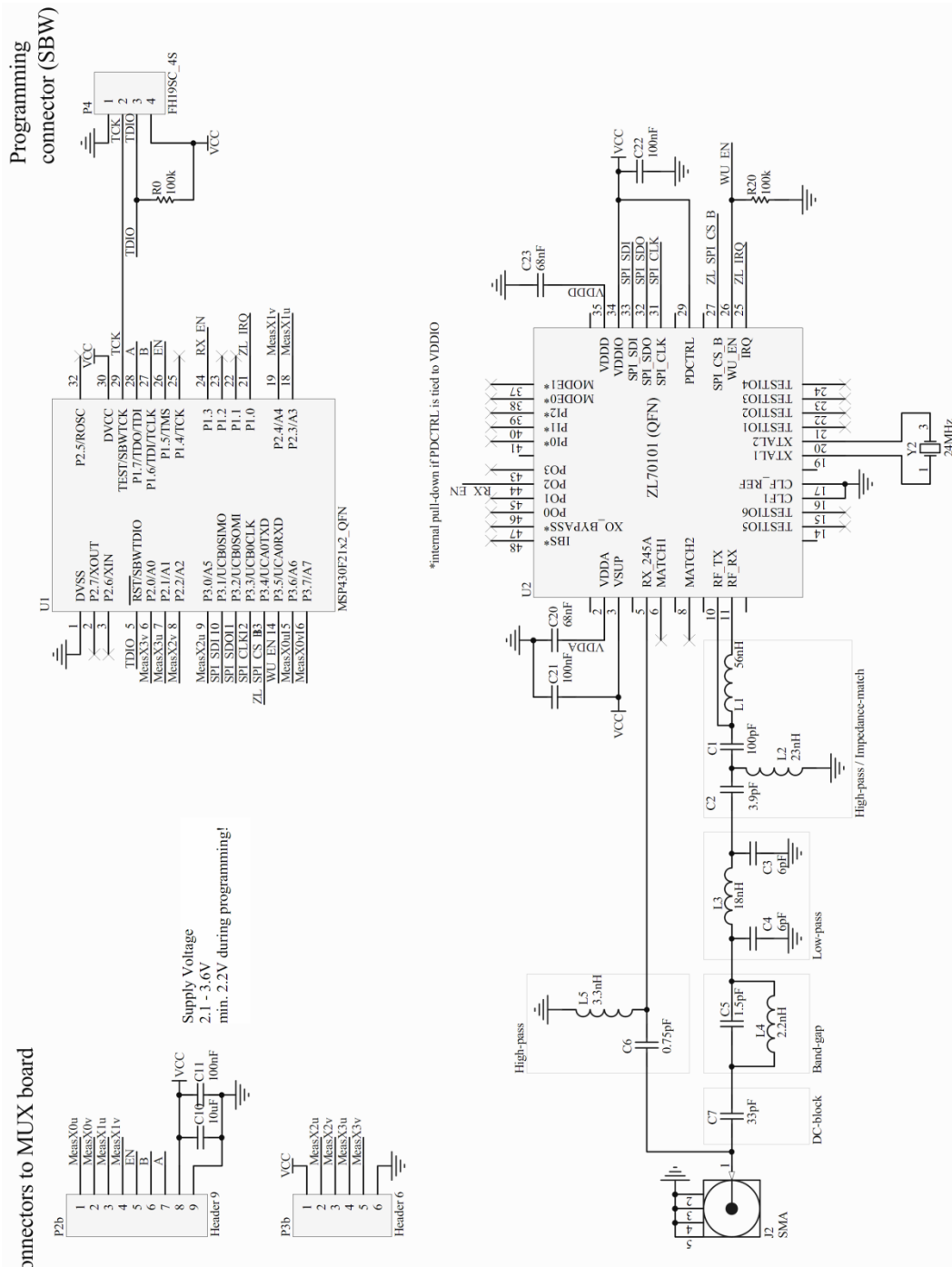
Appendix A-1: Sensor platform schematic
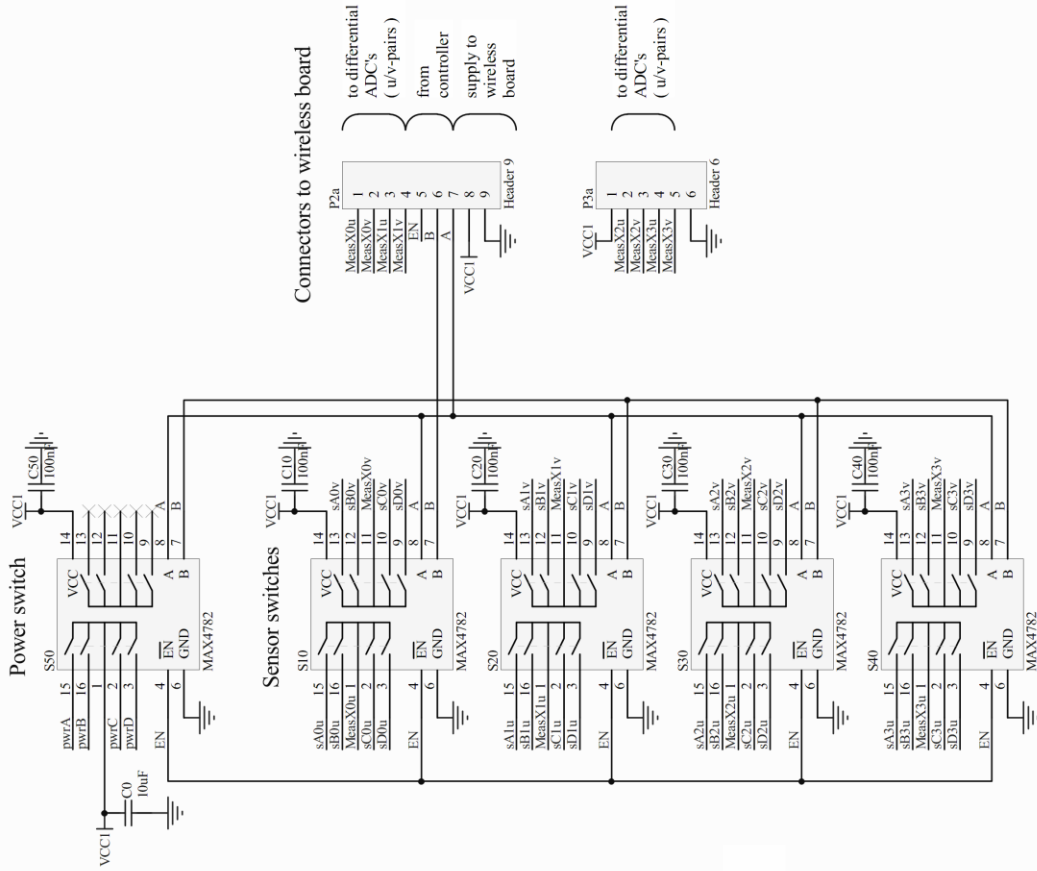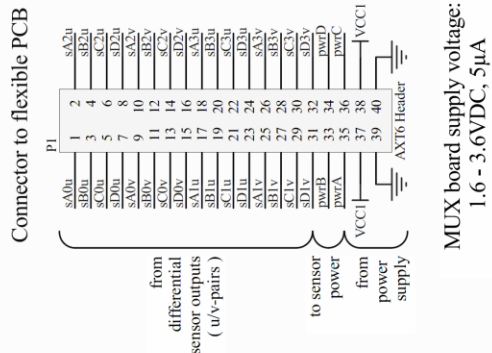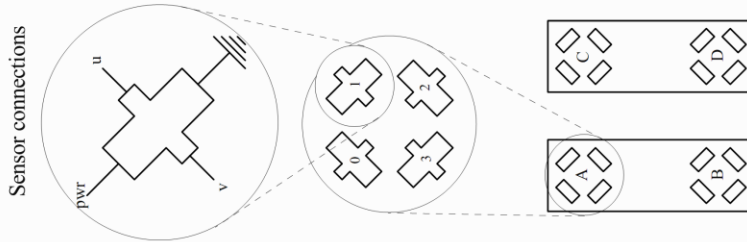
Appendix A-2: Multiplexer schematic

Appendix A-3: Base station schematic, microcontroller and USB interface (sheet 1)

Appendix A-4: Base station schematic, MICS (sheet 2)

Appendix A-5: Base station schematic, 2.45 GHz wake up (sheet 3)
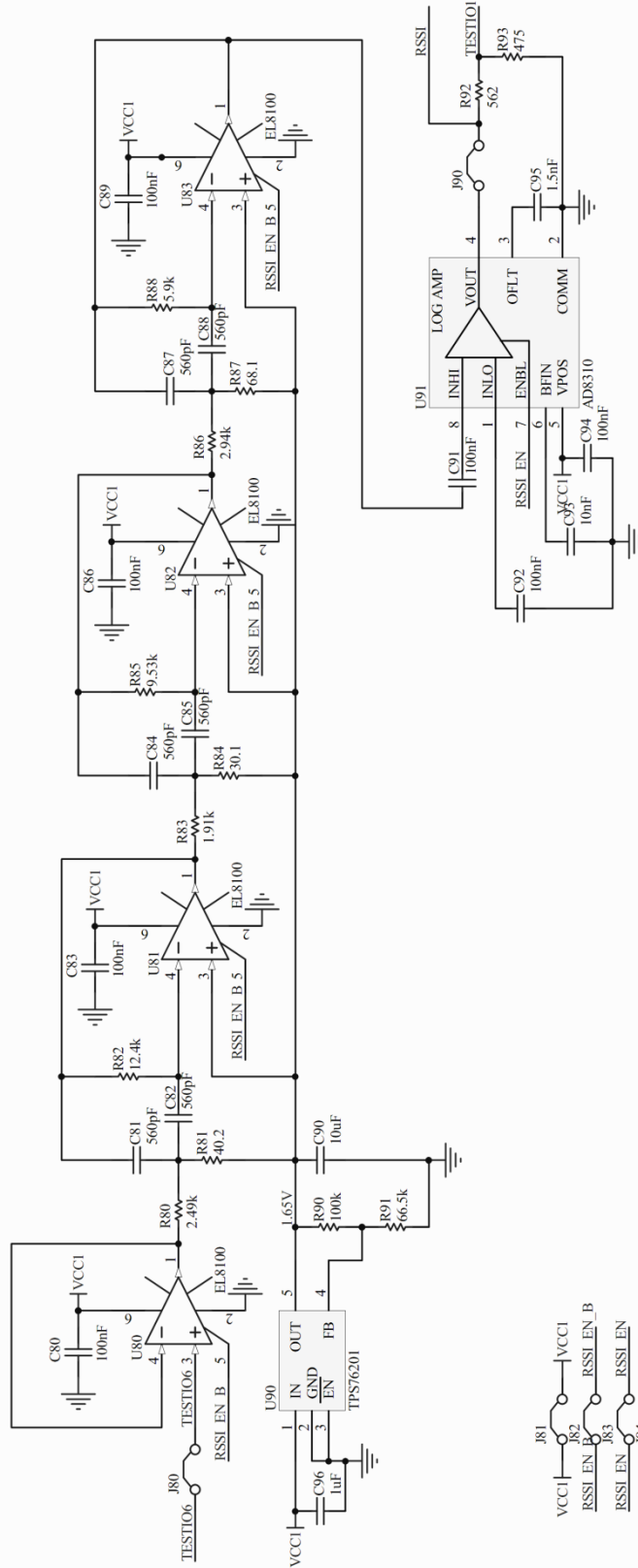
Appendix A-6: Base station schematic, RSSI filter (sheet 4)
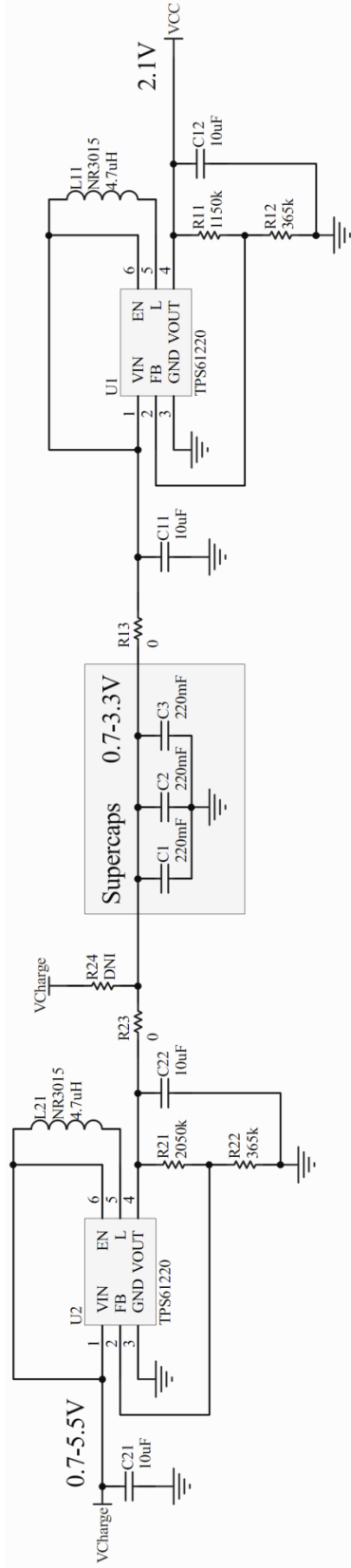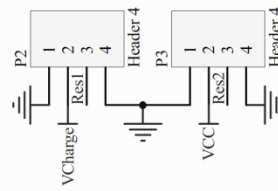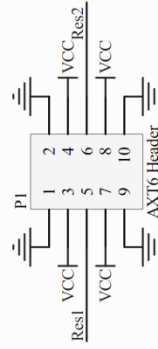
Appendix A-7: Capacitive power module schematic